

HARMONIC MOTION MICROWAVE DOPPLER IMAGING METHOD

A THESIS SUBMITTED TO  
THE GRADUATE SCHOOL OF NATURAL AND APPLIED SCIENCES  
OF  
MIDDLE EAST TECHNICAL UNIVERSITY

BY

CAN BARIŞ TOP

IN PARTIAL FULFILLMENT OF THE REQUIREMENTS FOR  
THE DEGREE OF DOCTOR OF PHILOSOPHY

IN

ELECTRICAL AND ELECTRONICS ENGINEERING

SEPTEMBER 2013



Approval of the Thesis:

**HARMONIC MOTION MICROWAVE DOPPLER IMAGING METHOD**

submitted by **CAN BARIŞ TOP** in partial fulfillment of the requirements for the degree of **Doctor of Philosophy in Electrical and Electronics Engineering Department, Middle East Technical University** by,

Prof. Dr. Canan ÖZGEN  
Dean, **Graduate School of Natural and Applied Sciences** \_\_\_\_\_

Prof. Dr. Gönül TURHAN SAYAN  
Head of Department, **Electrical and Electronics Engineering** \_\_\_\_\_

Prof. Dr. Nevzat Güneri GENÇER  
Supervisor, **Electrical and Electronics Engineering Dept., METU** \_\_\_\_\_

**Examining Committee Members:**

Prof. Dr. Mustafa KUZUOĞLU  
Electrical and Electronics Engineering Dept., METU \_\_\_\_\_

Prof. Dr. Nevzat Güneri GENÇER  
Electrical and Electronics Engineering Dept., METU \_\_\_\_\_

Prof. Dr. Ergin ATALAR  
Electrical and Electronics Engineering Dept., Bilkent University \_\_\_\_\_

Prof. Dr. Sencer KOÇ  
Electrical and Electronics Engineering Dept., METU \_\_\_\_\_

Prof. Dr. Şimşek DEMİR  
Electrical and Electronics Engineering Dept., METU \_\_\_\_\_

**Date:** 03.09.2013

**I hereby declare that all information in this document has been obtained and presented in accordance with academic rules and ethical conduct. I also declare that, as required by these rules and conduct, I have fully cited and referenced all material and results that are not original to this work.**

Name, Last name: Can Barış TOP

Signature :

## **ABSTRACT**

### **HARMONIC MOTION MICROWAVE DOPPLER IMAGING METHOD**

TOP, Can Barış

Ph. D., Department of Electrical and Electronics Engineering  
Supervisor: Prof. Dr. Nevzat Güneri GENÇER

September 2013, 126 pages

Conventional method for breast tumor detection, mammography, has a number of drawbacks such as X-ray exposure, patient discomfort and loss of reliability especially for dense breast tissue. Therefore, it is a hot research topic to develop new alternative non-invasive, reliable, safe and patient friendly breast imaging methods. In this thesis, we propose a novel hybrid mechanical and electromagnetic imaging method to identify cancerous regions particularly inside dense glandular breast tissue at the early stage by making use of the contrast between elastic and electrical properties of healthy and malignant tissues. A small vibrating region is created inside the tissue using the radiation force of focused ultrasound waves. A microwave transceiver is used to collect data from the vibrating region at the Doppler frequency, which depends on both elastic and electrical properties. The vibrating region is scanned inside the tissue to generate images. A semi-analytical formulation for the forward problem is developed using a two-layered simple breast model. A three dimensional Finite Difference Time Domain (FDTD) method is developed for analyzing the scattered signal from a vibrating region inside the tissue. Forward multi-physics problem is solved numerically with successive acoustic, mechanical and electromagnetic simulations. The performance of the method is investigated using both homogeneous and realistic numerical tissue models. Phantom materials that mimic the electrical and elastic properties of the fatty, fibro-glandular and malignant breast tissues are developed. The proof of concept is demonstrated experimentally on breast phantom materials using general measurement devices. A 5 mm diameter tumor phantom inside fibro-glandular tissue phantom was identified at 25 mm depth. Simulation results show that even smaller tumors can be detected inside breast issue if specialized receivers and transmitters are used. Even though the performance of the method is investigated for breast tumor detection in the scope of this thesis, it can be used for detecting tumors in the other organs that are microwave and ultrasound penetrable.

Keywords: Medical Imaging, Microwave Imaging, Breast Cancer Detection, Focused Ultrasound, Elasticity Imaging, Finite Difference Time Domain Method

## ÖZ

### HARMONİK HAREKET MİKRODALGA DOPPLER GÖRÜNTÜLEME YÖNTEMİ

TOP, Can Barış

Doktora, Elektrik ve Elektronik Mühendisliği Bölümü  
Tez Yöneticisi: Prof. Dr. Nevzat Güneri GENÇER

Eylül 2013, 126 sayfa

Meme kanseri tanısı için yaygın olarak kullanılan mamografi yönteminde iyonizan radyasyon kullanımı, yoğun meme dokusunda ayırt ediciğin azalması ve hastaya rahatsızlık vermesi gibi problemler bulunmaktadır. Bu nedenle bu yönteme alternatif invazif olmayan, güvenilir, zararsız ve hasta dostu yeni yöntemler geliştirilmesi üzerine araştırmalar devam etmektedir. Bu tezde, normal ve patojen dokuların elastik ve elektriksel özelliklerini kullanarak meme tümörlerinin erken evrede teşhis edilmesini amaçlayan yeni bir görüntüleme yöntemi önerilmektedir. Yöntemde odaklı ultrason dalgalarının ışıma kuvveti kullanılarak doku içinde titreşen küçük bir bölge yaratılmaktadır. Dokuya aynı zamanda mikrodalga işaret uygulanmaktadır. Geri yansıyan işaret tayfında titreşimden dolayı Doppler bileşeni oluşmaktadır. Bu bileşen titreşen bölgenin elastik ve elektriksel özelliklerine bağlıdır. Doku içinde odak bölgesi taranmakta ve her bir tarama noktasında geri yansıyan işaretin Doppler bileşeni algılanıp işlenerek görüntü oluşturulabilmektedir. Yöntemin basit meme modeli ile performansının değerlendirilmesi için yarı-analitik bir formülasyon geliştirilmiştir. Doku içinde titreşen bölgeden saçınan işaretin analiz edilmesi için üç boyutlu Zamanda Sonlu Farklar tabanlı bir yöntem geliştirilmiştir. Akustik, mekanik ve elektromanyetik benzetimler artarda yapılarak ileri problem sayısal olarak çözülmüştür. Yöntemin başarımı, homojen ve gerçekçi meme modelleri kullanılarak sayısal olarak incelenmiştir. Meme dokusunun elektriksel ve elastiklik özelliklerine benzeyen malzemeler (fantomlar) geliştirilmiştir. Önerilen görüntüleme yönteminin kullanılabilirliği geliştirilen doku benzeri malzemeler üzerinde genel test ekipmaları kullanılarak deneysel olarak incelenmiştir. 25 mm derinliğinde 5 mm çapında bir tümör fantomu glandüler meme fantomu içinde ayırt edilebilmiştir. Benzetim sonuçları uygun almaç devreleri kullanıldığında gerçek doku içinde daha küçük tümörlerin de tespit edilebileceğini göstermektedir. Bu çalışma kapsamında yöntemin performansı meme kanserinin tespiti için incelenmiş olsa da, mikrodalga ve ultrasonik işaretlerin nüfuz edebildiği diğer doku ve/veya organlarda da kullanım potansiyeli bulunmaktadır.

Anahtar Kelimeler: Tıbbi görüntüleme, Mikrodalga görüntüleme, Meme Kanseri Tespiti, Odaklı Ultrason, Elastiklik Görüntüleme, Zamanda Sonlu Farklar Yöntemi

To my beloved wife Özden

## ACKNOWLEDGMENTS

The author would like to express his sincere appreciation to his supervisor, Prof. Dr. Nevzat Güneri GENÇER for his support, valuable guidance, supervision and friendly encouragement.

The author is grateful to Prof. Dr. Ergin ATALAR, Prof. Dr. Sencer KOÇ, and Prof. Dr. Şimşek DEMİR for their support and advices.

The author is also grateful to: Prof. Dr. Nesrin HASIRCI and Dr. Aysel KIZILTAY for their help on the elasticity measurements of the phantom materials; Assoc. Prof. Dr. Barış BAYRAM for his help on ultrasound field measurements; METU EEE Microwaves and Antennas group members for providing necessary microwave measurement instruments.

The author would like to express his gratings to his project friend Azadeh KAMALI TAFRESHI for her help in the phantom development process and experimental studies. Her practical ideas helped very much in desperate situations. The author is also grateful to: Dr. Reyhan ZENGİN for her support, advices, and help in purchasing issues; Dr. Koray Özdal ÖZKAN and Mürsel KARADAŞ for their support, advices, and help in measurement hardware.

The author would like to acknowledge his gratitude to his friends and colleagues Mr. Mehmet Erim İNAL, Mr. Rahmi DÜNDAR, Erdiñ ERÇİL, Doğanay DOĞAN, Egemen YILDIRIM, Akın DALKILIÇ, Hakan BÖLÜKBAŞI, Dr. Nizam AYYILDIZ, Dr. Burak ALIŞAN, Atacan YAĞBASAN, Bilal UĞURLU, Hasan MERCAN and Dr. Feza CARLAK for their friendship, support and advices.

The author is also grateful to ASELSAN A.Ş. for all facilities provided for the completion of this thesis.

For translating the idea to experimental studies, author would like to express his gratitude to The Scientific and Technological Research Council of Turkey (TUBITAK) for supporting the experimental work financially with project code 112E031.

The author would like to express his deepest gratitude to his parents, Nedret and Cevdet, and his sister Başak for their invaluable love, support, encouragement and advices.



The author is also grateful to his mother-in-law Münevver ÖZCAN, father-in-law Mustafa ÖZCAN, sister-in-law Zeynep ÖZCAN, his aunts Sevin AKSOY and Nermin DEMİR, and his uncle Mehmet AKSOY for their support, love and encouragement.

Finally, the author feels grateful to his wife Özden for her patience and understanding. Her encouragement, support and endless love have always been the greatest assets of his life.

## TABLE OF CONTENTS

ACKNOWLEDGMENTS .....	viii
TABLE OF CONTENTS.....	x
LIST OF TABLES .....	xii
LIST OF FIGURES .....	xiii
LIST OF ABBREVIATIONS.....	xx
CHAPTERS	
1. INTRODUCTION .....	1
2. A SEMI-ANALYTICAL FORMULATION FOR THE HMMDI METHOD .....	7
2.1. Introduction.....	7
2.2. Generation of Harmonic Motion Inside The Tissue .....	7
2.3. Electromagnetic Problem: A Semi-Analytical Solution .....	9
2.4. Validation of the Semi-Analytical Solution.....	13
2.5. Received Signal Due To Electrically Small Tumor.....	16
2.6. The Effect of Vibration.....	18
2.7. Mechanical Problem .....	19
2.8. Results.....	23
2.8.1. Microwave Operation Frequency.....	24
2.8.2. Tumor in Fibro-glandular Tissue .....	25
2.8.3. Replacing the Tumor with a Spherical, Electrically Small, Low Adipose Content Tissue .....	26
2.8.4. Distance and Alignment of the Waveguide Probes.....	26
2.8.5. Effect of Tumor Depth in Received Signal.....	28
2.8.6. Receiver Sensitivity .....	29
2.8.7. Safety .....	30
2.9. Conclusions and Discussion.....	33
3. DEVELOPMENT OF NUMERICAL TOOLS FOR REALISTIC SIMULATIONS ...	35
3.1. Introduction.....	35
3.2. Mechanical FDTD Solver for Displacement Analysis.....	37
3.3. Electromagnetic FDTD Solver.....	42
3.3.1. Scattered Field from a Vibrating Tumor Inside the Tissue in 3-D FDTD .....	43
3.3.2. Validation of the FDTD code.....	49
4. NUMERICAL SIMULATIONS.....	53
4.1. Introduction.....	53
4.2. Simulations for the Tumor Inside Homogenous Tissue.....	53
4.2.1. Acoustic Simulations .....	53
4.2.2. Mechanical Simulations.....	54

4.2.3.	Electromagnetic Simulations .....	59
4.3.	Simulations with the Realistic Breast Tissue Model.....	63
4.3.1.	Mechanical Simulations .....	64
4.3.2.	Electromagnetic Simulations .....	67
4.4.	Late Time Response.....	76
4.5.	Conclusions and Discussion.....	79
5.	DEVELOPMENT OF BREAST PHANTOM MATERIALS .....	81
5.1.	Introduction.....	81
5.2.	Phantom Preparation Procedure.....	82
5.3.	Dielectric Properties of the Developed Phantoms .....	83
5.4.	Elastic Properties of the Developed Phantoms .....	87
5.6.	Breast Phantoms for Imaging Setup.....	89
5.7.	Conclusion and Discussion .....	91
6.	EXPERIMENTAL STUDY .....	93
6.1.	Experimental Setup .....	93
6.1.1.	Focused Ultrasound Transducer.....	94
6.1.2.	Antenna Design.....	95
6.1.3.	Phase Noise of the Transmitter .....	96
6.2.	Measurements for the Phantom-1 .....	97
6.2.1.	Microwave Frequency Analysis.....	97
6.2.2.	Linear Scan Results.....	102
6.3.	Measurements with Phantom-2.....	106
6.4.	Conclusions and Discussions .....	108
7.	CONCLUSIONS AND FUTURE WORK .....	110
	REFERENCES .....	113
	CURRICULUM VITAE .....	124

## LIST OF TABLES

Table 2-1: Parameters Used in the Sample Problem.....	15
Table 2-2: Comparison of S-Parameters from Semi-analytical and Numerical Results.....	15
Table 2-3: Parameters Used in Mechanical Simulation.....	21
Table 2-4: Displacement beam widths and maximum displacement values.....	22
Table 3-1: Parameters Used In Mechanical Simulations .....	41
Table 4-1: Parameters used for intensity calculations with HIFU Simulator .....	55
Table 4-2: Acoustic and mechanical parameters for different tissue types used in the mechanical simulations.....	57
Table 4-3: The displaced region widths (DRW) and the peak-to-peak displacement values at the focus for the homogenous numerical phantom calculated by averaging the first 3 excitation cycles.....	58
Table 4-4: Parameters Used In The Electromagnetic Simulations .....	60
Table 4-5: Acoustic and mechanical parameters for different tissue types used in the mechanical simulations.....	65
Table 4-6: The displaced region width (DRW) and the displacement values at the focus mechanical simulations for the realistic phantom.....	66
Table 5-1: Amounts of materials for preparing 1 liter phantom ( p-tol: p-toluic asit, .....	82
Table 5-2: Measured Storage ( $E'$ ) and loss ( $E''$ ) modulus of the phantom samples (DMA)	87
Table 5-3: Measured Young's modulus of the phantom samples (Static compression measurements) .....	89
Table 5-4: Measured ultrasonic properties of the phantoms .....	89
Table 6-1: Properties of the FUS transducer Sonic Concepts H-102.....	94

## LIST OF FIGURES

Figure 1-1: The anatomy of the female breast [43] (by Patrick J. Lynch, medical illustrator; C. Carl Jaffe, MD, cardiologist).....	3
Figure 1-2: Dielectric constant (a) and conductivity (b) for different kinds of normal breast tissues and malignant tissue [72]. .....	4
Figure 2-1: Illustration of the proposed Harmonic Motion Microwave Doppler Imaging System. Local harmonic motion is generated by the focused ultrasound probe. Microwave radar is employed for detecting the received signal amplitude at the Doppler frequency. ....	8
Figure 2-2: Problem geometry for the semi-analytical solution. Waveguide aperture is radiating into two-layered lossy half space. Geometry extends to infinity for $\pm x, \pm y$ and $+z$ directions. Waveguide broad-wall and narrow-wall dimensions are $a$ and $b$ , respectively. Wall thickness of the waveguide is zero. Thickness of the skin is $d$ . .....	10
Figure 2-3: Sample problem geometry (CST MWS). TX (Transmitting) and RX (Receiving) antennas are placed on two layered medium. Boundaries are terminated with Perfectly Matched Layer (PML). .....	14
Figure 2-4: Normalized E-field components at the mid-line of waveguides obtained with semi-analytical and numerical solvers. ....	15
Figure 2-5: Illustration of the original and the reciprocal problems. ....	17
Figure 2-6: Axially symmetric ultrasound intensity (normalized) map inside the tissue for mechanical simulations. A focused ultrasound transducer is placed at $-y$ end. 3.5 cm water layer is not shown. ....	20
Figure 2-7: Snapshots at the maximum displacement instant for normal breast tissue at 250 Hz vibration frequency at the first displacement peak (a), and the sixth displacement peak (b) at the focus. ....	22
Figure 2-8: Normalized lateral (a) and axial (b) displacement cuts for the first displacement peak at the focus. Normalized lateral displacement for the late time displacement peak at the focus (c). ....	23
Figure 2-9: Geometry for the microwave operation frequency analysis. Spherical tumor of 1.5 mm radius is introduced at 3 cm depth measured from the top of the skin layer.....	25
Figure 2-10: Scattered signal level (at the Doppler frequency) as a function of frequency for different tissue types. Solid line (—): high adipose content tissue, dashed line(- -): medium adipose content tissue. Dash dotted line (- · - ·): low adipose content tissue. (Tumor radius:	

1.5 mm, tumor depth: 30 mm, probe separation: 20 mm, probe alignment: E-plane, max. displacement of tumor: 2.5 $\mu\text{m}$ ).....	25
Figure 2-11: Geometry for the case, in which the tumor is inside low adipose content tissue. Spherical tumor of 1.5 mm radius is introduced at 3 cm depth measured from the top of the skin layer, inside the low adipose content tissue. ....	26
Figure 2-12: Geometry for E-plane and H-plane Alignment of Waveguide Probes.....	27
Figure 2-13: Scattered signal (at the Doppler frequency) as a function of antenna distance for E-plane and H-plane aligned antennas. Solid line (—): H-plane alignment, dashed line (- -): E-plane alignment (Tumor radius: 1.5 mm, tumor depth: 30 mm, max. displacement of tumor: 2.5 $\mu\text{m}$ , TX Power: 1 W).....	27
Figure 2-14: Direct probe coupling to the scattered signal (at the Doppler frequency) ratio as a function of probe distance for E-plane and H-plane aligned probes. Solid line (—): H-plane alignment, dashed line (- -): E-plane alignment (Tumor radius: 1.5 mm, tumor depth: 30 mm, max. displacement of tumor: 2.5 $\mu\text{m}$ ).....	28
Figure 2-15: Scattered signal (at the Doppler frequency) level as a function of tumor depth for 5 GHz frequency with E and H plane probe alignments. Solid line (—): H-plane alignment, dashed line (- -): E-plane alignment (Tumor radius: 1.5 mm, probe separation: 20 mm, max. displacement of tumor: 10 $\mu\text{m}$ ).....	29
Figure 2-16: SAR value as a function of depth at the midline of the transmitter probe at 5 GHz for 1Watt probe output power. Solid line (—): high adipose content tissue, dashed line (- -): medium adipose content tissue, dash dotted line (- . - .): low adipose content tissue. ....	31
Figure 3-1: Forward Problem Simulation Methodology for HMMDI Method .....	36
Figure 3-2: Positions of the material constants, velocity and strain fields in the unit cell. The components at the points P1 to P7 are; P1: $\rho, \lambda, \mu, \tau_{xx}, \tau_{yy}, \tau_{zz}$ , P2: $v_x$ , P3: $v_y$ , P4: $v_z$ , P5: $\tau_{yz}$ , P6: $\tau_{xz}$ and P7: $\tau_{xy}$ .....	40
Figure 3-3: Mechanical volume load applied to the tissue. ....	41
Figure 3-4: The displacement values at the focal point obtained from FDTD and COMSOL simulation results. ....	42
Figure 3-5: Original (on the left) and the volume equivalent (on the right) FDTD simulation geometries. Breast tissue is modeled with two layers: skin and normal (high adipose content) tissue. Antennas are placed on top of the skin layer. A cubic tumor is present in the original problem. In the reciprocal problem it is replaced by volume equivalent current source. ....	44
Figure 3-6: Procedure of the method for calculating the Doppler component of the scattered field .....	44

Figure 3-7: FDTD grid showing field components  $E_z$ ,  $E_y$  and  $H_x$  for the displaced scatterer case on the y-z plane cut of the 3D geometry.  $E_z$ ,  $H_y$  and  $H_z$  field components are not shown for simplicity..... 46

Figure 3-8:  $S_{11}$  phase in radians for the waveguide discontinuity problem as a function of normalized sheet thickness. .... 50

Figure 3-9: Comparison of the results obtained by numerical (FDTD) and semi-analytical solution..... 51

Figure 4-1: Simulation geometry for the simulations of tumor inclusion inside a homogenous tissue. Focus of the ultrasound transducer is at 25 mm depth inside the tissue. Water filled open-ended waveguides are placed on the 2 mm thick skin tissue. A tumor inclusion of 3 mm edge length size is introduced at 25 mm depth inside the high adipose content tissue. The focus is scanned in  $x$  and  $z$  directions. .... 54

Figure 4-2: Acoustic simulation results for: (a) Pressure waveform, (b) Time average intensity, (c) Peak positive and negative pressure, (d) Heat, calculated in the axial direction. .... 55

Figure 4-3: Simulation geometry for the mechanical simulations. A focused ultrasound transducer is assumed to be present upon homogenous breast tissue. Transducer is focused at 25 mm depth. .... 56

Figure 4-4: Displacement distribution inside the tissue at the first maximum displacement instant for 500 Hz vibration frequency. Left: Normal tissue, right: cubic tumor of 3mm edge length is introduced..... 58

Figure 4-5: The displacement at the focus for homogenous model simulations for (a) 125 Hz, (b) 250 Hz, and (c) 500 Hz vibration frequencies. The tumor is not present in the solid line plots, whereas a cubic tumor with 3mm edge length is introduced in the dashed line plots.. 59

Figure 4-6: Doppler component to directly coupled signal ratio for different probe arrangements as a function of tumor depth..... 60

Figure 4-7: Signal level at the Doppler frequency for 1 W microwave output power as a function of scan position in  $x$  direction calculated using the 1<sup>st</sup> cycle of the vibration. Tumor with 3 mm edge size is present at 25 mm depth. The boundary of the tumor is shown as dashed-dotted line. .... 62

Figure 4-8: Signal level at the Doppler frequency for 1 W microwave output power as a function of scan position in  $z$  direction calculated using the 1<sup>st</sup> cycle of the vibration. Tumor with 3 mm edge size is present at 25 mm depth. The boundary of the tumor is shown as dashed line. .... 62

Figure 4-9: Four classes of ACR categorized breast images in UWCEM phantom repository [89]: (a) Class I, (b) Class II, (c) Class III, (d) Class IV..... 64

Figure 4-10: The breast phantom used in the simulations (Left: Side view, Right: Top view).The yellow region is fibro-glandular tissue, red region is fat tissue. The extent of the simulation geometry is shown in black dashed line for 125 Hz, light blue dashed line for 250 Hz, and green dashed line for 500 Hz. The place of the virtual ultrasound probe is shown in the left figure. The tumor is depicted in white color..... 65

Figure 4-11: The displacement at the focus for realistic model simulations. The tumor is not present in the solid line plots, whereas a cubic tumor with 3mm edge length is introduced in the dashed line plots. (a) 125 Hz vibration frequency, (b) 250 Hz vibration frequency, (c) 500 Hz vibration frequency. The moments when the displacement distribution is exported (1<sup>st</sup> maximum and 1<sup>st</sup> minimum) to a text file are shown with circles. .... 66

Figure 4-12: Geometry for the electromagnetic simulations for realistic numerical tissue model. .... 67

Figure 4-13: The realistic numerical breast model. The dielectric distribution inside the tissue is shown for: (a) Y=81.5 mm cut, (b) Z=58 mm cut, (c) X=75 mm cut. The intersection of the cut planes is the central point of tumor, which is introduced as a cubic inclusion with 3 mm edge length. The boundaries for the reduced model are shown with a dashed rectangle. The rectangle is moved in the  $x$  – direction for lateral scan simulations..... 68

Figure 4-14: The reduced numerical model used in the electromagnetic simulations. The dielectric distribution is shown for: (a) Y=30 mm cut, (b) Z=30 mm cut, (c) X=30 mm cut. The intersection of the cut planes is the central point of tumor which is introduced as a cubic inclusion with 3 mm edge length. Tumor is shown as a white box. .... 69

Figure 4-15: Displacement map cuts (Y=30mm) at the 1<sup>st</sup> maximum peak at the focus imported to the electromagnetic simulations. The displacement maps are shown in the presence and in the absence of the tumor inclusion for 125 Hz, 250 Hz, and 500 Hz vibration frequencies. The vibrating part for the scattering field calculation is depicted by a rectangle. .... 70

Figure 4-16: Geometries for the original (left) and the volume equivalent (right) problems for the realistic electromagnetic simulations. .... 71

Figure 4-17: Main frequency component of the received signal for the realistic simulation as a function of scan distance..... 72

Figure 4-18: Doppler component of the received signal as a function of lateral scan distance in the presence and in the absence of the tumor for (a) 125 Hz, (b) 250 Hz, and (c) 500 Hz vibration frequency. The place of tumor is shown as a pink region. .... 73

Figure 4-19: Differential Doppler component of the received signal as a function of scan distance in the presence and in the absence of the tumor for (a) 125 Hz – 250 Hz, (b) 125 Hz – 500 Hz , (c) 250 Hz – 500 Hz frequencies. The place of tumor is shown as a pink region. 74



Figure 4-20: Doppler component of the received signal as a function of axial scan distance in the presence and in the absence of the tumor for (a) 125 Hz, (b) 250 Hz, (c) 500 Hz vibration frequency. The place of tumor is shown as a pink region.....	75
Figure 4-21: Axial displacement plots for 500 Hz frequency at maximum and minimum displacement instants of the first cycle for (a) $x = 0$ mm, (b) $x = 1$ mm scan position.....	76
Figure 4-22: (a) Displacement of the focal point and the sampling instants in the presence and in the absence of the tumor at the focal point for 125 Hz, 250 Hz and 500 Hz vibration frequencies at 0 mm scan point. (b) Phase of the received signal at the sampled time instants in the presence and in the absence of the tumor at the focal point for 125 Hz, 250 Hz and 500 Hz vibration frequencies at 0 mm scan point.....	77
Figure 4-23: Simulation results for the received signal component (4 cycles of excitation) at the Doppler Frequency. Vibration is applied at 125 Hz, 250 Hz, and 500 Hz. The place of tumor is shown as a pink region.....	78
Figure 5-1: Probe model for virtual line method .....	83
Figure 5-2: Dielectric measurement of the breast fat phantom using network analyzer.....	85
Figure 5-3: Time-domain S11 parameter. Left : without “Gating”, Right: with “Gating”...	86
Figure 5-4: Measured relative permittivity of the developed phantoms. Top: Real part ( $\epsilon'$ ), Bottom: Imaginary part ( $\epsilon''$ ).....	86
Figure 5-5: Perkin Elmer Pyris Diamond Dynamic Measurement Analyzer (DMA) in METU Central Laboratory. ....	87
Figure 5-6: Lloyd LRX 5K materials testing machine in METU BIOMATEN laboratory testing fat phantom sample. The stress-strain relationships of the different phantom types are measured using a 100 N load cell. The samples were 15 mm in diameter and 10 mm in height. ....	89
Figure 5-7: Homogeneous breast phantom including 3 different size tumor phantoms at 30 mm depth. Left: Tumor phantoms used in the breast phantom, Middle: Tumor phantoms placed on the fat phantom at the first stage. Right: Final condition of the breast phantom after the second stage. ....	90
Figure 5-8: Homogeneous breast phantom including tumor phantom inside a fibro-glandular phantom. Left: Phantom geometry, Middle: Fibro-glandular phantom including tumor phantom placed on the fat phantom at the first stage. Right: Final condition of the breast phantom after the second stage. ....	91
Figure 6-1: Simplified schematic for experimental setup.....	93

Figure 6-2: The measured beam patterns of the FUS transducer for 1V peak to peak excitation.....	94
Figure 6-3: Antenna HFSS model. The design parameters are shown on the figure.....	95
Figure 6-4: Measured and simulated $S_{11}$ parameter of the antenna.....	96
Figure 6-5: Directly measured phase noise characteristic of the Signal Generator for 500 Hz frequency span.....	96
Figure 6-6: Phantom-1 before the second fat layer is poured.....	97
Figure 6-7: Setup configuration for the Phantom-1 measurements.....	98
Figure 6-8: Pressure and intensity at the focus of the ultrasound probe for microwave frequency analysis. Amplitude modulated pressure is applied as a burst of 3 cycles.....	98
Figure 6-9: Received signal and noise levels as a function of frequency when the focus is on the fibro-glandular phantom. 15 Hz vibration with 3 cycles is applied with 1 second PRI. Peak pressure is 6.7 MPa.....	99
Figure 6-10: (a) SNR, and (b) Doppler component to main frequency component. 15 Hz vibration with 3 cycles is applied with 1 second PRI. Peak pressure is 6.7 MPa.....	100
Figure 6-11: Ansys HFSS simulation geometry for coupling analyses. The antennas are placed at the bottom of the phantom. There is a 1 mm space between the aperture of the antennas and the glass. A third test antenna is placed on top of the phantom in order to observe the change in power transmitted to the phantom.....	100
Figure 6-12: Simulated and measured antenna coupling values.....	101
Figure 6-13: Simulated $S_{11}$ parameter of the antennas.....	101
Figure 6-14: Coupled signal from the transmitting antenna to the test antenna.....	102
Figure 6-15: FUS probe scanning on the breast phantom.....	103
Figure 6-16: Scan line 1 (black) and 2 (orange) for the heterogeneous tissue phantom.....	103
Figure 6-17: Simulation geometry for the linear scan measurements of Phantom-1.....	105
Figure 6-18: Measured and simulated signal level at the Doppler frequency for the linear scan across the fibro-glandular phantom, which contains tumor in the middle. The places of the tumor (red) and the fibro-glandular (yellow) phantoms are depicted in the figure.....	105

Figure 6-19: Scan line for the single 40 mm linear scan case for Phantom 1..... 106

Figure 6-20: Measured signal level at the Doppler frequency for the 40 mm linear scan across the fibro-glandular phantom, which contains tumor in the middle. The places of the tumor (red) and the fibro-glandular (yellow) phantoms are depicted in the figure..... 106

Figure 6-21: Phantom-2 before the second fat layer is poured. .... 107

Figure 6-22: Scan line 1 (black), 2 (orange), and 3 (gray) for Phantom-2..... 107

Figure 6-23: Measured signal level at the Doppler frequency for the linear scan across the heterogeneous breast phantom, which contains 3 different tumors. The places of tumors are depicted in red color..... 108

## LIST OF ABBREVIATIONS

ACR	American College of Radiology
AET	Acousto-Electrical Tomography
AM	Amplitude Modulation
ARFI	Acoustic Radiation Force Imaging
CEII	Contactless Electrical Impedance Imaging
CPML	Convolutional Perfectly Matched Layer
CW	Continuous Wave
DMA	Dynamic Measurement Analyzer
DTFT	Discrete Time Fourier Transform
DRW	Displaced Region Width
EII	Electrical Impedance Imaging
FDA	Food and Drug Administration
FDTD	Finite Difference Time Domain
FEM	Finite Element Method
FITD	Finite Integration Time Domain
FUS	Focused Ultrasound
FWHM	Full Width Half Maximum
HEI	Hall Effect Imaging
HIFU	High Intensity Focused Ultrasound
HMI	Harmonic Motion Imaging
HMMDI	Harmonic Motion Microwave Doppler Imaging
IF	Intermediate Frequency
$I_{SPPA}$	Spatial Peak Pulse Average Intensity
KZK	Khokhlov-Zabolotskaya-Kuznetsov
MAET	Magneto-Acousto-Electric Tomography
MAT-MI	Magneto Acoustic Tomography with Magnetic Induction
MI	Mechanical Index
MoM	Method of Moments
MRI	Magnetic Resonance Imaging
NCRP	National Council on Radiation Protection and Measurements
PML	Perfectly Matched Layer
RF	Radio Frequency
RX	Receiving

SAR	Specific Absorption Rate
SNR	Signal to Noise Ratio
SWEI	Shear Wave Elasticity Imaging
TE	Transverse Electrical
TI	Thermal Index
TX	Transmitting
US	Ultrasound

## CHAPTER 1

### INTRODUCTION

Breast cancer is the most common type of cancer among women. Officially 1.5 million women were diagnosed to have breast cancer in year 2010 [1]. Mammography is the clinically accepted breast imaging method for breast tumor detection, although it has drawbacks such as reliability, patient discomfort, and X-ray exposure. Mammography has high false positives rates as %70-80 that leads to unnecessary biopsies [2]-[4]. Detecting a tumor in dense breast tissue is challenging since the tumors can be hidden inside fibro-glandular tissue. In addition, ionizing radiation is used, which increases the risk of cancer formation. Other methods such as Magnetic Resonance Imaging (MRI) and Ultrasound are not very common for use as they both have some limitations [5]. Therefore, development of complementary or alternative imaging techniques is required in order to increase the accuracy in diagnosis. Electromagnetic imaging methods are evolved as a potential alternative to mammography method. The primary reason of that is breast tissue is penetrable in RF/microwave frequency spectrum and the dielectric contrast between breast fat and malignant breast tissue is high.

Imaging of biological tissues using electromagnetic radiation has been a research subject since the electrical properties of various tissues are discovered to be different. Electromagnetic imaging methods can be categorized into two according to frequency of operation: Low frequency Contactless Electrical Impedance Imaging (CEII) methods and high frequency RF/microwave methods. In low frequency CEII methods, time-varying magnetic fields are applied to the tissue, generally using coils. Currents are induced inside the tissue in response to the applied magnetic field. The amplitude of the induced currents depends on the conductivity of the tissue. Tissue conductivity distribution is reconstructed by sensing the secondary magnetic fields that are generated by the induced currents inside the tissue [6]-[10]. A quasi-static approach is used to analyze the problem since the wavelength of operation is very large compared to imaged subject and displacement currents can be neglected. Although penetration of electromagnetic waves inside the tissue at low frequencies is good, the image resolution is low due to large wavelengths. To enhance the resolution of electrical impedance imaging methods, hybrid acoustic-electromagnetic methods are proposed, which combine high resolution property of acoustic signals and tissue discrimination based on electrical conductivity. Hall Effect Imaging (HEI) [11]-[14], Acousto-electrical tomography (AET) [15], Magneto-acousto-electrical tomography (MAET) [16]-[18], Magneto acoustic tomography with Magnetic Induction (MAT-MI)[19]-[20] are the names of different imaging methods that make use of acoustics and electromagnetics together. In HEI and MAET, an ultrasound wave packet is sent to tissue, which is under the influence of a static magnetic field. Local acoustic vibration causes ions to move in the tissue with a velocity. This in turn, induces a Lorentz Force, thus a current that is proportional to conductivity of the tissue, velocity of the ions, and magnitude of the static magnetic field. A portion of this current is collected by electrodes or coils. MAT-MI is

similar to reverse HEI. The tissue to be imaged is put in a static magnetic field, and it is surrounded by acoustic transducers. A pulsed magnetic field is generated inside the tissue, and the acoustic signal generated in the tissue by Lorentz Force is sensed by acoustic transducers. In AET, change in resistivity, due to acoustical pressure which is proportional to tissue resistance, is being sensed.

In all of these methods, resolution is higher than the conventional EII systems, and limited by lateral and axial beamwidth of the ultrasound wave. Although high resolution is achieved, it was shown that collected signals are non-zero only at the boundaries of regions having different conductivity (because of the integration of bipolar ultrasound wave package). If there is a gradual change inside the tissue, this is invisible to the system.

The resolution of the imaging system can be increased using higher frequencies. However as the frequency gets higher, the skin depth decreases. Nevertheless, breast tissue is penetrable in the microwave frequency regime. Imaging of biological tissues especially for cancer detection in RF/Microwave frequency spectrum is a hot research topic since malign tumors have higher conductivity and permittivity values than normal tissues in this frequency range [21]. In microwave imaging systems, high frequency electromagnetic signals are transmitted to tissue using antennas and the backscattered signals are received by receiving antennas [23]-[25]. The images are reconstructed revealing dielectric distributions, rather than conductivity distributions as in low frequency impedance imaging, inside the tissue. In order to enhance resolution to detect small malignancies, ultra wideband systems are proposed. Hagness *et al.* introduced a pulsed confocal microwave imaging system operating at 6 GHz center frequency with 4 GHz bandwidth [26]-[27]. Fear *et al* also introduced a similar system with a bandwidth of 20 GHz with 10 GHz center frequency [28].

At this point it is worth to mention about the anatomy of breast tissue, which is shown in Figure 1-1. There are three main types of breast tissue: Fat, glandular (lobules, ducts) and connective tissues. The amount of glandular tissue changes from person to person. In the mammography image, glandular tissues are as opaque as tumors since they have low adipose content. Therefore, it is difficult to diagnose the presence of tumor in glandular tissue using mammography. The adipose (fat) content of tissues also affects their electromagnetic properties. A large scale study on the dielectric constants of normal and malign tissues reports that the dielectric contrast between the healthy glandular tissues and the malign tissues is (Figure 1-2) low [34], [35]. Therefore, tumors inside glandular tissues are not detectable using electromagnetic imaging methods, also.

The usage of contrast agents such as microbubbles or carbon nanotubes has a potential in enhancing the contrast between malignant and normal tissues [36]-[42]. These agents accumulate in malignant tumors and change their dielectric properties. Consequently, imaging is performed before and after contrast agent injection. Presence of a tumor is detected by observing the change in the dielectric properties. These studies are in the initial phase and further studies are needed before their use in the clinic.

1. Chest Wall
2. Pectoralis muscles
3. Lobules
4. Nipple
5. Areola
6. Milk Duct
7. Fatty Tissue
8. Skin

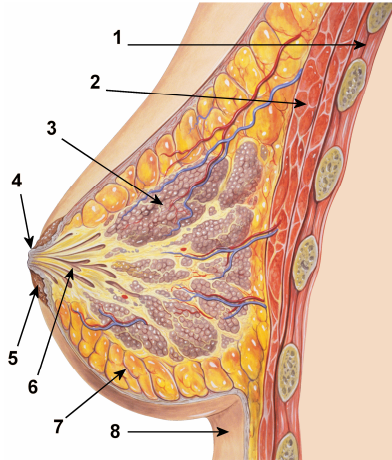
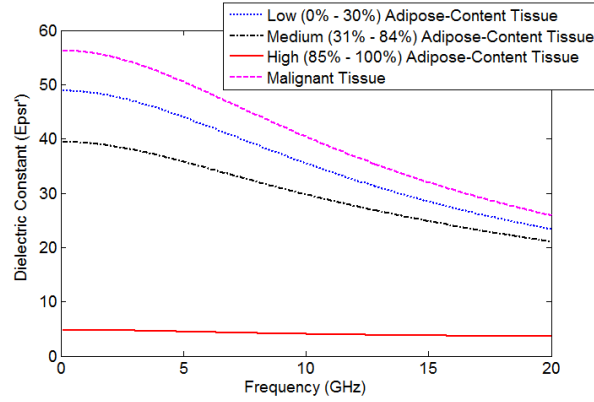


Figure 1-1: The anatomy of the female breast [43] (by Patrick J. Lynch, medical illustrator; C. Carl Jaffe, MD, cardiologist).

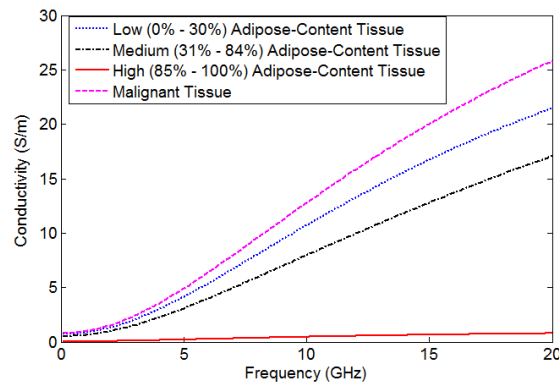
Another alternative to mammography is the remote palpation methods. Manual palpation is used for breast examination to feel hard lumps, since tumors are stiffer than normal tissues. The Young's constant (Elastic constant) of the malign tissues are reported to be higher than the normal breast tissues by a factor of 3 to 13[44]. Remote palpation methods such as Acoustic Radiation Force Imaging (ARFI), Vibro-acoustography, Shear Wave Elasticity Imaging (SWEI) and Harmonic Motion Imaging (HMI), make use of the radiation force of ultrasound for imaging the elastic properties of the tissue with high resolution. In HMI, a focused acoustic radiation force of ultrasound is used to make a locally oscillatory movement inside the tissue [45], [46]. The displacement amplitude at the focal region is measured with an imaging ultrasound transducer using cross-correlation techniques. Amplitude of the motion, i.e. the maximum displacement, gives information about the elasticity of the focal region. For the same amount of radiation force and similar thermal conditions, since the tumor is stiffer than the normal tissue, the displacement of the tumor region is smaller than the healthy tissues. The translation of these methods to clinical usage is still in progress.

The idea of using elastic contrast in microwave imaging is also proposed ([47] - [49]). In [48] and [49], the tissue is excited by low frequency (up to a few kHz) acoustic signals and the scattered microwave signal due to boundary perturbation of the tumor is calculated with 2-D FDTD simulations. It is concluded that with the usage of elastic properties more information about the malignancy of the tissue can be gained compared to conventional microwave imaging.





(a)



(b)

Figure 1-2: Dielectric constant (a) and conductivity (b) for different kinds of normal breast tissues and malignant tissue [72].

In this thesis, our aim is to develop a method for breast tumor detection and screening that is non-invasive, safe, reliable and patient friendly. We propose a novel imaging method to detect malignant breast tumors, particularly in glandular tissues, using their electrical and elasticity properties. We name the new method as Harmonic Motion Microwave Doppler Imaging (HMMDI).

In the proposed method, local vibration is induced inside the tissue using focused ultrasound, as in the case in HMI method. At the same time, microwave signals are transmitted to the tissue. Backscattered and received microwave signal is a phase and amplitude modulated signal due to the effect of vibration. The first spectral component of this signal, which differs from the transmitted signal frequency by an amount of vibration frequency, is sensed. The amplitude and phase of the received signal depends on the volume, maximum displacement, and dielectric properties of the vibrating region. If the vibrating region contains a volume that has a different permittivity and/or elasticity than the background, the scattered signal level will be changed. 3-D images can be obtained by scanning the tissue volume. The

proposed method has a potential to be used for tumor detection in other organs such as prostate and liver, as well.

This method has some advantages over electromagnetic imaging and elastography methods present in the literature. Firstly, better penetration depth is achievable using microwaves rather than ultrasound. Secondly, the response is related to both mechanical and electrical parameters of the tissue. Therefore, more information is obtained compared to only microwave or elasticity imaging, to localize malignant regions if present. Thirdly, the method can be combined with microwave imaging and dielectric and elastic properties can be reconstructed at the same time yielding better sensitivity and specificity.

The novelty of this method compared to earlier hybrid microwave-elasticity imaging methods given in [47]-[49] is that the tissue is excited with focused high frequency ultrasound signals, which inherently increases the resolution and makes it possible for the detection of smaller tumors. In addition, it is the first time in the literature that the feasibility of a hybrid microwave-elasticity imaging method is investigated extensively. The method is analyzed semi-analytically, numerically and experimentally for breast tumor detection in the scope of this thesis.

This thesis is organized as follows:

In Chapter 2, a semi-analytical solution for the forward problem solution of HMMDI method is given. The received signal level from a vibrating spherical scatterer inside simple breast tissue model is analyzed. A commercial Finite Element Method (FEM) solver is used for mechanical simulations for which the effect of vibration frequency on the tissue displacement amplitude is analyzed. The effect of microwave frequency of operation, antenna placement, depth of tumor scatterer on the received signal is investigated together with safety considerations.

In Chapter 3, a numerical solution procedure for the forward problem in HMMDI method is given. The procedure involves solving the acoustical, mechanical and electromagnetic problems successively. FDTD simulators for both mechanical and electromagnetic problems are developed and verified.

In Chapter 4, performance of the method is investigated with a homogenous numerical breast model and a realistic numerical breast phantom using the developed numerical solution procedure in Chapter 3. The effects of vibration frequency and the shear waves on the received signal amplitude are given.

In Chapter 5, the development of realistic breast phantoms for experimental analysis is given. The elasticity, electromagnetic and ultrasonic properties for the developed phantom materials are measured. Two breast tissue phantoms are developed for the experiments: One includes three different sized tumor phantoms in homogeneous fat tissue; the other includes fibro-glandular tissue phantom that has a small tumor inside.

In Chapter 6, the proposed method is investigated experimentally on the developed breast phantoms. The phantom materials are vibrated locally using a FUS probe. Microwave signals are transmitted to the phantom during ultrasound excitation. The amplitude of the received signal at the Doppler (vibration) frequency signal is sensed using a Spectrum Analyzer. Experimental results are compared to simulation results. It is shown that the proposed method is promising for detecting tumors inside fibro-glandular tissue.

## CHAPTER 2

### A SEMI-ANALYTICAL FORMULATION FOR THE HMMDI METHOD

#### 2.1. Introduction

In this chapter, the received signal amplitude due to a vibrating small spherical tumor in homogeneous breast tissue is investigated. The scattered signal from the tumor is calculated semi-analytically in the MATLAB (The MathWorks, Inc., MA, USA) environment, using a two-layer planar breast model. The perturbation of dielectric constant due to the change in density of the vibrating region [56] is not considered. Water filled open-ended waveguide probes are assumed to be used for transmitting and receiving microwave signals. Waveguide probes are assumed to be placed on the tissue in order to get maximum coupling. Reciprocity theorem is used in calculating the received signal from the tumor. The effect of microwave operation frequency, tumor depth and probe alignment on the received signal amplitude are given for a fixed vibration amplitude. Since the expected resolution of the system is high because of the usage of ultrasound waves, a narrow-band microwave system is employed rather than an ultra wideband (short pulse) system. Noise bandwidth is made smaller to increase the Signal to Noise Ratio (SNR) of the system by this choice. Using a commercial Finite Element Method (FEM) solver COMSOL (COMSOL, Inc., MA, USA), displacement amplitude of the vibrating region is calculated for a sample ultrasound configuration that does not exceed ultrasound safety limits. The displacement amplitude of breast fat, fibroglandular and tumor for vibration frequencies of 125 Hz, 250 Hz and 500 Hz are calculated assuming a linear elastic tissue model. The safety of the method is also analyzed in terms of ultrasound and microwave exposure.

The proposed method utilizes ultrasound transducer(s) to generate local harmonic motion inside the tissue. A microwave transceiver system, which has separate dielectric-filled open-ended waveguide antennas for transmitting and receiving microwave signals, is utilized (Figure 2-1).

#### 2.2. Generation of Harmonic Motion Inside The Tissue

The tissue is vibrated by a focused ultrasound transducer with amplitude modulated signal. Alternatively two focused transducers driven with a frequency difference of  $\Delta\omega$  can be used. When a tissue is exposed to ultrasound radiation, a unidirectional force acts on the tissue, which is caused by the momentum transfer from the acoustic signal to the medium [55]. The direction of this force is in the direction of propagation. In the biological tissues, acoustic attenuation is mainly caused by absorption, and the force applied to tissue can be written as [57]:

$$F = \frac{2\alpha I}{C_s} \quad (2-1)$$

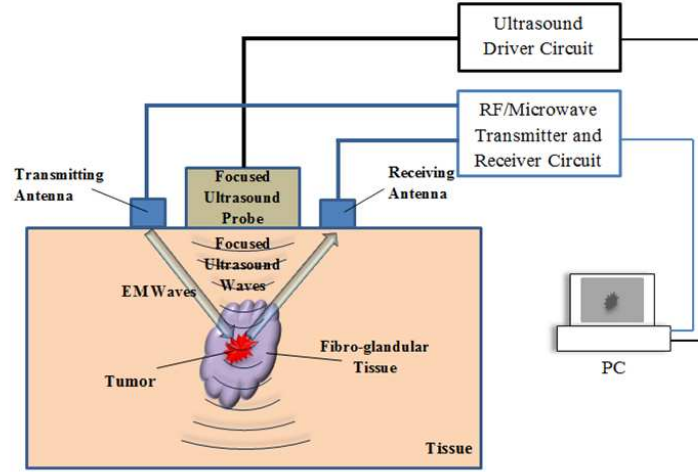


Figure 2-1: Illustration of the proposed Harmonic Motion Microwave Doppler Imaging System. Local harmonic motion is generated by the focused ultrasound probe. Microwave radar is employed for detecting the received signal amplitude at the Doppler frequency.

where  $\alpha$  (1/m) is the absorption constant of the tissue,  $I$  ( $\text{W}/\text{cm}^2$ ) is the short-term time average intensity of the acoustic beam,  $C_s$  (m/s) is the speed of ultrasound in tissue.  $F$  is the force per unit volume ( $\text{kg}/\text{s}^2\text{cm}^2$ ).

The pressure of the amplitude modulated acoustic beam at the focus can be written as [46] :

$$P(t) = P_0 \cos(\Delta\omega/2t) \cos(\omega_u t + \phi) \quad (2-2)$$

where  $P_0$  is the amplitude of the pressure wave,  $\Delta\omega/2$  is the modulation frequency, and  $\omega_u$  is the carrier frequency. The short-term time average intensity of the beam can be expressed as [55] :

$$I = \frac{P_0^2}{4\rho C_s} (1 + \cos(\Delta\omega t)) \quad (2-3)$$

where  $\rho$  is the density of tissue.

Elasticity parameters, Young's Modulus ( $E$ ) and Poisson's ratio ( $\nu$ ) of the tissue is related to the displacement of the tissue and radiation force by [54]:

$$E = \frac{2(1 - \nu)^2 F r_b}{X_0 A} \quad (2-4)$$

where  $F$  is the acoustic radiation force given in(2-1),  $r_b$  is the radius of the beam at the focus,  $A$  is the cross sectional area of the beam at the focus,  $X_0$  is the maximum displacement of the tissue. The acoustic beam radius  $r_b$  can be defined as half of the full width at half maximum (FWHM) intensity beamwidth at the focus in the axial direction. Assuming axial symmetry for the intensity, the cross-sectional area of the beam ( $A$ ) is the area inside the FWHM circle, i.e.,  $A = \pi r_b^2$ .

For a sinusoidal excitation  $F(t) = F_0 \cos(\Delta\omega t)$ , the local tissue in motion can be represented by a circular piston and the displacement is given by [55]:

$$X(t) = \frac{F_0 \cos(\Delta\omega t)}{\Delta\omega Z} = X_0 \cos(\Delta\omega t + \varphi) \quad (2-5)$$

where  $Z$  is the mechanical impedance of the tissue.

The peak value of local displacement  $X_0$  depends on the mechanical properties (elasticity/stiffness) of the local tissue as well as the intensity of the ultrasound. It is not straightforward to calculate  $X_0$  analytically since complex mechanics is involved in biological tissues. Approximate analytical methods or numerical tools such as FEM are generally used for simulations [58].

The electromagnetic problem is formulated, and solution strategies are proposed in the next subsection.

### 2.3. Electromagnetic Problem: A Semi-Analytical Solution

The problem of open-ended waveguide or box horn structures radiating in layered lossy medium is analyzed for two layered [59], and three layered tissue models [60]-[62] for hyperthermia applications. In this study, plane-wave spectral approach used in [61]-[63] is adopted. In [63], the solution is given for one layer, and in [60], for three layers. In this study, tissue is modeled by two homogeneous layers: skin and normal breast tissue. Spectral solution used for calculating radiated fields and mutual coupling between antennas is given for the two layered tissue model. The problem geometry is shown in Figure 2-2.

In order to couple the energy radiated from the open-ended waveguide to the tissue, dielectric loading is necessary. Water is used as filling material for the waveguide for this purpose.  $TE_{10}$  mode is assumed to be present on the aperture of the waveguide. Therefore, the broad-wall (a) and the narrow-wall (b) dimensions of the waveguide should be selected to justify  $TE_{10}$  mode. The thickness of the waveguide is taken as zero. The aperture is

assumed to be radiating in infinite ground plane so that the electric field is zero elsewhere [63]. The electric field at the aperture is in  $\hat{x}$ -direction. The field radiated by the waveguide is known to be TE to  $\hat{x}$  and  $\hat{y}$  everywhere [60], [64].

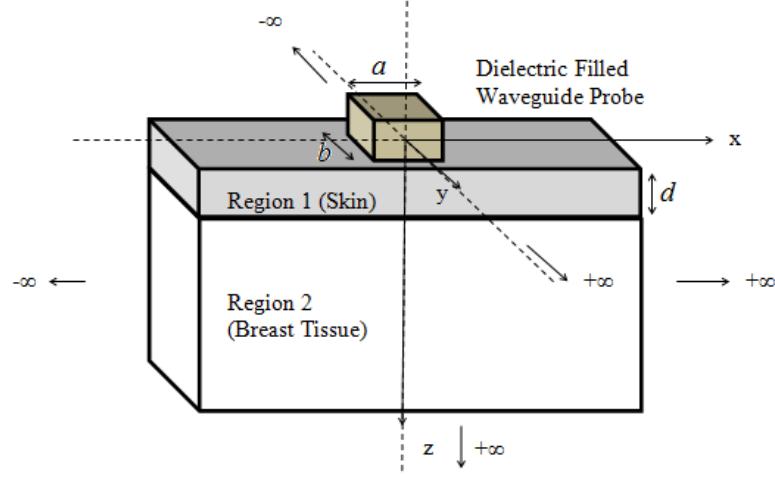


Figure 2-2: Problem geometry for the semi-analytical solution. Waveguide aperture is radiating into two-layered lossy half space. Geometry extends to infinity for  $\pm\hat{x}, \pm\hat{y}$  and  $+\hat{z}$  directions. Waveguide broad-wall and narrow-wall dimensions are  $a$  and  $b$ , respectively. Wall thickness of the waveguide is zero. Thickness of the skin is  $d$ .

The electric vector potential can be written as:

$$\vec{A}_m = \phi_n \hat{x} + \psi_n \hat{y} \quad (2-6)$$

Where  $\hat{x}$  and  $\hat{y}$  are the unit vectors in  $\hat{x}$  and  $\hat{y}$ -directions.  $\phi_n$  and  $\psi_n$  are the solutions of the wave equation in the  $n^{\text{th}}$  layer.

$$(\nabla^2 + k_n^2) \begin{Bmatrix} \phi_n \\ \psi_n \end{Bmatrix} = 0 \quad (2-7)$$

where  $k_n$  is the complex propagation constant in the  $n^{\text{th}}$  layer.

The spectral representations of  $\phi_n$  and  $\psi_n$  can be written in terms of the incident and reflected fields in region 1, and only the transmitted field in region 2, since it extends to infinity:

$$\begin{Bmatrix} \Phi_n(k_x, k_y, z) \\ \Psi_n(k_x, k_y, z) \end{Bmatrix} = \iint_{-\infty}^{+\infty} \begin{Bmatrix} \phi_n(x, y, z) \\ \psi_n(x, y, z) \end{Bmatrix} e^{jk_x x} e^{jk_y y} dk_x dk_y \quad (2-8)$$

In Region 1:

$$\begin{cases} \Phi_1(k_x, k_y, z) \\ \Psi_1(k_x, k_y, z) \end{cases} = \begin{cases} I_\Phi(k_x, k_y) \\ I_\Psi(k_x, k_y) \end{cases} e^{-jk_z z} + \begin{cases} R_\Phi(k_x, k_y) \\ R_\Psi(k_x, k_y) \end{cases} e^{+jk_z z} \quad (2-9)$$

In Region 2:

$$\begin{cases} \Phi_1(k_x, k_y, z) \\ \Psi_1(k_x, k_y, z) \end{cases} = \begin{cases} T_\Phi(k_x, k_y) \\ T_\Psi(k_x, k_y) \end{cases} e^{-jk_z z} \quad (2-10)$$

where  $k_x$  is the propagation constant in  $\hat{x}$ -direction, and  $k_y$  is the propagation constant in  $\hat{y}$ -direction,  $I_\Phi$  and  $I_\Psi$  are the incident,  $R_\Phi$  and  $R_\Psi$  are the reflected and  $T_\Phi$  and  $T_\Psi$  are the transmitted plane wave spectrums.

The electric and magnetic fields are given by:

$$\vec{E} = -\vec{\nabla} \times \vec{A}_m \quad (2-11)$$

$$\vec{H} = \frac{1}{j\omega\mu_0} [k_n^2 \vec{A}_m - \vec{\nabla}(\vec{\nabla} \cdot \vec{A}_m)] \quad (2-12)$$

where  $\mu_0$  is the permeability of the free space. The electric fields in region 1 can be written as:

$$E_{x_1}(x, y, z) = \frac{1}{4\pi^2} \iint_{-\infty}^{+\infty} [-jk_{z1} I_\Psi(k_x, k_y) e^{-jk_{z1} z} + jk_{z1} R_\Psi(k_x, k_y) e^{+jk_{z1} z}] e^{-jk_x x} e^{-jk_y y} dk_x dk_y \quad (2-13)$$

$$E_{y_1}(x, y, z) =$$

$$\frac{1}{4\pi^2} \iint_{-\infty}^{+\infty} [+jk_{z1} I_\Phi(k_x, k_y) e^{-jk_{z1} z} - jk_{z1} R_\Phi(k_x, k_y) e^{+jk_{z1} z}] e^{-jk_x x} e^{-jk_y y} dk_x dk_y \quad (2-14)$$

$$E_{z_1}(x, y, z) =$$

$$\begin{aligned} & -\frac{1}{4\pi^2} \iint_{-\infty}^{+\infty} jk_x [I_\Psi(k_x, k_y) e^{-jk_{z1} z} + R_\Psi(k_x, k_y) e^{+jk_{z1} z}] e^{-jk_x x} e^{-jk_y y} dk_x dk_y \\ & + \frac{1}{4\pi^2} \iint_{-\infty}^{+\infty} -jk_y [I_\Phi(k_x, k_y) e^{-jk_{z1} z} + R_\Phi(k_x, k_y) e^{+jk_{z1} z}] e^{-jk_x x} e^{-jk_y y} dk_x dk_y \quad (2-15) \end{aligned}$$



Similarly, the electric fields in region 2 can be written as:

$$E_{x_2}(x, y, z) = \frac{1}{4\pi^2} \iint_{-\infty}^{+\infty} [-jk_{z2} T_\psi(k_x, k_y) e^{-jk_{z2}z}] e^{-jk_x x} e^{-jk_y y} dk_x dk_y \quad (2-16)$$

$$E_{y_2}(x, y, z) = \frac{1}{4\pi^2} \iint_{-\infty}^{+\infty} [+jk_{z2} T_\phi(k_x, k_y) e^{-jk_{z2}z}] e^{-jk_x x} e^{-jk_y y} dk_x dk_y \quad (2-17)$$

$$E_{z_2}(x, y, z) = -\frac{1}{4\pi^2} \iint_{-\infty}^{+\infty} -jk_x [T_\psi(k_x, k_y) e^{-jk_{z2}z}] e^{-jk_x x} e^{-jk_y y} dk_x dk_y \\ + \frac{1}{4\pi^2} \iint_{-\infty}^{+\infty} -jk_y [T_\phi(k_x, k_y) e^{-jk_{z2}z}] e^{-jk_x x} e^{-jk_y y} dk_x dk_y \quad (2-18)$$

Magnetic fields can be written similarly using (2-12). Since TE<sub>10</sub> mode is assumed to be present at the aperture of the waveguide, the electric field at the aperture is of the form:

$$E_x(x, y, 0) = a_0(1 + \Gamma) \cos\left(\frac{\pi y}{b}\right) \quad (2-19)$$

$$E_y(x, y, 0) = 0 \quad (2-20)$$

where  $a_0$  is the mode amplitude at the waveguide surface, and  $\Gamma$  is the reflection coefficient at the waveguide-skin interface. The plane wave spectra in regions 1 and 2 can be solved using the continuity of tangential  $\vec{E}$  and  $\vec{H}$  fields at the boundaries:

$$E_{x1}(x, y, d) = E_{x2}(x, y, d) \quad (2-21)$$

$$E_{y1}(x, y, d) = E_{y2}(x, y, d) \quad (2-22)$$

$$H_{x1}(x, y, d) = H_{x2}(x, y, d) \quad (2-23)$$

$$H_{y1}(x, y, d) = H_{y2}(x, y, d) \quad (2-24)$$

Equations (2-21) to (2-24) are simultaneously solved for incident, reflected and transmitted plane wave spectrums  $I_\psi, I_\phi, R_\psi, R_\phi, T_\psi, T_\phi$  from which electric fields and magnetic fields are computed. Electric fields are computed using (2-13) to (2-18), where the integrals are computed numerically. Simpson's rule is used for the numerical integration.

Self and mutual admittance of the transmitting and receiving waveguides can be written as:

$$Y_{ij} = \frac{2P_{ij}}{|V_i||V_j|} = 2P_{ij} = \iint_{\substack{\text{Waveguide} \\ \text{Aperture}(i)}} (\vec{E}_i \times \vec{H}_j) \cdot \vec{d}\vec{s} \quad (2-26)$$

where  $P_{ij}$  is the Poynting vector on the waveguide surface,  $S$  is the surface of the waveguide.  $|V_{i,j}|$  is the voltage on the waveguide surface, which can be made unity with the choice of normalizing constant  $a_0 = \sqrt{\frac{2}{ab}}$  in (2-19). Using Parseval's theorem, (2-26) can be written as:

$$Y_{ij} = \frac{1}{4\pi^2} \iint_{-\infty}^{+\infty} E_{xi}^* \cdot H_{yj} dk_x dk_y = \frac{1}{4\pi^2} \iint_{-\infty}^{+\infty} [-jkz_1(-I_\psi + R_\psi)]^* \left[ \frac{(k_1^2 - k_y^2)}{j\omega\mu_0} (I_\psi e^{-jk_{z1}z} + R_\psi e^{+jk_{z1}z}) \right] dk_x dk_y \quad (2-27)$$

Wave impedance in the waveguide is given by [65]:

$$Y_0 = \frac{1}{120\pi} \sqrt{\epsilon_w} \frac{\lambda_w}{\lambda_g} \quad (2-28)$$

where  $\epsilon_w$  is the relative dielectric constant of the waveguide filling material,  $\lambda_w$  is the free-space wavelength of the waveguide filling material.  $\lambda_g$  is the guided wavelength in the waveguide with filling material.

Scattering parameters for the input reflection coefficient ( $S_{11}$ ) and the coupling coefficient ( $S_{21}$ ) between transmitting and receiving waveguide antennas can be calculated using:

$$S_{11} = \frac{1 - Y_{11}/Y_0}{1 + Y_{11}/Y_0} \quad (2-29)$$

$$S_{21} = -2 \frac{Y_{21}/Y_0}{(1 + Y_{11}/Y_0)^2 - Y_{21}/Y_0^2} \quad (2-30)$$

#### 2.4. Validation of the Semi-Analytical Solution

The semi-analytical solution is implemented in MATLAB, and its results are compared with the results of a commercial Finite Integration Time Domain (FITD) numerical solver, CST Microwave Studio (CST of America, Inc., MA, USA), on a sample problem. The geometry of the problem is shown in Figure 2-3. The parameters used in the sample problem are shown in Table 2-1. For the semi-analytical solution, the integration limits are chosen so that

the contribution of the outer portion is negligible. It is found that it is enough to integrate both  $k_x$  and  $k_y$  from  $-2500$  rad/m to  $2500$  rad/m since the contribution outside this region has negligible effect on the computed value. The integrand has a pole at  $k_x=0$ . Thus, integration boundaries for  $k_x$  are taken as  $[-2500,-\delta] \cup [\delta,2500]$ , where  $\delta$  is  $10^{-6}$  rad/m. The step size is also optimized to get the correct value with largest step in order to reduce the calculation time. It was decreased until the amplitude of the  $E_x$  field is converged within  $10^{-4}$  of the field value at the aperture of the waveguide. The optimized step size used in the integrations was  $5$  rad/m. The cut-off frequency of the waveguide probes is calculated to be  $1.25$  GHz, for the waveguide dimensions given in Table 2-1.

In CST simulations, to simulate the infinite extent of the medium, the boundaries of the problem are terminated with Perfectly Matched Layer in all directions. The mesh size in the problem is set to  $\lambda/18$  in  $\hat{x}$ ,  $\hat{y}$  and  $\hat{z}$  directions. The mesh size is adaptively decreased from  $\lambda/10$  in order to get  $0.005$  convergence in the S-parameters. Results are calculated with ports de-embedded to the aperture of the waveguides.

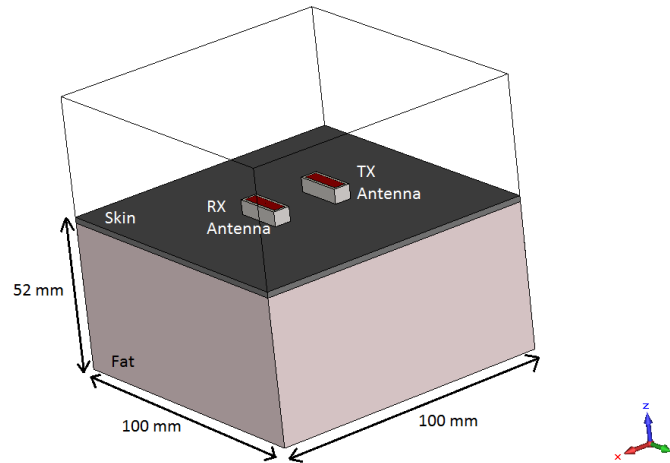


Figure 2-3: Sample problem geometry (CST MWS). TX (Transmitting) and RX (Receiving) antennas are placed on two layered medium. Boundaries are terminated with Perfectly Matched Layer (PML).

The electric field components  $E_x$  and  $E_z$  normalized to the electric field at the antenna aperture are calculated at the midline of the waveguides semi-analytically and numerically. They are plotted as a function of depth in Figure 2-4 for comparison. The value of electric field at the aperture of the waveguide is taken to be  $1\text{V/m}$  for both solutions. The semi-analytically and numerically calculated values for the magnitude of the  $S_{11}$  and  $S_{21}$  parameters are given in Table 2-2. The electric field values and the S-parameters found consistent using both solution techniques.

Table 2-1: Parameters Used in the Sample Problem

<b>Frequency</b>	GHz	5
<b>Waveguide dimensions</b>	a (mm)	13.7
	b (mm)	3.4
<b>Thickness of the skin layer</b>	d (mm)	2
<b>Distance between transmitting and receiving waveguides</b>	s (mm)	20
<b>Relative dielectric constants</b>	Skin[22]	39.61-j12.86
	Fat [72]	4.48-j0.75
	Water	77.15-j15.86

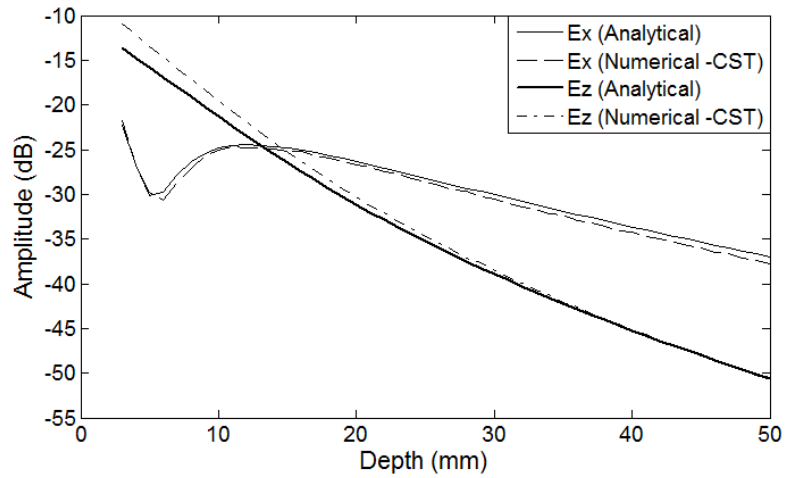


Figure 2-4: Normalized E-field components at the mid-line of waveguides obtained with semi-analytical and numerical solvers.

Table 2-2: Comparison of S-Parameters from Semi-analytical and Numerical Results

<b>Parameter</b>	Semi-Analytical (dB)	Numerical (dB)
<b>S<sub>11</sub></b>	-10.72	-10.65
<b>S<sub>21</sub></b>	-28.34	-28.77

## 2.5. Received Signal Due To Electrically Small Tumor

In the proposed system, the receiver is sensitive to the signal scattered from the moving region in the tissue. In order to calculate the received signal, static problem is considered first. The effect of the harmonic motion of the local region will be added next. In the static problem, it is assumed that the tissue is homogeneous, and a spherical tumor is introduced with different electrical permittivity into otherwise homogeneous tissue. If the diameter of the tumor is much less than the wavelength of operation, the polarization density inside the tumor can be written as [66]:

$$\vec{P} = \frac{3\varepsilon_b(\varepsilon_t - \varepsilon_b)}{\varepsilon_t + 2\varepsilon_b} \varepsilon_0 \vec{E}_{inc} \quad (2-31)$$

where  $\varepsilon_0$  is the permittivity of the free space,  $\varepsilon_t$  is the relative permittivity of the tumor,  $\varepsilon_b$  is the relative permittivity of the surrounding medium,  $\vec{E}_{inc}$  is the incident electric field on the tumor. The wavelength inside the tissue can be calculated as  $\lambda_b = \frac{2\pi c}{\omega\sqrt{\varepsilon_b}}$ , where  $c$  is the speed of light. The diameter of the tumor used in this study is 3 mm, which is about  $1/10^{\text{th}}$  of the wavelength inside breast fat at 5 GHz.

The tumor can be modeled with a polarization current density  $\vec{J} = j\omega\vec{P}$ . The received signal due to this current density can be found using Lorentz reciprocity theorem (Figure 2-5):

$$\int_{\substack{\text{Tumor} \\ \text{Volume}}} (\vec{E}_1 \cdot \vec{J}_2) dV = \int_{\substack{\text{Waveguide} \\ \text{surface}}} [\vec{E}_2 \cdot \vec{J}_1 - \vec{H}_2 \cdot \vec{M}_1] dS \quad (2-32)$$

where  $\vec{J}_2$  is the electric current density representing the tumor.  $\vec{E}_2$  and  $\vec{H}_2$  are the electric and magnetic fields radiated by this current density on the waveguide surface. In the reciprocal problem,  $\vec{E}_1$  and  $\vec{H}_1$  are the electric and magnetic fields radiated by the receiving antenna.  $\vec{J}_1$  and  $\vec{M}_1$  are the electric and magnetic current source density on the waveguide surface.

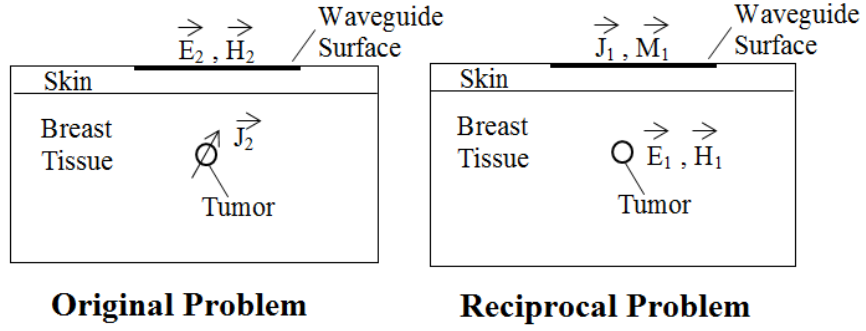


Figure 2-5: Illustration of the original and the reciprocal problems.

The right hand side of (2-32) is the coupling admittance of the dipole to waveguide multiplied by the voltages of the transmitting and receiving waveguides. The mutual admittance of the dipole and the receiving antenna can be written as:

$$Y_{21t} = \frac{1}{|V_1||V_2|} \int_{\substack{\text{Tumor} \\ \text{Volume}}} \vec{E}_1 \cdot \vec{J}_2 dV = \frac{2}{ab} j\omega\epsilon_0 \frac{3\epsilon_b(\epsilon_t - \epsilon_b)}{\epsilon_t + 2\epsilon_b} \vec{E}_{inc} \cdot \vec{E}_1 v \quad (2-33)$$

where  $|V_1|$  and  $|V_2|$  are the voltages of the transmitter and receiver waveguide aperture fields, and  $v$  is the volume of the tumor. In (2-33), if the field amplitudes on the waveguide apertures are made unity, normalizing constant  $\sqrt{\frac{2}{ab}}$  can be applied to both receiving and transmitting antennas, in order to have unity voltage at the apertures. Then the coupling admittance between the tumor and the receiving antenna can be written as:

$$Y_{21t} = \frac{2}{ab} j\omega\epsilon_0 v \frac{3\epsilon_b(\epsilon_t - \epsilon_b)}{\epsilon_t + 2\epsilon_b} \vec{E}_{inc} \cdot \vec{E}_1 \quad (2-34)$$

The coupling S-parameter due to tumor can be calculated in a similar manner as in (2-30):

$$S_{21t} = -2 \frac{Y_{21t}/Y_0}{(1 + Y_{11}/Y_0)^2 - Y_{21t}/Y_0^2} \quad (2-35)$$

The signal at the receiving antenna when the ultrasound radiation force is applied will also depend on the displacement amplitude of the moving region which is given by (2-5). In the next section, the effect of vibration on the scattered signal is discussed.

## 2.6. The Effect of Vibration

When the tissue is illuminated by ultrasound for harmonic motion, assuming the vibrating region occupies the electrically small spherical tumor and the whole volume of the tumor is in harmonic motion, the phase and amplitude of the scattered signal changes harmonically with the frequency of vibration.

In the system, an interrupted continuous-wave microwave signal is transmitted to the tissue which has a local harmonic motion at the region of the focus of the ultrasound transducer. If the output signal from the transmitter antenna is  $S_{TX}(t) = A \cos(\omega_m t)$ , the scattered signal at the receiving antenna due to vibrating dipole can be written as:

$$S_{RX}(t) = B[1 + M \sin(\Delta\omega t)] \cos\left(\omega_m t + \frac{4\pi R}{\lambda} + K \sin(\Delta\omega t) + \phi\right) \quad (2-36)$$

where  $B$  is the magnitude of the received signal for the case without vibration,  $R$  is the distance from antennas to locally vibrating tumor,  $\omega_m$  is the operating frequency of the radar,  $\Delta\omega$  is the vibration frequency of the tissue,  $M$  and  $K$  are the change in amplitude and phase of the signal respectively. It is assumed that the tumor is displaced a maximum amount of  $X_0$  and the vibrating region is on the mid-plane between transmitting and receiving antennas.  $X_0$  is in the order of micrometers and the effect of amplitude modulation ( $M \ll 1$ ) can be neglected. The cosine term in the right hand side of (2-36) can be expressed as:

$$\begin{aligned} \cos\left(\omega_m t + \frac{4\pi R}{\lambda} + K \sin(\Delta\omega t) + \phi\right) &= \cos\left(\omega_m t + \phi + \frac{4\pi R}{\lambda}\right) \cdot \cos(K \sin(\Delta\omega t)) \\ &\quad - \sin\left(\omega_m t + \phi + \frac{4\pi R}{\lambda}\right) \cdot \sin(K \sin(\Delta\omega t)) \end{aligned} \quad (2-37)$$

Since  $K$  is very small ( $K \ll 1$ ), cosine and sine terms resulting from the displacement can be written as:

$$\cos(K \sin(\Delta\omega t)) \approx 1 \quad (2-38)$$

$$\sin(K \sin(\Delta\omega t)) \approx K \sin(\Delta\omega t) \quad (2-39)$$

Equation (2-37) can be written as:

$$\begin{aligned} \cos\left(\omega_m t + \frac{4\pi R}{\lambda} + K \sin(\Delta\omega t) + \phi\right) \\ = \cos\left(\omega_m t + \phi + \frac{4\pi R}{\lambda}\right) - \sin\left(\omega_m t + \phi + \frac{4\pi R}{\lambda}\right) \cdot K \sin(\Delta\omega t) \end{aligned} \quad (2-40)$$

The scattered signal is then:

$$S_{RX}(t) = B \left\{ \cos \left( \omega_m t + \phi + \frac{4\pi R}{\lambda} \right) + \frac{K}{2} \cos \left( \omega_m t - \Delta\omega t + \frac{4\pi R}{\lambda} + \phi \right) - \frac{K}{2} \cos \left( \omega_m t + \Delta\omega t + \frac{4\pi R}{\lambda} + \phi \right) \right\} \quad (2-41)$$

The scattered signal has a component at the operating ( $\omega_m$ ) frequency and also two different main frequency components at ( $\omega_m + \Delta\omega$ ) and ( $\omega_m - \Delta\omega$ ). The component of the received signal at  $\omega_m$  angular frequency may practically be very small compared to clutter and leakage. Since  $\Delta\omega$  is known, Doppler filters and other components in the receiving circuitry can be optimized for sensing this frequency component. The bandwidth of the receiver, thus, can be made minimum to increase SNR.

Since the Doppler frequency is known beforehand, signal can be down-converted and filtered. Using (2-35) and (2-41), coupled signal amplitude at the Doppler frequency is then given by:

$$S_{21t,doppler} = -2 \frac{\frac{Y_{21t}}{Y_0}}{\left(1 + \frac{Y_{11}}{Y_0}\right)^2 - \frac{Y_{21t}^2}{Y_0}} \frac{K}{2} \quad (2-42)$$

In general, for any position of the tumor with respect to the antennas including the near field region, maximum deviation in phase  $K$  should be calculated for a given  $X_0$  using the phase of  $S_{21t}$  (2-35).

## 2.7. Mechanical Problem

To solve the mechanical part of the problem, solid mechanics module of commercially available finite element solver COMSOL Multi-physics is used. The acoustic intensity distribution inside the tissue generated by the focused ultrasound probe is obtained by the HIFU simulator tool developed by U.S Food and Drug Administration (FDA) [67]. This MATLAB tool solves axi-symmetric Khokhlov-Zabolotskaya-Kuznetsov (KZK) equation [68] in the frequency domain. A transducer that has 2.1 cm outer radius, 1 cm inner radius, and 6 cm focusing depth is simulated at 3.3 MHz. 150 harmonics are included in the simulation. 3.5 cm water layer is assumed to be present between 5.5 cm normal breast (fat) tissue and the transducer. The focus of the transducer is at 2.5 cm depth inside the tissue. From the simulations, the axial and lateral intensity beamwidths are obtained as 6.75 mm and 0.48 mm, respectively. Spatial peak-pulse average value of intensity ( $I_{SPPA}$ ) for the amplitude modulated ultrasound beam is 175 W/cm<sup>2</sup>. The normalized intensity map obtained using this simulation is given in Figure 2-6. The force due to this intensity is applied to the tissue sinusoidally, using (2-1), as a volume body load, for frequencies 100 Hz, 250 Hz, and 500 Hz. Since the beam is axially symmetric, axial symmetry is assigned to the mechanical problem in order to reduce the computational cost. The loss in the intensity of the ultrasound beam due to the presence of the skin layer and the tumor is not taken into account since the



reflection due to acoustic impedance mismatch is about 1% in soft tissues [69]. By this way, the displacement is analyzed for the same amount of ultrasound intensity at the focus in all cases.

Breast tissue is modeled as a homogeneous material having a Young's constant of 5 kPa and a Poisson's ratio of 0.495. The chosen value of Young's constant is between the reported mean values of normal breast fat/fibro-glandular tissue and fibro-adenoma tissue [44]. Tumor is modeled as a sphere of radius 1.5 mm having a Young's constant of 20 kPa and a Poisson's ratio of 0.495. This value is the reported mean value for intermediate-grade invasive ductal carcinoma [44]. The other parameters used in the simulations are listed in Table 2-3. Two snapshots at the first and the sixth maximum displacement instants for normal breast tissue at 250 Hz difference frequency are given in Figure 2-7. The resultant displacements for the normal breast tissue at the first peak focal displacement are plotted for the lateral and axial cuts in Figure 2-8 (a) and (b), respectively. The displaced region width (DRW) can be defined as the width of the region where the displacement decreases to a half of the displacement at the focal point. The lateral and axial DRW values are given in Table 2-4 2-4. DRW is larger than the intensity beamwidth as expected. DRW can be used as a metric to assess the imaging resolution of the method. It is greater in the axial direction. Therefore, the resolution relatively low (8-13 mm) in the axial direction. However, higher resolution (1.5-3 mm) can be achieved in the lateral dimension. The beam properties of the transducer affect the resolution of the system, and using larger transducers, it is possible to decrease the DRW to achieve high resolutions. However, as the DRW gets narrower, the scattered electromagnetic power at the Doppler frequency is decreased since the displaced portion of the tissue is smaller.

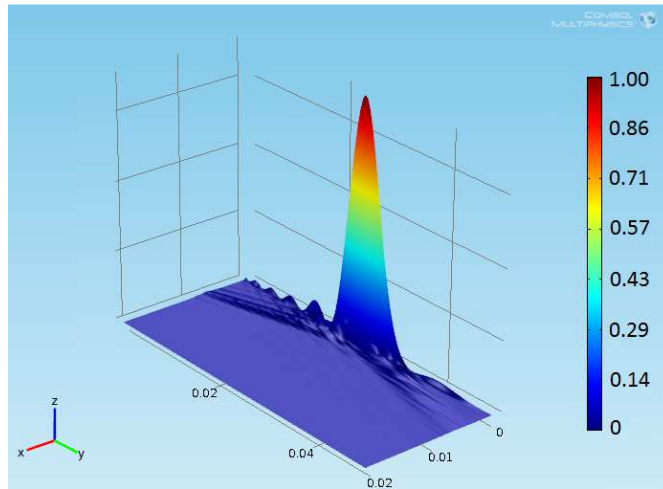


Figure 2-6: Axially symmetric ultrasound intensity (normalized) map inside the tissue for mechanical simulations. A focused ultrasound transducer is placed at  $-\hat{y}$  end. 3.5 cm water layer is not shown.

Because of the induced shear waves due to vibration, there are some ripples in the displacement map (Figure 2-7 (b)). This is undesirable since these waves may also change the phase and amplitude of the scattered electromagnetic wave. Lateral cut displacement distribution for the late time peak is plotted in Figure 2-8(c). The effect of shear waves may be significant since the displacement outside the focus goes up to 30-40% of the focal displacement. This effect should be investigated in realistic numerical simulations. If they are effective, one solution may be limiting the duration of the ultrasound wave and taking the electromagnetic measurement data in the first few cycles of the displacement.

The attenuation constant and the elastic constant have opposing effects on the displacement. For tumor, high attenuation constant increases the displacement while high elastic constant tends to decrease it. Fibro-glandular tissue has high attenuation constant, but lower elastic constant compared to the tumor that lead to higher displacement values. For fat tissue, attenuation is smaller, which results in a smaller displacement. The results in Table 2-4 include these effects. Although the attenuation value of the tumor is greater than the attenuation value of the fat tissue, the displacement is found to be smaller since the ratio of elastic constants (1:4) dominates over the ratio of attenuation constants (1:2.3) for fat and tumor tissues. Fibro-glandular tissue has the highest displacement values since the attenuation coefficient is greater. This is desirable for especially detecting tumors located inside the fibro-glandular tissue. Another important observation is that the displacement of the tumor is nearly halved when the frequency is increased by a factor of two. However, this is not the case for the normal tissues. The ratio of the displacement for fibro-glandular tissue and the tumor is given in Table 2-4 for different excitation frequencies. This property can also be used to distinguish tumors from normal tissue in conjunction with the electromagnetic scattering properties.

Table 2-3: Parameters Used in Mechanical Simulation

<b>Young's Modulus</b> [44]	<b>Breast tissue</b>	5 kPa
	<b>Tumor</b>	20 kPa
<b>Poisson's ratio</b>	<b>All tissues</b>	0.495
<b>Ultrasonic attenuation</b> [70]	<b>Breast Fat</b>	0.34 dB/cm/MHz
	<b>Fibro glandular</b>	1.5 dB/cm/MHz
	<b>Tumor</b>	0.79 dB/cm/MHz
<b>Ultrasound speed</b> [71]	<b>Breast Fat</b>	1479m/s
	<b>Fibro glandular</b>	1553 m/s
	<b>Tumor</b>	1550 m/s
<b>Focal width (FWHM) of the transducer</b>		0.48
<b>Focal depth (FWHM) of the transducer</b>		6.75
<b>Intensity (<math>I_{SPPA}</math>) of the ultrasound beam</b>		175 W/m <sup>2</sup>
<b>Number of elements in the Finite Element model</b>		4308
<b>Maximum element size in the Finite Element model</b>		0.8 mm

Table 2-4: Displacement beam widths and maximum displacement values

Freq. (Hz)	Lateral DRW (mm)	Axial DRW (mm)	Displacement of the tumor ( $\mu\text{m}$ )	Displacement of fat tissue ( $\mu\text{m}$ )	Displacement of fibroglandular tissue ( $\mu\text{m}$ )	Ratio (tumor/fibroglandular)
125	3	12.6	2.94	4.8	8.75	2.97
250	2.2	9.6	1.55	1.8	7.5	4.83
500	1.4	8.2	0.7	1.65	5.25	7.5

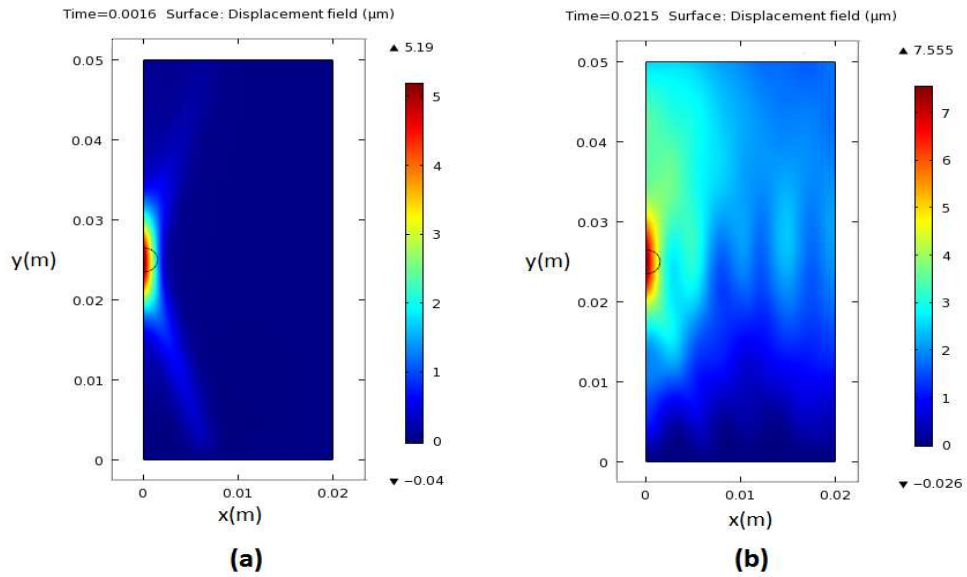


Figure 2-7: Snapshots at the maximum displacement instant for normal breast tissue at 250 Hz vibration frequency at the first displacement peak (a), and the sixth displacement peak (b) at the focus.

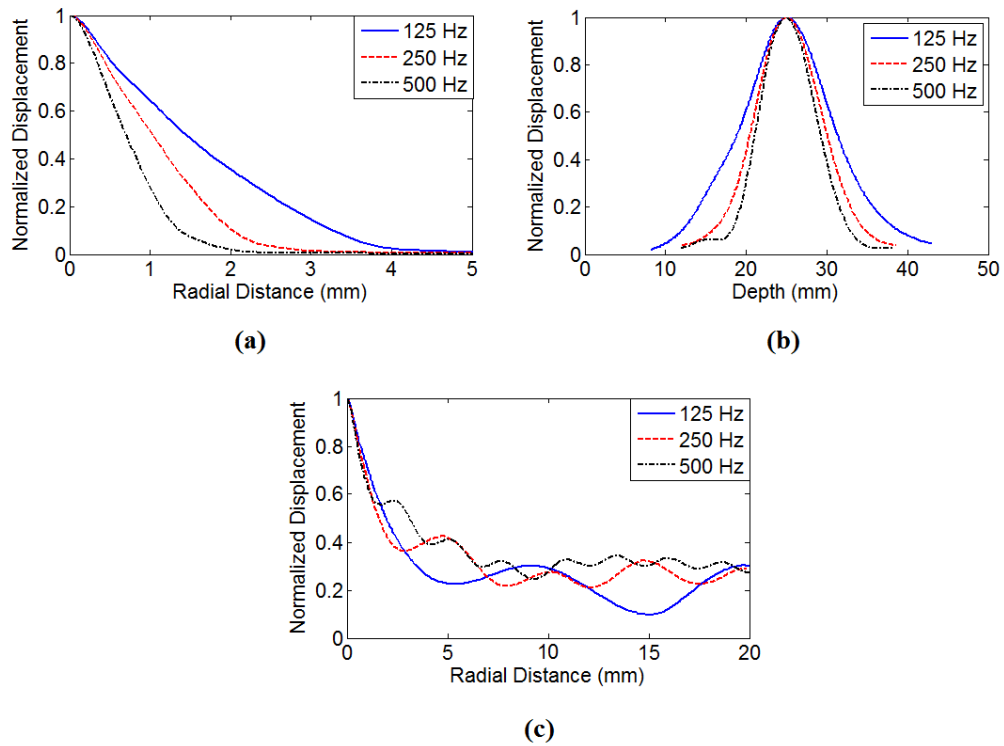


Figure 2-8: Normalized lateral (a) and axial (b) displacement cuts for the first displacement peak at the focus. Normalized lateral displacement for the late time displacement peak at the focus (c).

## 2.8. Results

The received microwave signal amplitude, which depend on the electromagnetic and mechanical properties of the breast tissue, are presented in this section for different scenarios, using the formulation given in the previous sections. In order to obtain realistic results, dielectric and elastic properties of the breast tissue used in the solutions must be accurate. In a large scale study for the dielectric properties of the breast, tissue is grouped into three types according to the adipose content, for which the dielectric properties are different ([34]-[35]). Tissues with low adipose, higher fibro-connective and glandular content have higher dielectric constant (approaching to malignant tissues) whereas tissues having high adipose content have lower dielectric constant. In this study, the two-pole Debye model presented in [72] is used. For the skin layer, wet skin dielectric properties [22] are used. Water filled open ended waveguide probes are used for microwave signal transmission and reception. The vibration amplitude is taken as  $2.5 \mu\text{m}$  in the analyses, which is similar to the 125 Hz displacement amplitude value of tumor obtained in Section 2.7.

When the tissue is exposed to focused ultrasound for harmonic motion, the locally displaced region is in the form of an ellipsoid. As seen in Figure 2-8, this region is larger than the focal

dimensions of the transducer. It is narrower in the axial direction and broader in elevation and lateral directions. The malignant region may be totally or partially inside this ellipsoid, or it may be larger than the ellipsoid, depending on the dimensions of the malignant region, frequency of ultrasound and transducer dimensions. In this study, the malignant tissue is assumed to be spherical, small and totally inside the locally displaced region.

### **2.8.1. Microwave Operation Frequency**

The selection of the microwave operating frequency is an important parameter which directly affects the received signal amplitude. Therefore, optimum value for frequency should be chosen. The geometry of the problem used in the analysis is shown in Figure 2-9. The Doppler frequency component of the received signal at the receiving antenna aperture is plotted as a function of frequency in Figure 2-13 for different breast tissue types using (2-42). In the analysis, transmitting output power is 1 Watt, the tumor has 1.5 mm radius, and depth of the tumor measured from the top of the skin layer is 3 cm. The maximum displacement of the tumor is 2.5  $\mu\text{m}$ .

The transmitting and the receiving antennas are assumed to be water filled waveguides having broad-wall size of  $2 \lambda_w$  ( $\lambda_w$ : electromagnetic wavelength in water) and narrow wall size of  $0.5 \lambda_w$ . By this choice of waveguide dimensions, electrical aperture size for each frequency remains constant for comparison. The distance measured between the near edges of the antennas is 2 cm.

The results show that if the tissue is mostly fatty, optimum choice of microwave frequency is nearly 5 GHz. The waveguide aperture dimensions are 13.7 mm x 3.4 mm for this frequency. The magnitude of the received signal decreases no more than 3dB between 3.25-7 GHz bandwidth. For high and medium adipose content tissues, optimum frequency of operation is 2.1 GHz and the signal decreases no more than 3dB between 1.75-3.25 GHz. Maximum level of the received signal for the low adipose content tissue case is nearly 15 dB lower than the high adipose content tissue case. This is a result of higher attenuation property of the background tissue, as well as the low permittivity difference between the tumor and the surrounding tissue. Note that this is the worst case scenario as whole of the tissue is assumed to be low adipose content tissue. Since, the optimum operation frequency is different for high and medium-low adipose content tissues, a dual (or multiple) frequency system which operates at 2.1 GHz and 5 GHz may be preferable for detecting tumors in all kind of tissues.

In practice, data can be taken for both frequencies (there may be also intermediate frequencies) and the frequency for the best SNR performance can be used to generate the image, since tissue adipose content varies inside the tissue.

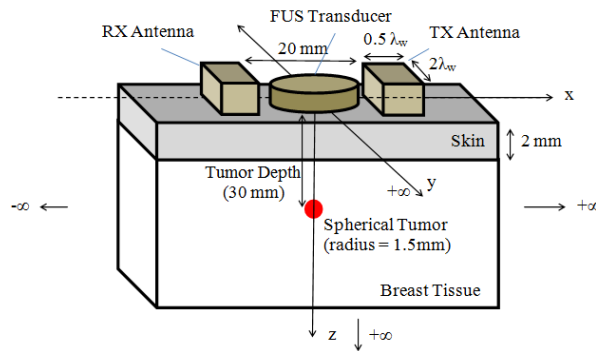


Figure 2-9: Geometry for the microwave operation frequency analysis. Spherical tumor of 1.5 mm radius is introduced at 3 cm depth measured from the top of the skin layer.

### 2.8.2. Tumor in Fibro-glandular Tissue

What if the tumor is located inside a low adipose content tissue for which the dielectric properties are similar to the malignant tissue (Figure 2-11)? This case is investigated assuming most of the tissue has high adipose content, and neglecting the attenuation of the fibro-glandular tissue. The backscattered signal is thus only affected because of the low contrast of permittivity values between the low adipose content tissue and the tumor. The signal level is found to be only 4 dB lower than the case that the tumor is located inside high adipose content tissue in this case. This result shows that the method is capable of sensing the signals from the tumor even if it is in fibro-glandular tissue. Note that the fibro-glandular tissue is also a scattering source and the discrimination of tumor inside the fibro-glandular is discussed in the following subsection.

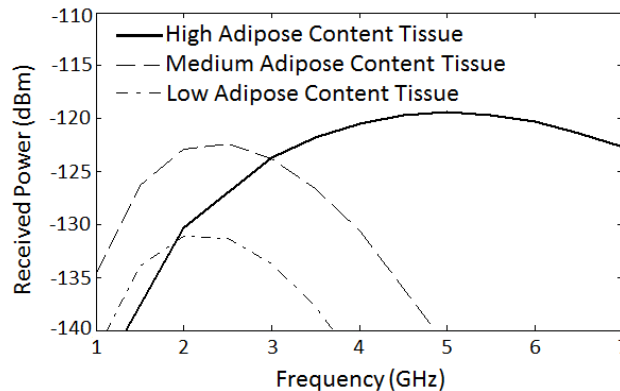


Figure 2-10: Scattered signal level (at the Doppler frequency) as a function of frequency for different tissue types. Solid line (—): high adipose content tissue, dashed line(- -): medium adipose content tissue. Dash dotted line (- · - ·): low adipose content tissue. (Tumor radius: 1.5 mm, tumor depth: 30 mm, probe separation: 20 mm, probe alignment: E-plane, max. displacement of tumor: 2.5  $\mu$ m).

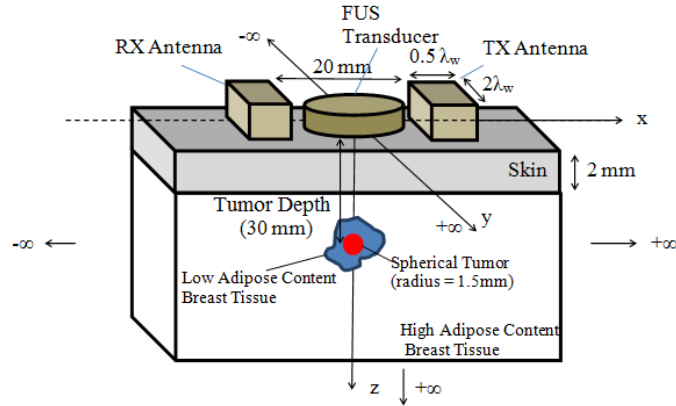


Figure 2-11: Geometry for the case, in which the tumor is inside low adipose content tissue. Spherical tumor of 1.5 mm radius is introduced at 3 cm depth measured from the top of the skin layer, inside the low adipose content tissue.

### 2.8.3. Replacing the Tumor with a Spherical, Electrically Small, Low Adipose Content Tissue

During a scan, if there is an increase in the received signal level, it may be due to a low adipose content tissue or tumor. In order to make a decision about malignancy, the vibration frequency response can be used. If the frequency of the harmonic motion is increased, the maximum displacement of the local region decreases substantially if the focus is at the malignant region (Table 2-4). A benign/malign decision can be made by comparing the difference between the signal levels obtained from two or more harmonic motion frequencies. Therefore, it is better to have a system capable of acquiring multiple frequency harmonic motion images in order to get reliable results for tumor detection. In addition, when the ultrasound is focused inside a fibro glandular region, scattering from the boundaries of the fibro-glandular tissue increases the backscattered signal at the Doppler frequency. If there is a tumor inside the fibro-glandular region, when the ultrasound is focused on it, the displacement and the backscattered signal level will decrease.

### 2.8.4. Distance and Alignment of the Waveguide Probes

The distance between waveguide probes and their alignment (Figure 2-12) affects the received signal level and the coupling between probes. Received signal level at the Doppler frequency component is plotted in Figure 2-13 as a function of probe separation, for two cases in which the probes are aligned in their narrow wall direction (E-plane) and broad wall direction (H-plane).

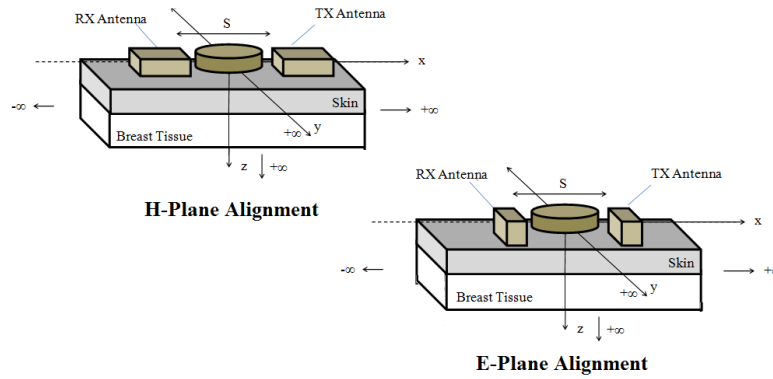


Figure 2-12: Geometry for E-plane and H-plane Alignment of Waveguide Probes

It is better minimize the probe distance for both types of alignments. However, for the E-plane alignment, one must be careful about the local minima caused by the polarization mismatch between probes. Consequently, H-plane alignment is considered as a better choice. In practice, especially due to phase noise, the transmitted signal will have a spread spectrum that also falls in the Doppler frequency range of the moving region. Because of this, the directly coupled signal may mask the scattered Doppler frequency signal. Thus, it is desirable to have high isolation between the probes. Figure 2-14 shows the ratio of direct coupling between the probes to the scattered signal from tumor at the Doppler frequency for both cases. Directly coupled signal from the transmitting probe is found to be 20 dB to 35 dB higher for E-plane aligned probe than the H-plane alignment case.

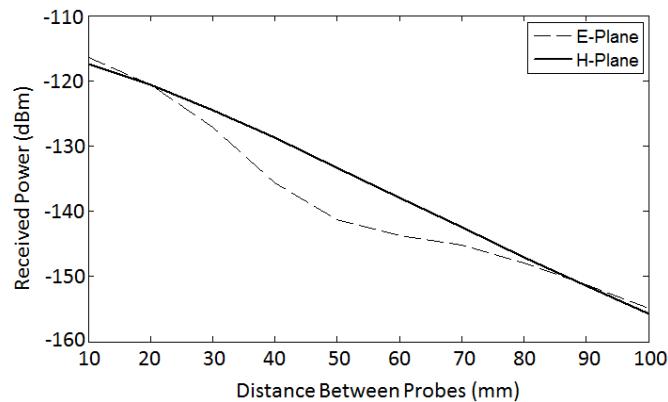


Figure 2-13: Scattered signal (at the Doppler frequency) as a function of antenna distance for E-plane and H-plane aligned antennas. Solid line (—): H-plane alignment, dashed line (---): E-plane alignment (Tumor radius: 1.5 mm, tumor depth: 30 mm, max. displacement of tumor: 2.5  $\mu$ m, TX Power: 1 W).



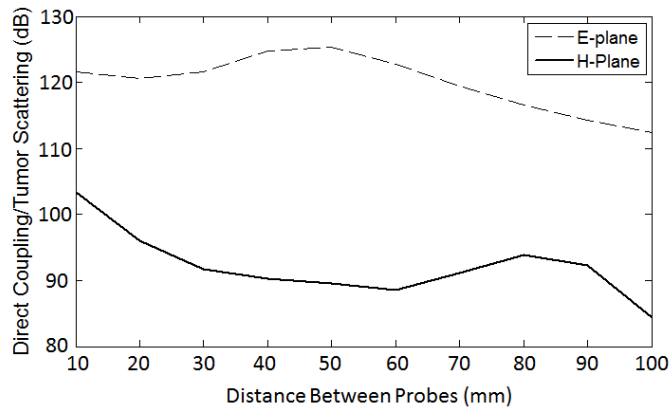


Figure 2-14: Direct probe coupling to the scattered signal (at the Doppler frequency) ratio as a function of probe distance for E-plane and H-plane aligned probes. Solid line (—): H-plane alignment, dashed line (---): E-plane alignment (Tumor radius: 1.5 mm, tumor depth: 30 mm, max. displacement of tumor: 2.5  $\mu\text{m}$ ).

### 2.8.5. Effect of Tumor Depth in Received Signal

The received signal level for a spherical tumor is plotted as a function of tumor depth for E-Plane and H-Plane probe alignment in Figure 2-15 (for 1.5 mm tumor radius, 2.5  $\mu\text{m}$  maximum displacement, 20 mm probe separation, 5 GHz frequency, 1 Watt TX output power). The received signal level for the E-plane alignment case is higher than the H-plane alignment case when the tumor is near to the surface up to 15 mm. The signal level decreases for higher depths because of the polarization mismatches. However, since the phase gradient is larger at this point, the local minimum (i.e. the decrease in signal level at the Doppler frequency) is not severe. The signal level then starts to decrease monotonically with 0.6 dB/mm. In the H-plane aligned probe case, the signal level is too low at the surface, which is caused by the small phase gradient. It increases as the depth is increased to 15 mm. There is no polarization mismatch in this configuration since the electric fields of receiving and transmitting probes are parallel everywhere. For depths beyond 25 mm, the response for both alignments is similar. It can be concluded that the E-plane alignment is better in terms of received Doppler signal amplitude, especially for shallow regions.

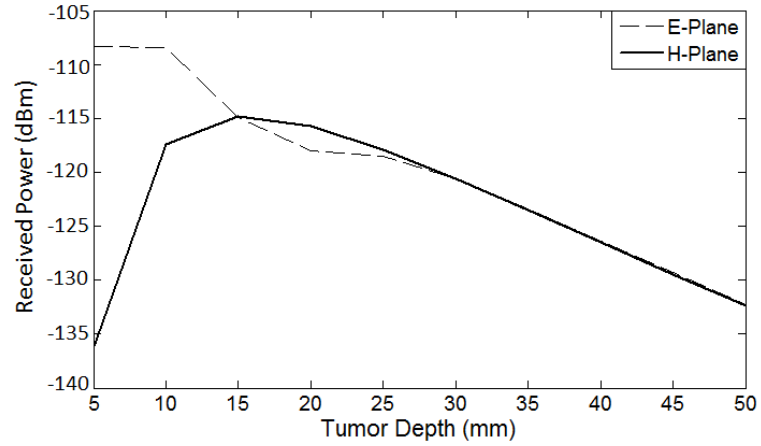


Figure 2-15: Scattered signal (at the Doppler frequency) level as a function of tumor depth for 5 GHz frequency with E and H plane probe alignments. Solid line (—): H-plane alignment, dashed line (---): E-plane alignment (Tumor radius: 1.5 mm, probe separation: 20 mm, max. displacement of tumor: 10  $\mu$ m).

### 2.8.6. Receiver Sensitivity

In order get an idea of the systems performance capability, the required received power can be calculated by making some assumptions. Assuming a heterodyne receiver is used, in which the RF signal is down-converted to an Intermediate Frequency (IF) signal, minimum detectable signal level at the microwave receiver can be written as [74]:

$$S_{min} = k_b T B_n F_n \left(\frac{S_0}{N_0}\right)_{min} \quad (2-43)$$

Where  $k_b$  ( $1.3806504 \times 10^{-23}$  J/K) is the Boltzman constant,  $T$  (290°K) is the noise temperature of the receiver,  $F_n$  is the noise figure of the receiver,  $B_n$  is the IF bandwidth of the receiver, and  $\left(\frac{S_0}{N_0}\right)_{min}$  is the minimum SNR to detect the signal.

Assuming 20dB SNR, 10 dB noise figure, and 100 Hz IF Bandwidth, the received signal power should be greater than:

$$S_{min} = -153 \text{ dBm} + 10 + 20 = -123 \text{ dBm} \quad (2-44)$$

If microwave output power is 1 W (30 dBm), considering only thermal noise, detection of signals from spherical tumors having 1.5 mm radius up to 35 mm depth in high adipose content tissue seems feasible, assuming 2.5  $\mu$ m displacement is given locally by focused ultrasound (Figure 2-15).

This calculation involves only the thermal noise at the receiver. Another limiting factor is that the received signal power level at the Doppler frequency should be greater than the phase noise of the coupled signal from the transmitter at those Doppler frequencies. In the system design, the transmitter power levels of the ultrasound and RF, and also the vibration frequency and RF frequency should be selected carefully in order to acquire reliable data for image formation.

## **2.8.7. Safety**

### **2.8.7.1. Microwave Exposure**

In order to get a reliable signal level at the receiver, the transmitted power should be high, but it must be low enough not to harm the healthy tissue. The specific absorption rate (SAR) value of the tissue which is exposed to microwave signal is a criteria to investigate the safety of the system. The temperature rise inside the tissue is less than 1°C for 30 minutes exposure to SAR values between 1 W/kg to 4 W/kg [75]. The SAR value for microwave exposure is calculated and plotted as a function of depth at the midline of the transmitter probe (which is the maximum value at a certain depth) at 5 GHz when the output power of the probe is 1 Watt (Figure 2-16). It is observed that the mostly affected region is the tissue surface. Neglecting the blood perfusion and the thermal conduction, temperature rise due to microwave exposure in the worst case can be calculated as:

$$\Delta T_m = \frac{SAR}{\gamma_w} t \quad (2-45)$$

where  $\gamma_w$  is the tissue effective specific heat in J/(kgK) and  $t$  is the microwave exposure time.  $\gamma_w$  for skin tissue is 3500 [76]. For a 3W/kg SAR value, 19 minutes of continuous wave (CW) exposure results in 1°C temperature rise in the skin tissue. The output power may be increased beyond 1 Watt without harming the tissue to increase detection capability.

### **2.8.7.2. Ultrasound Exposure**

Ultrasound radiation has thermal effects that lead to temperature rise in the tissue and non-thermal effects like cavitation that is expansion and contraction, or collapse of gas bubbles. The limit for ultrasound field intensity as restricted by U.S Food and Drug Administration (FDA) is 190 W/cm<sup>2</sup> spatial peak pulse-average intensity ( $I_{SPPA}$ ) [77]. The intensity for the mechanical simulations in Section 2.7 is 175 W/cm<sup>2</sup>, which is below the limit.

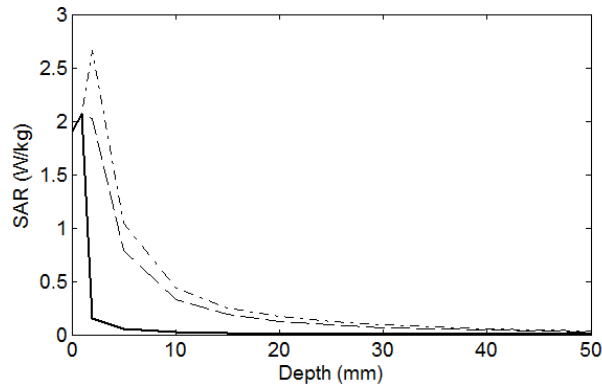


Figure 2-16: SAR value as a function of depth at the midline of the transmitter probe at 5 GHz for 1Watt probe output power. Solid line (—): high adipose content tissue, dashed line (---): medium adipose content tissue, dash dotted line (- · - ·): low adipose content tissue.

### ***Thermal Index***

Absorption of the ultrasound energy heats the tissue. If convection and conduction of heat inside the tissue is not taken into account, the temperature rise for the worst case can be calculated by:

$$\Delta T_u = \frac{2\alpha I}{\gamma_v} t$$

where  $\gamma_v$  is the volume specific heat of the tissue and  $t$  is the ultrasound exposure time. Temperature rise less than  $1^\circ\text{C}$  is considered to be acceptable by the National Council on Radiation Protection and Measurements (NCRP [79]). The Thermal Index is calculated as the applied ultrasound power divided by the power that causes  $1^\circ\text{C}$  temperature rise in the tissue. Using the intensity and attenuation values in Table 2-3, and  $4.2 \text{ J/cm}^3/^\circ\text{C}$  for  $\gamma_v$ , the time duration for  $1^\circ\text{C}$  temperature rise at the focus is 93 ms for breast fat, 21 ms for fibroglandular tissue, and 40 ms for tumor. The ultrasound wave shouldn't be applied continuously more than a few cycles of the modulating wave in order not to exceed  $1^\circ\text{C}$ . If the transducer is directly placed on the tissue, heating at the skin by ultrasound must also be considered along with microwave heating. Assuming uniform illumination, the  $I_{\text{SPPA}}$  at the transducer aperture is  $0.17 \text{ W/cm}^2$  for the sample problem given in Section 2.7. Duration for  $1^\circ\text{C}$  temperature rise is calculated as 1.7 s at the skin (assuming  $1.84 \text{ dB/cm/MHz}$  attenuation [80]). Some of the input power applied to the transducer will also be converted to heat. Therefore, the efficiency of the transducer should also be taken into account while considering safety issues.

### ***Mechanical Index***

Main concerns about the mechanical effects of radiation force of ultrasound are cavitation and acoustic streaming. When the acoustic pressure passes a cavity like a gas bubble, it expands and contracts. If pressure is high enough, the gas bubble collapses, which in turn produce very high temperatures and pressures in a very short time. This is called cavitation. It causes the production of free radicals and liquid micro jets which can damage the cells. Acoustic streaming can occur in liquid parts of the body, which may cause thrombosis if the streaming is near a solid part.

A quantity called mechanical index is used for calculating the safety of an ultrasound system in terms of mechanical effects. It is given by [81]:

$$MI = \frac{p_-}{\sqrt{f}} \quad (2-46)$$

where  $p_-$  is the peak negative pressure of the ultrasound beam in Mega Pascal's and  $f$  is the frequency of the ultrasound beam in MHz's.

The FDA limit for MI is 1.9 [82]. The peak negative pressure is calculated to be 2.4 MPa for the ultrasound intensity given in Section 2.7. The MI due to this pressure is 1.32 which is below the FDA limit.

#### **2.8.8. Measurement Duration**

The Doppler component of the scattered signal is very low compared to the main component. Therefore, measurement duration should be long enough at each voxel to get a reliable signal level at the receiver. However, there are some limiting factors on the measurement time, namely, safety issues, shear wave disturbance and total imaging time. It was calculated in Section 2.8.7 that only 21 ms is enough to increase the temperature of the fibro-glandular tissue 1°C, which is shorter than three cycle duration for 125 Hz vibration. In order to avoid shear wave disturbance, it is also better take just a few cycles of the vibration. Therefore, a pulsed waveform is necessary for the ultrasound excitation. The received signals at each pulse can be integrated to improve the SNR at each point. It is not trivial to determine the number and duration required pulses without experimental analyses. However, if 10 pulses with 10 ms duration are used and 50 % duty cycle is employed to avoid heating and the effect of shear waves, for a dual vibration frequency system; 400 ms duration is necessary for each point. In order to scan a region of 10 cm x 10 cm with 2 mm steps, 16.7 minutes are necessary. As an implementation alternative, aprior microwave imaging can be applied to detect the high-reflectivity regions inside the tissue for which the presence of malignancy is suspected. The presented method can be employed for these suspicious regions to detect the presence of malignancy.

## 2.9. Conclusions and Discussion

In this chapter, a novel hybrid acoustic-microwave imaging method for breast tumor detection is introduced. It is investigated semi-analytically using two-layer breast model. Focused ultrasound radiation force is used to generate local vibrations in the tissue. Tumor is assumed to be spherical and electrically small (radius  $\ll \lambda$ ). The vibration of the local region induces a Doppler shift in the received signal, which is known to be the harmonic motion frequency of the vibrating region. The received signal level at the Doppler frequency caused by harmonic displacement is analyzed for various microwave operating frequencies and probe alignments. This work is an initial analysis about the method, and the problem is complex involving multiple disciplines. Therefore, some assumptions are made to simplify the analysis: 1) The breast tissue is assumed to be homogeneous, semi-infinite and bi-layered, 2) waveguide aperture is in an infinite ground plane, 3) the dielectric variation of the tissue due to motion and the effect of shear waves are not taken into account, 4) the tumor is completely inside the vibrating region, 5) the displacement of tumor is  $2.5 \mu\text{m}$ .

In mechanical simulations, the tissue is modeled as a linear elastic medium, and it is assumed that the Young's constant and Poisson's ratio are not functions of frequency and the applied force [83]. Also, the thermal effects on the peak value of the displacement are ignored. The radiation force is assumed to be solely due to attenuation, and the effect of ultrasound reflection at the tissue interfaces to the radiation force is not taken into account. As the acoustic impedance is similar in tumor and fibro-glandular tissues, the reflection from tumor/fibro glandular interfaces are very small. The reflections from fat/tumor and fat/fibro-glandular interfaces are stronger than the reflections from the tumor/fibro glandular interfaces. However, they are still weak ( $\sim 1\%$ ). This effect can increase the radiation force slightly, which is an advantage for the microwave detection.

Fibro-glandular tissue has lower elasticity modulus and higher attenuation than the tumor. In this aspect, the contrast due to vibration amplitude is high between fibro-glandular and malignant tissue, which is desirable for detecting tumors in fibro-glandular tissue. The images should be acquired for multiple harmonic motion frequencies in order to increase the sensitivity and discriminate the malign tissue from benign tissue.

The results show that, in terms of the received signal amplitude at the Doppler frequency, the microwave frequency of operation should be 2-2.5 GHz for relatively dense breast tissues (medium to low adipose content mostly), whereas 5 GHz is suitable for mostly fatty tissue.

Regarding the alignment of the antennas, the main advantages of the E-plane alignment are sensitivity in shallow regions and compactness. However, the directly coupled signal to the scattered signal ratio is higher for the E-plane alignment case compared to the H-plane alignment case.

The directly coupled signal is a limiting factor for choosing the alignment of the antennas, and also for the microwave operation frequency since the Doppler signal frequency is very

close to the carrier frequency. It may be preferable to have an imaging system operating in multiple frequencies and to choose the frequency of operation for best SNR value.

For safety, ultrasound intensity and duty cycle should be considered along with the microwave exposure so that just enough displacement is given to the tissue locally without exceeding safety limits. This affects the speed of the data acquisition system and should be considered in further studies. The received signal drops about 6 dB when the displacement of the tumor is halved (2-42). In the presented results, 2.5  $\mu\text{m}$  was used for the vibration amplitude. However, it is found to be lower for vibration frequencies higher than 125 Hz. In safety analyses, it was shown that the values used in the acoustic simulations are near the safety limits. Nevertheless, the microwave output power (which is 1 Watt in the analyses) can be increased to improve the performance for higher vibration frequencies. The SAR analyses show that the most of the microwave power is absorbed by the tissue near the surface. Using surface cooling techniques, more output power can be used for better detection performance. Also, lower vibration frequencies can be used to increase the displacement amplitude.

Shear wave disturbance in the late time may disturb the received signal by creating clutter. Therefore, the data should be taken at the early time. A pulsed ultrasound wave packet is recommended, which is also necessary for safety of the patient. The number of pulses used at each point of scan should be optimized in order to obtain enough SNR in the minimum amount of time.

A typical value for the sensitivity of the receiver is calculated, and the results show that the proposed method may be used for breast tumor detection without exceeding safety limitations. Therefore, the method is rewarding for further numerical and experimental investigation.

## CHAPTER 3

### DEVELOPMENT OF NUMERICAL TOOLS FOR REALISTIC SIMULATIONS

#### 3.1. Introduction

Numerical methods are useful in analyzing complex engineering problems. Tissue is an inhomogeneous medium and numerical methods are required for realistic solutions. There are mainly three types of numerical methods which are widely used: Method of Moments (MoM), Finite Element Methods (FEM), Finite Difference Time Domain Methods (FDTD). In MoM, the solution is constructed using the known Green's function for a given problem. The problem region is divided into smaller parts and fields are solved using integral equation formulation for a given frequency [84]. In FEM, the problem region is divided into small elements, which are generally tetrahedrons or hexahedrons. The elements can be made conformal to curved surfaces. The solution is obtained solving Maxwell's Equations for all the elements simultaneously for a given frequency [85]. Thus, the Green's function is not used in this case. In FDTD method [86], the problem region is divided into cubic (or rectangular hexahedral) elements. The Maxwell's Equations are discretized in time and space domain. The solution for the fields is iterated in time. The FDTD method is employed in this thesis for the realistic simulations because of the following reasons: 1) There is no need to calculate the Green's function; 2) it is easy to implement; 3) inhomogeneous media can be easily implemented into the simulations; 4) memory requirements are less demanding compared to FEM since there is no matrix inversion.

The physical problem in HMMDI method is complicated which is a combination of acoustic, mechanical and electromagnetic problems. The simulation methodology used in this thesis is given in Figure 3-1.

For acoustic simulations, HIFU simulator tool developed by U.S Food and Drug Administration (FDA) [67] is used. The ultrasound intensity distribution is used as an input to the mechanical simulator. The acoustic radiation force is calculated using (2-1). The intensity is assumed to be changing sinusoidally as if the transducer is driven with an amplitude modulated signal. A 3-D displacement distribution is obtained using the mechanical simulator. The displacement distribution is fed into the electromagnetic simulator as snapshots in time. The received signal at the fundamental and the Doppler frequencies are outputs of the electromagnetic simulator. Simplified tissue models are used for the initial simulations. Realistic tissue models derived from the MRI data by University of Wisconsin Computational Electromagnetics (UWCEM) group [89] is used for the realistic simulations. To simplify the problem, the effect of heating due to ultrasound and RF radiation is not taken into account.



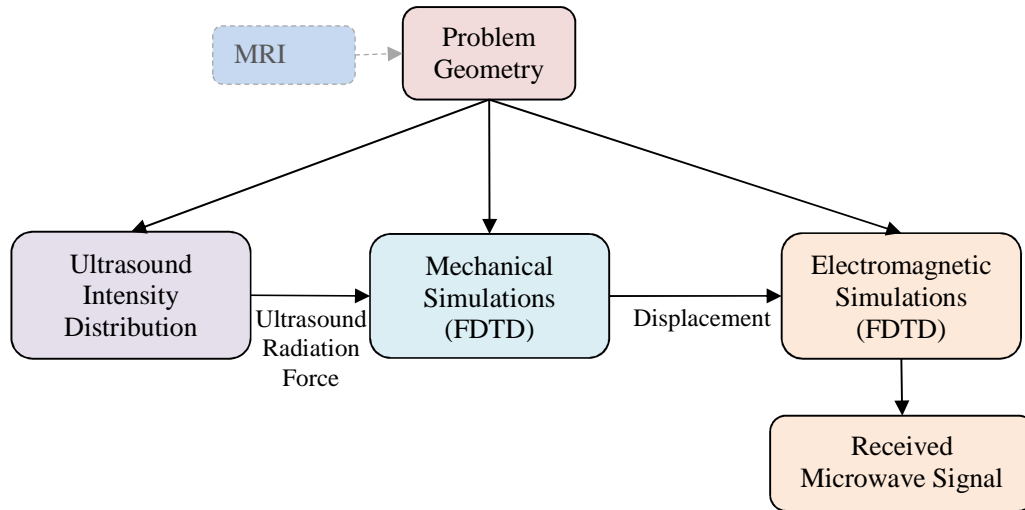


Figure 3-1: Forward Problem Simulation Methodology for HMMDI Method

The mechanical and electromagnetic simulators are developed in the scope of this thesis.

In the mechanical part of the problem, velocity stress-strain equations are solved with the FDTD method. Input is the mechanical body load of the acoustic radiation force. The resultant displacement distribution inside the tissue is the output of this solver.

In the electromagnetic part, snapshots of the displacement maps are used to predict the Doppler component of the received electromagnetic signal. A novel approach is used for the simulation of the scattered field from a vibrating region inside the tissue. Two consecutive simulations are run: one with the displacement, and one without displacement. Since the displacement values are much smaller than the wavelength and the FDTD grid size, a sub-cell approach [87] is used to introduce the effect of displacement. The resultant Doppler signal level is much lower than the direct coupled signal level. In order to resolve this small signal component, scattered fields are calculated using the Volume Equivalence Theorem.

This chapter is organized as follows: In the next section, the mechanical FDTD simulator is introduced. The results obtained from the simulator are compared with commercial multi-physics solver COMSOL Multi-physics for validation purposes. In the following section, electromagnetic FDTD simulator is described. The electromagnetic solver is validated by comparing its results with the results obtained using the semi-analytical solution.

### 3.2. Mechanical FDTD Solver for Displacement Analysis

Staggered-grid FDTD method has been formulated for seismic wave propagation in elastic media by Virieux [90], [91] and Levander [92] for 2-D, and by Randall [93], Yamogida and Etgen [94] for 3-D problems. A 3-D solver is implemented in this study. The equations of motion are solved together with stress-strain relationships in the simulations. The set of Equations are discretized in time and space and solved iterating in time. The equations of motion for velocity-stress relations are given by:

$$\frac{\partial v_x}{\partial t} = \frac{1}{\rho} \left( \frac{\partial \tau_{xx}}{\partial x} + \frac{\partial \tau_{xy}}{\partial y} + \frac{\partial \tau_{xz}}{\partial z} + f_x \right) \quad (3-1)$$

$$\frac{\partial v_y}{\partial t} = \frac{1}{\rho} \left( \frac{\partial \tau_{xy}}{\partial x} + \frac{\partial \tau_{yy}}{\partial y} + \frac{\partial \tau_{yz}}{\partial z} + f_y \right) \quad (3-2)$$

$$\frac{\partial v_z}{\partial t} = \frac{1}{\rho} \left( \frac{\partial \tau_{xz}}{\partial x} + \frac{\partial \tau_{yz}}{\partial y} + \frac{\partial \tau_{zz}}{\partial z} + f_z \right) \quad (3-3)$$

Where  $v_x, v_y, and v_z$  are the velocity components,  $\tau_{xx}, \tau_{yy}, \tau_{zz}, \tau_{xy}, \tau_{xz} and \tau_{yz}$  are the stress components,  $f_x, f_y, and f_z$  are the load components, and  $\rho$  is the density of the medium.

The stress-strain relationships in terms of velocity are given by [91]:

$$\frac{\partial \tau_{xx}}{\partial t} = (\lambda + 2\mu) \frac{\partial v_x}{\partial x} + \lambda \left( \frac{\partial v_y}{\partial y} + \frac{\partial v_z}{\partial z} \right) \quad (3-4)$$

$$\frac{\partial \tau_{yy}}{\partial t} = (\lambda + 2\mu) \frac{\partial v_y}{\partial y} + \lambda \left( \frac{\partial v_x}{\partial x} + \frac{\partial v_z}{\partial z} \right) \quad (3-5)$$

$$\frac{\partial \tau_{zz}}{\partial t} = (\lambda + 2\mu) \frac{\partial v_z}{\partial z} + \lambda \left( \frac{\partial v_x}{\partial x} + \frac{\partial v_y}{\partial y} \right) \quad (3-6)$$

$$\frac{\partial \tau_{xy}}{\partial t} = \mu \left( \frac{\partial v_x}{\partial y} + \frac{\partial v_y}{\partial x} \right) \quad (3-7)$$

$$\frac{\partial \tau_{xz}}{\partial t} = \mu \left( \frac{\partial v_x}{\partial z} + \frac{\partial v_z}{\partial x} \right) \quad (3-8)$$

$$\frac{\partial \tau_{yz}}{\partial t} = \mu \left( \frac{\partial v_y}{\partial z} + \frac{\partial v_z}{\partial y} \right) \quad (3-9)$$

where  $\lambda$  is the first Lamé coefficient, and  $\mu$  is the second Lamé coefficient. These constants define the elastic property of the medium.

The discrete form of the Equations can be written as:

$$\begin{aligned}
v_{x_{i+\frac{1}{2},j,k}}^{n+1/2} &= v_{x_{i+\frac{1}{2},j,k}}^{n-1/2} \\
&+ \frac{\Delta t}{2} \left( \frac{1}{\rho_{i+1,j,k}} + \frac{1}{\rho_{i,j,k}} \right) \left( \frac{\tau_{xx_{i+1,j,k}}^n - \tau_{xx_{i,j,k}}^n}{\Delta x} + \frac{\tau_{xy_{i+\frac{1}{2},j+1,k}}^n - \tau_{xy_{i+1/2,j,k}}^n}{\Delta y} \right. \\
&\left. + \frac{\tau_{xz_{i+\frac{1}{2},j,k+1}}^n - \tau_{xz_{i+1/2,j,k}}^n}{\Delta z} + f_x \right)
\end{aligned} \tag{3-10}$$

$$\begin{aligned}
v_{y_{i,j+1/2,k}}^{n+1/2} &= v_{y_{i,j+1/2,k}}^{n-1/2} \\
&+ \frac{\Delta t}{2} \left( \frac{1}{\rho_{i,j+1,k}} + \frac{1}{\rho_{i,j,k}} \right) \left( \frac{\tau_{xy_{i+1,j+1/2,k}}^n - \tau_{xy_{i,j+1/2,k}}^n}{\Delta x} + \frac{\tau_{yy_{i,j+1,k}}^n - \tau_{yy_{i,j,k}}^n}{\Delta y} \right. \\
&\left. + \frac{\tau_{yz_{i,j+1/2,k+1}}^n - \tau_{yz_{i,j+1/2,k}}^n}{\Delta z} + f_y \right)
\end{aligned} \tag{3-11}$$

$$\begin{aligned}
v_{z_{i,j,k+1/2}}^{n+1/2} &= v_{z_{i,j,k+1/2}}^{n-1/2} \\
&+ \frac{\Delta t}{2} \left( \frac{1}{\rho_{i,j,k+1}} + \frac{1}{\rho_{i,j,k}} \right) \left( \frac{\tau_{xz_{i+1,j,k+1/2}}^n - \tau_{xz_{i,j,k+1/2}}^n}{\Delta x} \right. \\
&\left. + \frac{\tau_{yz_{i,j+1,k+1/2}}^n - \tau_{yz_{i,j,k+1/2}}^n}{\Delta y} + \frac{\tau_{zz_{i,j,k+1}}^n - \tau_{zz_{i,j,k}}^n}{\Delta z} + f_z \right)
\end{aligned} \tag{3-12}$$

$$\begin{aligned}
\tau_{xx_{i,j,k}}^{n+1} &= \tau_{xx_{i,j,k}}^n \\
&+ \Delta t \left[ \left( \lambda_{i,j,k} + 2\mu_{i,j,k} \right) \frac{v_{x_{i+1/2,j,k}}^{n+1/2} - v_{x_{i-1/2,j,k}}^{n+1/2}}{\Delta x} \right. \\
&\left. + \lambda_{i,j,k} \left( \frac{v_{y_{i,j+1/2,k}}^{n+1/2} - v_{y_{i,j-1/2,k}}^{n+1/2}}{\Delta y} + \frac{v_{z_{i,j,k+1/2}}^{n+1/2} - v_{z_{i,j,k-1/2}}^{n+1/2}}{\Delta z} \right) \right]
\end{aligned} \tag{3-13}$$

$$\begin{aligned}
\tau_{yy}^{n+1} = \tau_{yy}^n & \\
& + \Delta t \left[ \left( \lambda_{i,j,k} + 2\mu_{i,j,k} \right) \frac{v_{y,i,j+1/2,k}^{n+1/2} - v_{y,i,j-1/2,k}^{n+1/2}}{\Delta y} \right. \\
& \left. + \lambda_{i,j,k} \left( \frac{v_{x,i+1/2,j,k}^{n+1/2} - v_{x,i-1/2,j,k}^{n+1/2}}{\Delta x} + \frac{v_{z,i,j,k+1/2}^{n+1/2} - v_{z,i,j,k-1/2}^{n+1/2}}{\Delta z} \right) \right]
\end{aligned} \tag{3-14}$$

$$\begin{aligned}
\tau_{zz}^{n+1} = \tau_{zz}^n & \\
& + \Delta t \left[ \left( \lambda_{i,j,k} + 2\mu_{i,j,k} \right) \frac{v_{z,i,j,k+1/2}^{n+1/2} - v_{z,i,j,k-1/2}^{n+1/2}}{\Delta z} \right. \\
& \left. + \lambda_{i,j,k} \left( \frac{v_{x,i+1/2,j,k}^{n+1/2} - v_{x,i-1/2,j,k}^{n+1/2}}{\Delta x} + \frac{v_{y,i,j+1/2,k}^{n+1/2} - v_{y,i,j-1/2,k}^{n+1/2}}{\Delta y} \right) \right]
\end{aligned} \tag{3-15}$$

$$\begin{aligned}
\tau_{xy}^{n+1} = \tau_{xy}^n & \\
& + \Delta t \left\{ \left[ \frac{1}{4} \left( \frac{1}{\mu_{i,j,k}} + \frac{1}{\mu_{i+1,j,k}} + \frac{1}{\mu_{i,j+1,k}} \right. \right. \right. \\
& \left. \left. \left. + \frac{1}{\mu_{i+1,j+1,k}} \right) \right]^{-1} \left[ \frac{v_{x,i+1/2,j+1,k}^{n+1/2} - v_{x,i+1/2,j,k}^{n+1/2}}{\Delta y} + \frac{v_{y,i+1,j+1/2,k}^{n+1/2} - v_{y,i,j+1/2,k}^{n+1/2}}{\Delta x} \right] \right\}
\end{aligned} \tag{3-16}$$

$$\begin{aligned}
\tau_{xz}^{n+1} = \tau_{xz}^n & \\
& + \Delta t \left\{ \left[ \frac{1}{4} \left( \frac{1}{\mu_{i,j,k}} + \frac{1}{\mu_{i+1,j,k}} + \frac{1}{\mu_{i,j,k+1}} \right. \right. \right. \\
& \left. \left. \left. + \frac{1}{\mu_{i+1,j,k+1}} \right) \right]^{-1} \left[ \frac{v_{x,i+1/2,j,k+1}^{n+1/2} - v_{x,i+1/2,j,k}^{n+1/2}}{\Delta z} + \frac{v_{z,i+1,j,k+1/2}^{n+1/2} - v_{z,i,j,k+1/2}^{n+1/2}}{\Delta x} \right] \right\}
\end{aligned} \tag{3-17}$$

$$\begin{aligned}
\tau_{yz}^{n+1}{}_{i,j+1/2,k+1/2} &= \tau_{yz}^n{}_{i,j+1/2,k+1/2} \\
&+ \Delta t \left\{ \left[ \frac{1}{4} \left( \frac{1}{\mu_{i,j,k}} + \frac{1}{\mu_{i,j+1,k}} + \frac{1}{\mu_{i,j,k+1}} \right. \right. \right. \\
&\left. \left. \left. + \frac{1}{\mu_{i,j+1,k+1}} \right) \right]^{-1} \left[ \frac{v_{y_{i,j+1/2,k+1}}^{n+\frac{1}{2}} - v_{y_{i,j+1/2,k}}^{n+\frac{1}{2}}}{\Delta z} + \frac{v_{z_{i,j+1,k+1/2}}^{n+\frac{1}{2}} - v_{z_{i,j,k+1/2}}^{n+\frac{1}{2}}}{\Delta y} \right] \right\}
\end{aligned} \tag{3-18}$$

The unit cell for the grid, adopted from [95] is shown in Figure 3-2. The FDTD code is implemented in C++ and validated with the results obtained by the commercial multi-physics software COMSOL 4.0. The parameters used in the mechanical COMSOL simulations are given in Table 3-1. 2-D axially symmetric geometry is used in the COMSOL simulations.

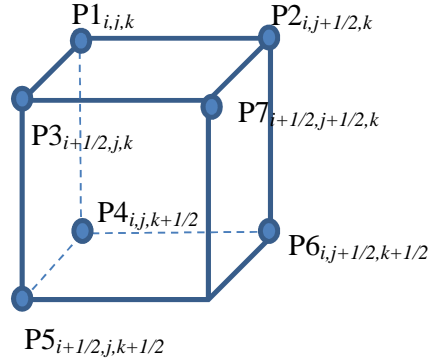


Figure 3-2: Positions of the material constants, velocity and strain fields in the unit cell. The components at the points P1 to P7 are; P1:  $\rho, \lambda, \mu, \tau_{xx}, \tau_{yy}, \tau_{zz}$ , P2:  $v_x$ , P3:  $v_y$ , P4:  $v_z$ , P5:  $\tau_{yz}$ , P6:  $\tau_{xz}$  and P7:  $\tau_{xy}$ .

For validation analyses, the ultrasound transducer is assumed to emit focused Gaussian beam with the intensity profile [88]:

$$I = \frac{I_0 A_1}{B_g} e^{-2A_1 \left(\frac{r}{a}\right)^2} e^{-2\alpha z} \tag{3-19}$$

where

$$A_1(z) = \frac{B_g}{\frac{B_g^2 z^2}{\left(\frac{k_a a^2}{2}\right)^2} + \left(1 - \frac{z}{z_f}\right)^2} \tag{3-20}$$

$B_g$  and  $z_f$  are the Gaussian coefficient of the transducer and the focal length of the transducer, respectively.  $k_a$  is the acoustic wavenumber,  $a$  is the transducer radius,  $\alpha$  is the

acoustic attenuation constant of the tissue. The radiation force due to this intensity profile, as given in (3-19) is applied as input to the numerical simulator. The force is applied as a volume load to the tissue sinusoidally, for frequencies 100 Hz, 250 Hz, 500 Hz and 1000 Hz. In all simulations, the peak force at the focus is  $0.41\text{N/cm}^3$ , and the peak value of intensity of the beam is  $18.8\text{ W/cm}^2$ . It is assumed that the intensity profile given in (3-19) is not affected by the presence of the skin layer and the inhomogeneity of the breast tissue.

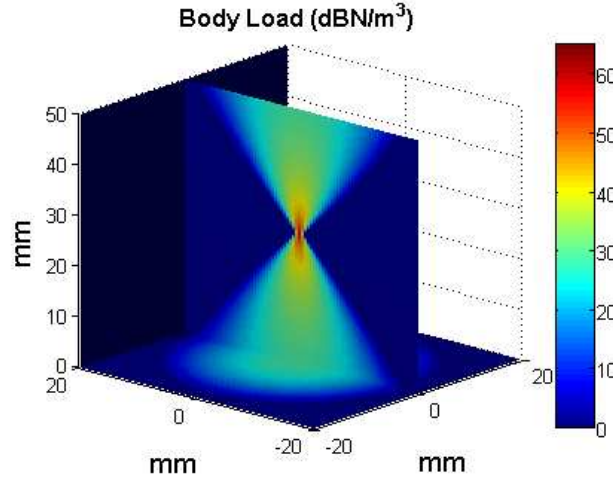


Figure 3-3: Mechanical volume load applied to the tissue.

Table 3-1: Parameters Used In Mechanical Simulations

<b>Frequency</b>	3 MHz	
<b>Gaussian coefficient of the transducer <math>B_g</math></b>	1	
<b>Focal length of the transducer <math>z_f</math></b>	25 mm	
<b>Radius of the transducer <math>a</math></b>	10 mm	
<b>Young's Constant (E)</b>	Breast tissue	5 kPa
	Tumor	20 kPa
<b>Poisson's ratio</b>	All tissues	0.495
<b>Ultrasonic absorption const.(dB/cm/MHz)</b>	All tissues	0.75
<b>Intensity of the beam at focus</b>	$18.8\text{ W/cm}^2$	
<b>Focal Width (FWHM) of the transducer</b>	0.48 mm	
<b>Focal Depth (FWHM) of the transducer</b>	2.06 mm	
<b>Number of elements in the Finite Element model</b>	4308	
<b>Maximum element size in the Finite Element model</b>	0.8 mm	

For the FDTD simulations, the body load applied to the tissue in  $\hat{z}$ -direction is given in Figure 3-3 at  $y=0$  plane. In order to visualize better, load is given in logarithmic scale. The boundaries of the simulation domain are zero-stress free-surface boundary. The displacement values at the focal point obtained from FDTD and COMSOL are plotted in Figure 3-4, for frequencies ranging from 100Hz to 1000Hz. The results obtained by COMSOL are interpolated from the values at 100 Hz, 250 Hz, 500 Hz and 1000Hz. FDTD simulations are run in 100 Hz steps ranging from 100 Hz to 1000Hz. The results in two cases show very good agreement. The average difference between the FDTD and COMSOL results are 1.27  $\mu\text{m}$  for  $E=5\text{kPa}$  case and 1.17  $\mu\text{m}$  for  $E=20\text{kPa}$  in 5kPa case.

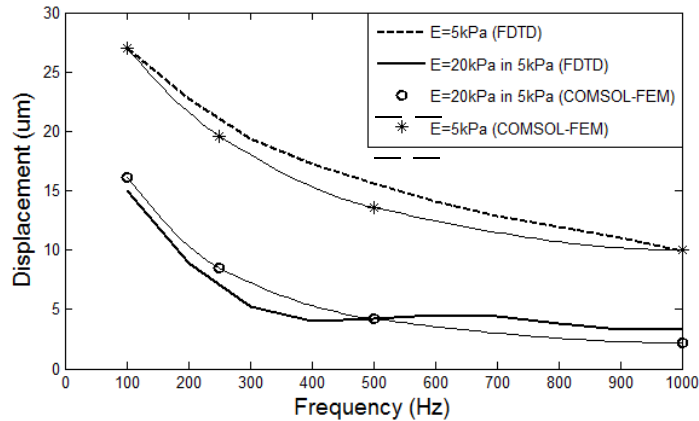


Figure 3-4: The displacement values at the focal point obtained from FDTD and COMSOL simulation results.

### 3.3. Electromagnetic FDTD Solver

FDTD method is a very common tool for electromagnetic simulations. The Maxwell's Equations in differential form are discretized in time and space. Magnetic and electric fields are solved in a half time step difference using a leap-frog scheme. A staggered grid is used with cubic cells. FDTD is suitable for biomedical applications since tissue is an inhomogeneous type of media that can be handled easily by controlling the simulation domain media parameters.

An electromagnetic FDTD code is implemented in MATLAB with Convolutional Perfectly Matched Layer (CPML) boundaries [96] terminating the solution region. Waveguide terminations are necessary in the simulations since the microwave signal is transmitted and received with open-ended waveguide type antennas. There are a number of ways for waveguide port implementation. The easiest one is placing the approximate transverse field distribution of the propagating mode as a hard source [97]. Since the impedance of the hard source is zero, the field reflected back to the source will be reflected into computation

domain. This brings a limit for the duration of the source. Absorbing boundary conditions may be used in terminations. At the port, backward and forward travelling waves should be separated in this approach [98]. Another way of implementing a reflection free port is terminating it with the characteristic impedance of the waveguide [99]. This method is preferred for waveguide port termination in this study since it is simple and effective. The waveguide is excited with a monochrome signal, and the characteristic impedance at the excitation frequency is found analytically.

### 3.3.1. Scattered Field from a Vibrating Tumor Inside the Tissue in 3-D FDTD

In the HMMDI method, the effect of vibration inside the tissue should be modeled in the simulation. Time-varying sheet surface impedance boundary conditions are formulated for the scattering due to time varying boundaries of the conducting [100], and dielectric cylinders [101]. These types of boundary conditions are implemented for 2-D problems in an FDTD scheme [102]. In this approach, two consecutive electromagnetic simulations are run. In the first simulations, the target is stationary. The fields from this simulation are stored and are used to find the currents at the moving boundaries of the target. In the second simulation, the only source is the boundary current sources which accounts for the motion of the boundary. It is necessary to use second order boundary conditions for arbitrary boundary perturbations. This method requires the calculation of the tangential derivatives of the fields, and careful choice of the current locations in the grid. Finding analytical expressions for the boundary currents is not straightforward [103] for a 3-D FDTD implementation of a vibrating scatterer problem. In this thesis, a different approach is proposed. The volume currents - directly calculated from the field components - are employed, and the volume equivalent problem is solved. The original and the equivalent FDTD models of a sample problem are given in Figure 3-5.

The procedure is as follows: A simulation is run, for the scatterer object at its original position. The transmitting (TX) antenna is active, and the electric fields inside the object are stored for each time step. A second simulation is run, for which the object is replaced by its volume equivalent electric current ( $\vec{J}_{eq}$ ) distribution, using the Volume Equivalence Principle. TX antenna is passive in this case.

For the second simulation, the volume equivalent currents can be written as:

$$\vec{J}_{eq} = (\epsilon_{obj} - \epsilon_b) \frac{d\vec{E}_{obj}}{dt} + (\sigma_{obj} - \sigma_b) \vec{E}_{obj} \quad (3-21)$$

Discretizing the current for FDTD simulation, we get:



$$\vec{J}_{eq_{i,j,k}}^n = (\varepsilon_{obj} - \varepsilon_b) \frac{\vec{E}_{obj_{i,j,k}}^{n+1} - \vec{E}_{obj_{i,j,k}}^n}{\Delta t} + (\sigma_{obj} - \sigma_b) \frac{\vec{E}_{obj_{i,j,k}}^{n+1} + \vec{E}_{obj_{i,j,k}}^n}{2} \quad (3-22)$$

where  $\varepsilon_{obj}$ ,  $\sigma_{obj}$  and  $\varepsilon_b$ ,  $\sigma_b$  are the permittivity and the conductivity values of the tumor and the background tissue, respectively.  $\vec{E}_{obj}$  is the stored electric field components inside the scatterer volume in the first simulation. Magnetic current source is not present since the permeability is constant throughout the tissue. The frequency domain signal obtained in the second simulation at the RX antenna aperture is divided by the signal at the TX antenna aperture in the first simulation. By this way, the amplitude ( $A_1$ ) and the phase ( $\Phi_1$ ) of the scattered field component of the  $S_{21}$  parameter is obtained for the undisplaced tumor. The same procedure is repeated for the scatterer displaced to maximum extent due to vibration, and the amplitude ( $A_2$ ) and the phase ( $\Phi_2$ ) of the scattered field component of the  $S_{21}$  parameter are obtained. The procedure is shown in Figure 3-6.

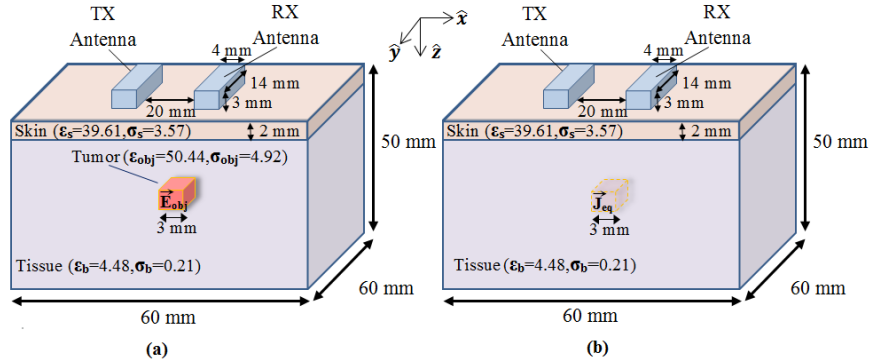


Figure 3-5: Original (on the left) and the volume equivalent (on the right) FDTD simulation geometries. Breast tissue is modeled with two layers: skin and normal (high adipose content) tissue. Antennas are placed on top of the skin layer. A cubic tumor is present in the original problem. In the reciprocal problem it is replaced by volume equivalent current source.

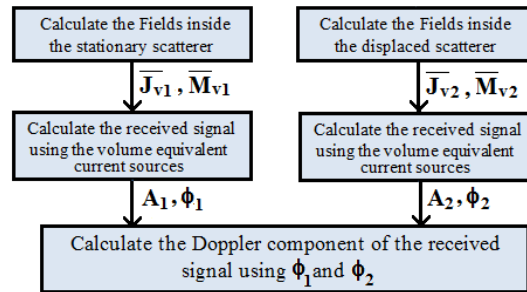


Figure 3-6: Procedure of the method for calculating the Doppler component of the scattered field

### 3.3.1.1. Calculation of the Doppler Component

The vibration introduces phase and amplitude modulation on the scattered signal. Maximum amplitude and phase deviations on the received signal are calculated as  $\Delta A = A_2 - A_1$  and  $\Delta\Phi = \Phi_2 - \Phi_1$ . Neglecting the effect of amplitude modulation, which can be shown to be very small compared to the effect of phase modulation, the received signal due to a vibrating scatterer is of the form:

$$S_{RX}(t) = A_1 \cos\left(\omega_m t + \frac{4\pi R}{\lambda} + \Delta\Phi \sin(\Delta\omega t + \varphi) + \varnothing\right) \quad (3-23)$$

where  $R$  is the distance from antennas to locally vibrating tumor,  $\omega_m$  is the operating frequency of the microwave transmitter,  $\Delta\omega$  is the vibration frequency, and  $\lambda$  is the wavelength inside the tissue. It is assumed that the vibrating region is on the mid-plane between the TX and the RX antennas. Since  $\Delta\Phi$  is much less than unity, (3-23) can be written as:

$$S_{RX}(t) = A_1 \left\{ \cos\left(\omega_m t + \frac{4\pi R}{\lambda} + \varnothing\right) \pm \frac{\Delta\Phi}{2} \cos(\omega_m t \mp \Delta\omega t + \varphi) \right\} \quad (3-24)$$

The signal magnitude at the Doppler frequency ( $\Delta\omega$ ) is  $\Delta\Phi/2$  times smaller than the main scattered signal level  $A_1$ .  $\Delta\omega$  is determined by the modulation frequency of the acoustic signal, which is practically tens to thousands of Hertz's. This component can be extracted using low phase noise transmitters and highly sensitive receivers.

### 3.3.1.2. FDTD Sub-cell Grid

When the tumor displaces, its boundary moves inside the adjacent cell (Figure 3-7). Practical displacement values are on the order of microns. In order to simulate small displacements in the geometry, a sub-cell method, which is originally developed for thin material sheets [87] is used. In this method, the cells including the thin sheet are specialized. The FDTD update equations are altered for these special cells. In the vibrating scatterer case, the cells surrounding the scatterer are "special" because of the displacement. The mechanical force, which acts on a very small (millimetric) volume, is assumed to be given by a focused ultrasound transducer radiating in the  $\hat{z}$ -direction. Since the displacement of the tumor is mainly in the direction of the force, the thin sheets are placed parallel to  $xy$ -plane.

In the special cells,  $E_z$  field is split into  $E_z$  and  $E_{zs}$  components since  $E_z$  field component is normal to the boundary and not continuous. The tangential field components at the boundaries ( $E_x$ ,  $E_y$ ,  $H_x$ ,  $H_y$ ) are continuous. Therefore, these field components are not split.  $H_z$  field component is also continuous since the permeability is same everywhere inside the tissue.

For the update Equations of the E-field components, integral form of Maxwell's first Equation (Ampere's Law) is used:

$$\oint \vec{H} \cdot d\vec{l} = \iint \frac{d\vec{D}}{dt} \cdot d\vec{S} \quad (3-25)$$

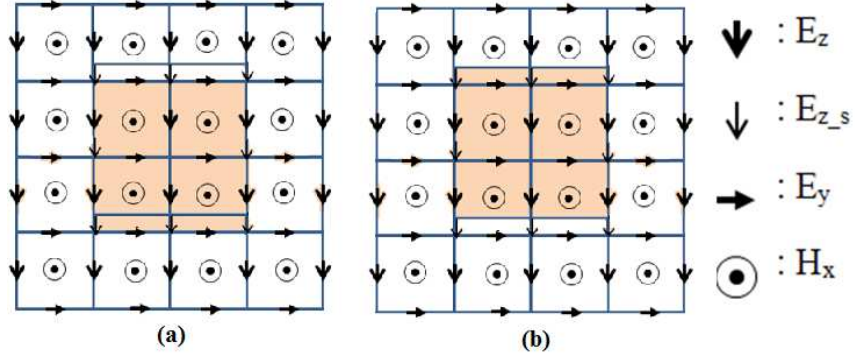


Figure 3-7: FDTD grid showing field components  $E_z$ ,  $E_y$  and  $H_x$  for the displaced scatterer case on the y-z plane cut of the 3D geometry.  $E_z$ ,  $H_y$  and  $H_z$  field components are not shown for simplicity.

$E_z$  component:

Writing (3-25) for a generic  $Ez_{i,j,k}^{n+1}$  component,

$$\begin{aligned} Hx_{i,j+1/2,k}^{n+1/2} \Delta x - Hx_{i,j-1/2,k}^{n+1/2} \Delta x + Hy_{i+1/2,j,k}^{n+1/2} \Delta y - Hy_{i-1/2,j,k}^{n+1/2} \Delta y \\ = \epsilon_{i,j,k} \frac{Ez_{i,j,k}^{n+1} - Ez_{i,j,k}^n}{\Delta t} + \sigma_{i,j,k} \frac{Ez_{i,j,k}^{n+1} + Ez_{i,j,k}^n}{2} \end{aligned} \quad (3-26)$$

Media parameters and the H-field components are not affected by the displacement. Therefore update Equation is not changed for the  $E_z$  component.

$E_{z_s}$  component:

Writing (3-25) for a generic  $Ez_{i,j,k}^{n+1}$  component,

$$\begin{aligned}
& Hx_{i,j+1/2,k}^{n+1/2} \Delta x - Hx_{i,j-\frac{1}{2},k}^{n+\frac{1}{2}} \Delta x + Hy_{i+\frac{1}{2},j,k}^{n+\frac{1}{2}} \Delta y - Hy_{i-\frac{1}{2},j,k}^{n+1/2} \Delta y \\
& = \varepsilon_{i,j,k+1} \frac{Ez_{-S_{i,j,k}}^{n+1} - Ez_{-S_{i,j,k}}^n}{\Delta t} + \sigma_{i,j,k+1} \frac{Ez_{-S_{i,j,k}}^{n+1} + Ez_{-S_{i,j,k}}^n}{2}
\end{aligned} \tag{3-27}$$

Media parameters are changed because of the displacement. Since the displacement is in the  $-\hat{z}$  direction, the parameters should be replaced with the next neighboring cell parameters in the  $+\hat{z}$  direction.

H-field components are not changed since they are tangential to the boundary. These components can be taken as same as in  $E_z$  update equation for the greater cell.

*E<sub>y</sub> component:*

Writing (3-25) for a generic  $Ey_{i,j,k}^{n+1}$  component,

$$\begin{aligned}
& Hx_{i,j,k+1/2}^{n+1/2} \Delta x - Hx_{i,j,k-\frac{1}{2}}^{n+\frac{1}{2}} \Delta x + Hz_{i+\frac{1}{2},j,k}^{n+\frac{1}{2}} \Delta z - Hz_{i-1/2,j,k}^{n+1/2} \Delta z \\
& = \frac{(\Delta z - d)\varepsilon_{i,j,k} + d \varepsilon_{i,j,k+1}}{\Delta z} \frac{Ey_{i,j,k}^{n+1} - Ey_{i,j,k}^n}{\Delta t} \\
& + \frac{(\Delta z - d)\sigma_{i,j,k} + d \sigma_{i,j,k}}{\Delta z} \frac{Ey_{i,j,k}^{n+1} + Ey_{i,j,k}^n}{2}
\end{aligned} \tag{3-28}$$

where,  $d$  is the displacement value for the particular cell.

Average media parameters should be used since the media inside the area bounded by the Ampere's law contour includes both background and the object.

*E<sub>x</sub> component:*

Writing (3-25) for a generic  $Ex_{i,j,k}^{n+1}$  component:

$$\begin{aligned}
& Hy_{i,j,k+1/2}^{n+1/2} \Delta y - Hy_{i,j,k-\frac{1}{2}}^{n+\frac{1}{2}} \Delta y + Hz_{i,j+\frac{1}{2},k}^{n+\frac{1}{2}} \Delta z - Hz_{i,j-1/2,k}^{n+1/2} \Delta z \\
& = \frac{(\Delta z - d)\varepsilon_{i,j,k} + d \varepsilon_{i,j,k+1}}{\Delta z} \frac{Ex_{i,j,k}^{n+1} - Ex_{i,j,k}^n}{\Delta t} \\
& + \frac{(\Delta z - d)\sigma_{i,j,k} + d \sigma_{i,j,k}}{\Delta z} \frac{Ex_{i,j,k}^{n+1} + Ex_{i,j,k}^n}{2}
\end{aligned} \tag{3-29}$$

where  $d$  is the displacement value for the particular cell.

Average media parameters should also be used in this case, since the media inside the area bounded by the Ampere's law contour includes both background and the object.

For the update Equations of the H-field components, integral form of Maxwell's second Equation (Faraday's Law) is used:

$$\oint \vec{E} \cdot d\vec{l} = \iint \frac{d\vec{B}}{dt} \cdot d\vec{S} \quad (3-30)$$

*H<sub>z</sub> component:*

Writing (3-30) for a generic  $H_{i,j,k}^{n+1/2}$  component,

$$\begin{aligned} & Ex_{i,j+1/2,k}^n \Delta x - Ex_{i,j-1/2,k}^n \Delta x + Ey_{i+1/2,j,k}^n \Delta y - Ey_{i-1/2,j,k}^n \Delta y \\ & = \mu_0 \frac{Hz_{i,j,k}^{n+1/2} - Hz_{i,j,k}^{n-1/2}}{\Delta t} \end{aligned} \quad (3-31)$$

Permeability and the E-field components are not affected by the displacement. Therefore, update equation is not changed for the H<sub>z</sub> component.

*H<sub>y</sub> component:*

Writing (3-30) for a generic  $H_{i,j,k}^{n+1/2}$  component,

$$\begin{aligned} & Ex_{i,j,k+1/2}^n \Delta x - Ex_{i,j,k-1/2}^n \Delta x + Ez_{i+1/2,j,k}^n (\Delta z - d) + Ez_{s_{i+1/2,j,k}}^n(d) - Ez_{i-1/2,j,k}^n (\Delta z \\ & - d) - Ez_{s_{i-1/2,j,k}}^n(d) = \mu_0 \frac{Hy_{i,j,k}^{n+1/2} - Hy_{i,j,k}^{n-1/2}}{\Delta t} \end{aligned} \quad (3-32)$$

where  $d$  is the displacement value for the particular cell.

*H<sub>x</sub> component:*

Writing (3-30) for a generic  $H_{i,j,k}^{n+1/2}$  component,

$$\begin{aligned}
& Ey_{i,j,k+1/2}^n \Delta y - Ey_{i,j,k-1/2}^n \Delta y + Ez_{i,j+1/2,k}^n (\Delta z - d) + Ez_{s_{i,j+1/2,k}}^n (d) \\
& - Ez_{i,j-1/2,k}^n (\Delta z - d) - Ez_{-s_{i,j-1/2,k}}^n (d) = \mu_0 \frac{Hx_{i,j,k}^{n+1/2} - Hx_{i,j,k}^{n-1/2}}{\Delta t}
\end{aligned} \tag{3-33}$$

where  $d$  is the displacement value for the particular cell.

In realistic simulations, scatterers with arbitrary geometries along with arbitrary tumor shapes may be present. Therefore, the specialized cells are generalized to all cells and the Equations (3-26) to (3-29) and (3-31) to (3-33) are used for the whole volume.

In the thin sheet method, the location of the sheet in the cell is ambiguous. In the vibrating tumor problem,  $E_z$  field component is continuous along the thin sheet and the adjacent cell having the same material properties as that of the thin sheet. Assuming that the displacement values are very small compared to the cell size,  $E_{zs}$  field components are not used for generating the current source in (3-21). By this way, the location of the thin sheet is implicitly made adjacent to the neighboring cell. This assumption and its limitations are investigated in the next subsection. It is important to note that in order to have high accuracy in the simulations, the same grid and special cells with the same displacement values are used for the displaced and the undisplaced scatterer simulations. The only difference is in the media parameter values as seen in Figure 3-7. The phase relation between the two simulations is not conserved when the sub-cell grid implementation is changed for the displaced and undisplaced cases.

### 3.3.2. Validation of the FDTD code

In order to check the validity of the sub-cell approach, a simple waveguide discontinuity problem is solved. A dielectric filled waveguide having a first section with  $\epsilon_{r1}=20$  and a second section with  $\epsilon_{r2}=40$  is excited with 10 GHz monochrome signal from Port 1 (Figure 3-8). Generalized-scattering-matrix model given in [99] is used for terminating and exciting the waveguides. Simulation parameters are: Discretization in space ( $\Delta_{x,y,z}$ )= 1 mm, discretization in time ( $\Delta_t$ )= 1.11 picoseconds, no. of iterations = 3600 and mesh size = 2240. The length of the  $\epsilon_{r2}$  section is increased in very small amounts ( $d_{\text{sheet}}$ ), without changing the total waveguide length. The change in  $S_{11}$  parameter phase is calculated and compared with the analytical value calculated using  $4\pi d_{\text{sheet}}/\lambda_{g1}$ , where  $\lambda_{g1}$  is the guided wavelength in the low dielectric section. The difference between the two solutions was found to be smaller than 6% for small displacements below  $0.08 \times$  cell sizes. As the displacement increases, error increases as seen on Figure 3-8 since the current density inside the sheet is not taken into account. In the vibrating tumor problem, the practical values for displacement are below tens of microns. Therefore, the method is accurate enough to be used for numerical simulations.

The proposed method is validated on a sample problem by comparing the results with the results of a semi-analytical solution. The simulation geometry and the electrical parameters

are shown in Figure 3-5. Water-filled ( $\epsilon_{r\_water} = 77.15$ ,  $\sigma_{\_water} = 4.41$  S/m) open ended waveguides are used as TX and RX antennas. Geometry is terminated with 10 cells of Perfectly Matched Layers in all directions. TX antenna is excited (in  $TE_{10}$  mode) with a monochrome signal at 5 GHz frequency. The tumor is assumed to be vibrating in the  $\hat{z}$ -direction (max. displacement =  $10\mu\text{m}$ ). Simulation parameters are:  $\Delta_{x,y,z} = 1$  mm,  $\Delta_t = 1.11$  picoseconds, no. of iterations = 3600, and mesh size = 512K. Spectral approach [60] with two layer semi-infinite breast model is used in the semi-analytical calculations. This method was presented in Chapter 2. In this case, the tumor is modeled as a polarization current density [66], which is equivalent to a sphere having the same volume with the cubic tumor inclusion in the FDTD simulations. The received signal due to this current source is calculated using the Reciprocity Theorem. The semi-analytical method was validated using CST Microwave Studio. Figure 3-9 shows the main scattered signal level and the Doppler component as a function of tumor depth for 1Watt TX output power. The magnitudes of reflection ( $S_{11}$ ) and direct coupling ( $S_{21}$ ) parameters of the antennas de-embedded to their aperture plane are -10.7 dB and -28 dB, respectively.

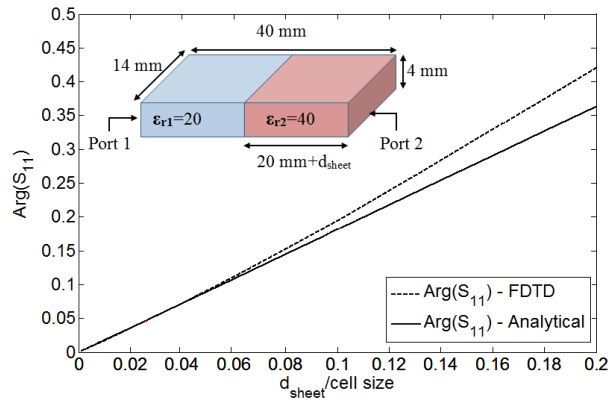


Figure 3-8:  $S_{11}$  phase in radians for the waveguide discontinuity problem as a function of normalized sheet thickness.

The results obtained with the two methods have a very good agreement, especially below a certain tumor depth (15 mm). The disagreement in the shallow region can be explained as follows: In semi-analytical calculations, the scattering response of a sphere is used, and the tumor inclusion is modeled as a point source. However, the tumor is modeled as a cube in the FDTD grid. In practice, the Doppler component is mostly affected by the movement of the surface of the tumor inclusion, which is the case in the FDTD simulations. At the far zone of the antennas, the phase gradients of the fields are nearly constant, and the point source model is a good approximation.

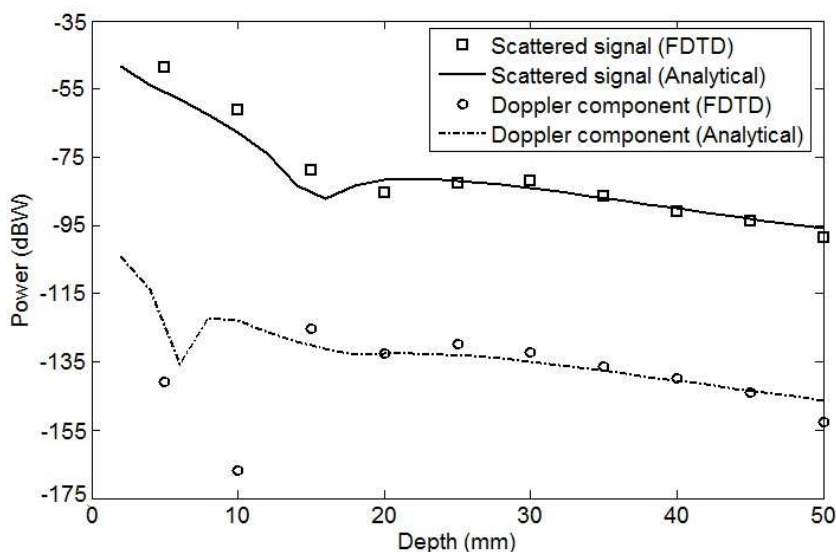


Figure 3-9: Comparison of the results obtained by numerical (FDTD) and semi-analytical solution.

More realistic FDTD simulations of heterogeneous tissues that also include medium and low adipose content tissues are possible with the proposed approach. Analysis of the same problem using a brute force method requires high discretization resolution ( $<\lambda/1000$ ) with demanding memory resources, and smaller time steps. The usage of time-varying SIBC's requires high order spatial derivatives of the field components, and high amount of effort is needed to formulate a 3-D FDTD implementation. The proposed method only requires an extra field component in the regular FDTD gridding scheme. Thus, the method is efficient in terms of memory requirements, computation time and implementation effort. Accuracy of the method is high enough to resolve the Doppler component of the field which is much smaller than the main scattered field component ( $<-50$  dB). The special cells can be generalized to the whole geometry, and the displacement maps from mechanical simulation tools can be readily implemented without changing the formulation. The recommended limit for maximum displacement is one tenth of the cell size, to keep the phase error smaller than 10%. The limitation of the method is that only unidirectional deformation of the scatterer can be simulated. Nevertheless, the deformation in the directions other than the direction of motion can be assumed to be small in the vibrating tumor problem. The validity of this assumption must be checked with mechanical simulations before adopting the proposed method for electromagnetic simulations.

### 3.4. Conclusions

Analysis of the physical problem for the proposed HMMDI method is complex since it is a hybrid method involving acoustics, solid mechanics, electromagnetics, and also thermodynamics. A simulation strategy is proposed in this chapter, which involves the simulation of the problem with different tools separately. The acoustic, mechanical and electromagnetic simulations are solved sequentially.



In the 2-D acoustic simulations, the axi-symmetric intensity distribution is calculated assuming a homogenous tissue. This assumption is valid in the sense that we are interested in the ultrasound intensity distribution inside the tissue, rather than the backscattered signal. As the problem involves only soft tissues, the beam shape of the ultrasound is not affected by the small reflections at the tissue interfaces.

A mechanical 3-D FDTD simulator is developed, which takes the intensity distribution output of the acoustic simulator as an input. The intensity distribution is used to calculate the acoustic radiation force. It also can take the realistic tissue ultrasound parameters as an input to manipulate the input intensity distribution according to the attenuation and reflection due to tissue inhomogeneity. The output of the mechanical simulator is the displacement distribution inside the tissue.

An electromagnetic 3-D FDTD simulator is developed, in which microwave transceiver system is simulated to obtain the received signal amplitude and phase. A method is introduced for calculating the scattered field component due to the vibration of the tissue. The displacement map inside the tissue in different time instants are used to calculate the Doppler component of the received signal.

Using the developed simulation tools, the forward problem can be analyzed with realistic numerical tissue models. Since the simulators are run separately, the coupling between different physical problems are not taken into account. For example, the effect of acoustic wave propagation to the dielectric distribution and the heating effect of acoustic waves on the electrical and the elastic parameters of the tissue are ignored. Nevertheless, it can be argued that these are second order effects, which does not influence the purpose of this thesis work.

## CHAPTER 4

### NUMERICAL SIMULATIONS

#### 4.1. Introduction

In this chapter, simulations for various scenarios are conducted in order to show the capability of the method for breast tumor detection. In the first part, simplified (homogeneous) breast models are used. A small cubic tumor is introduced inside the homogenous breast tissue. The Doppler component of the received signal is presented for linear scan of the ultrasound probe in axial ( $\hat{z}$ ) and lateral ( $\hat{x}$ ) directions. In the second part, a realistic numerical breast model is used in the simulations. The model, which is based on MRI data, is obtained from the phantom repository of University of Wisconsin Computational Electromagnetics (UWCEM) group [89]. A small cubic tumor is introduced inside the fibro-glandular tissue. Using the change in the phase of the received signal in the first cycle of vibration, the Doppler component of the received signal is calculated. The results are presented in the presence and in the absence of the tumor for linear scan of the ultrasound probe in axial ( $\hat{z}$ ) and lateral ( $\hat{x}$ ) directions. In addition, the simulations are conducted for the late time response when the shear waves are present inside the tissue. A four cycle amplitude modulated burst signal is used in these cases. The effect of shear waves on the received signal and tumor detection performance is analyzed.

#### 4.2. Simulations for the Tumor Inside Homogenous Tissue

In this first case, a small cubic tumor of 3 mm edge length is introduced inside a homogenous high adipose content tissue. The simulation geometry is shown in Figure 4-1. The ultrasound focus is scanned in  $\hat{x}$  and  $\hat{z}$  directions. The received signal is simulated using the simulation approach given in Chapter 3.

Firstly, acoustic simulations are conducted to obtain the ultrasound intensity distribution inside the tissue.

##### 4.2.1. Acoustic Simulations

The acoustic intensity distribution inside the tissue is the input for the mechanical simulations. Intensity map is calculated using the HIFU simulator tool developed by FDA [67]. This MATLAB tool solves axi-symmetric Khokhlov-Zabolotskaya-Kuznetsov (KZK) equation [68] in the frequency-domain. The simulation parameters are given in Table 4-1. The radius and the axial dimension of the computational domain are 2.1 cm and 9 cm, respectively.

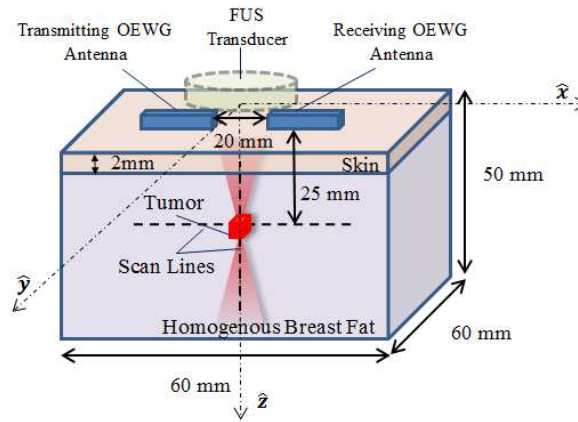


Figure 4-1: Simulation geometry for the simulations of tumor inclusion inside a homogenous tissue. Focus of the ultrasound transducer is at 25 mm depth inside the tissue. Water filled open-ended waveguides are placed on the 2 mm thick skin tissue. A tumor inclusion of 3 mm edge length size is introduced at 25 mm depth inside the high adipose content tissue. The focus is scanned in  $\hat{x}$  and  $\hat{z}$  directions.

The geometry is meshed with rectangular cells having  $32\mu\text{m}$  length in the radial direction and  $29\mu\text{m}$  length in the axial direction. The calculation time for the simulation was 46 minutes on an Intel 7 1.73 GHz dual core CPU notebook. The axial and lateral intensity beamwidths of the transducer are obtained as 6.75 mm and 0.48 mm, respectively. Spatial peak-pulse average value of intensity ( $I_{\text{SPPA}}$ ) for the amplitude modulated ultrasound beam is  $175\text{ W/cm}^2$ . Resultant pressure waveform, time average intensity, peak positive and negative pressure, and heat in the axial direction are plotted in Figure 4-2. The ultrasound beam intensity distribution output is saved to a text file to be used as an input of the mechanical simulator. It is assumed that the intensity beam profile is not affected by the reflections inside the soft tissue. The loss in ultrasound intensity due to inhomogeneity of the tissue is calculated in the mechanical simulator, which is given in the next subsection.

#### 4.2.2. Mechanical Simulations

The intensity distribution obtained in the acoustic simulation is used to calculate the mechanical force distribution inside the tissue. The simulation geometry is shown in Figure 4-3. Since the ultrasound waves are propagating in the  $\hat{z}$ -direction, the force is applied in the  $\hat{z}$ -direction. The acoustic and elastic parameters used in the calculations are given in Table 4-2. The chosen value of Young's constant for the homogeneous tissue is between the reported mean values of normal breast fat/fibro-glandular tissue and fibro-adenoma tissue [44]. This elasticity value used for the tumor is the reported mean value for intermediate-grade invasive ductal carcinoma [44].

Table 4-1: Parameters used for intensity calculations with HIFU Simulator

<i>Material Parameter</i>	<i>Material 1 (Water)[67]</i>	<i>Material 2 (Breast)</i>	<i>Transducer Parameter</i>	<i>Value</i>
Speed of sound (m/s)	1482	1479[71]	Outer radius (cm)	2.1
Mass density (kg/m <sup>3</sup> )	1000	1000	Inner radius (cm)	1
Attenuation (dB/m/MHz)	0.217	34[70]	Focusing Depth (cm)	6
Power of attenuation vs. frequency curve	2	1	Frequency (MHz)	3.3
Material transition distance (cm)	2.5-4.5	-	Power (W)	3.35
			No. Of Harmonics	150

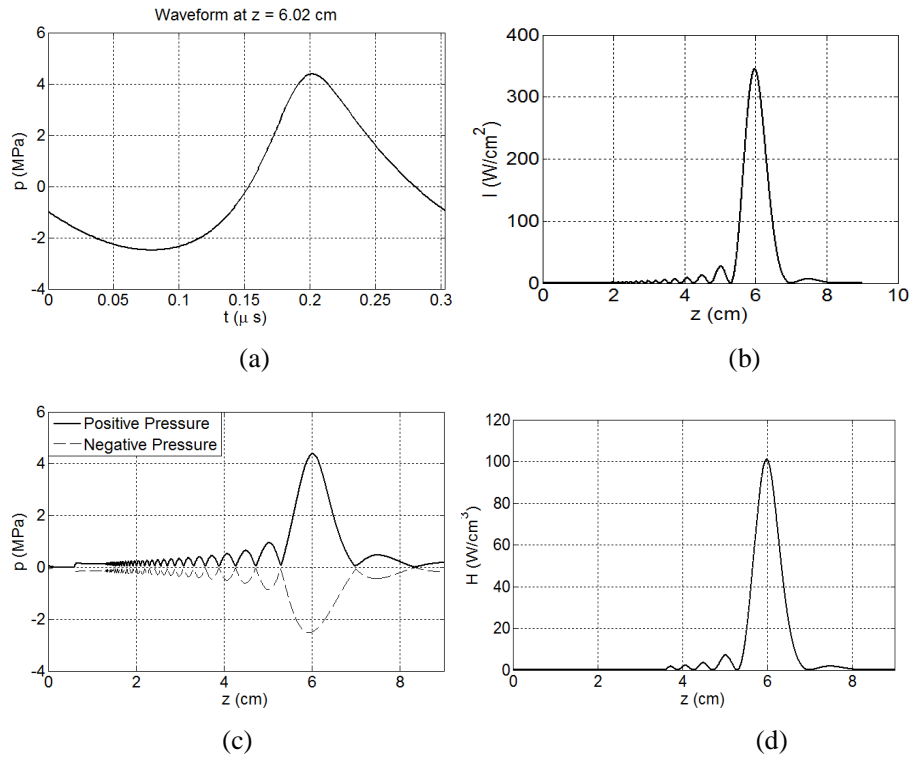


Figure 4-2: Acoustic simulation results for: (a) Pressure waveform, (b) Time average intensity, (c) Peak positive and negative pressure, (d) Heat, calculated in the axial direction.

In the acoustic simulation, tissue is modeled as a homogeneous breast fat. Therefore, the attenuation of the ultrasound due to skin layer and the tumor is not taken into account. In order to obtain more accurate results, the intensity distribution is altered to include the attenuation of the skin layer and tumor due to reflection and extraneous attenuation.

The extraneous attenuation due to reflection and absorption is calculated in the axial direction (direction of propagation) using [104]:

$$\xi_{i,j,k} = \xi_{i,j,k-1} e^{-2(\alpha_{i,j,k} - \alpha_0)\Delta z} \left[ 1 - \left( \frac{\eta_{i,j,k+1} - \eta_{i,j,k}}{\eta_{i,j,k+1} + \eta_{i,j,k}} \right)^2 \right] \quad (4-1)$$

$$I'(i\Delta x, j\Delta y, k\Delta z) = I(i\Delta x, j\Delta y, k\Delta z) \xi_{i,j,k} \quad (4-2)$$

where  $i, j$  and  $k$  are the voxel indices in  $\hat{x}$ ,  $\hat{y}$  and  $\hat{z}$ -direction, respectively.  $\xi_{i,j,k}$  is the extraneous attenuation coefficient for the  $(i, j, k)^{th}$  voxel due to inhomogeneity.  $\alpha_{i,j,k}$  (nepers/m) is the absorption coefficient of the  $(i, j, k)^{th}$  voxel,  $\alpha_0$  (nepers/m) is the absorption coefficient of the fat tissue,  $\Delta z$  (m) is the voxel dimension in the  $\hat{z}$ -direction.  $\eta_{i,j,k}$  (N.s/m<sup>3</sup>) is the acoustic impedance of the  $(i, j, k)^{th}$  voxel. The acoustic impedance is calculated assuming that the density of the tissue is constant throughout the tissue. It only includes the variation of the speed of sound inside the tissue.

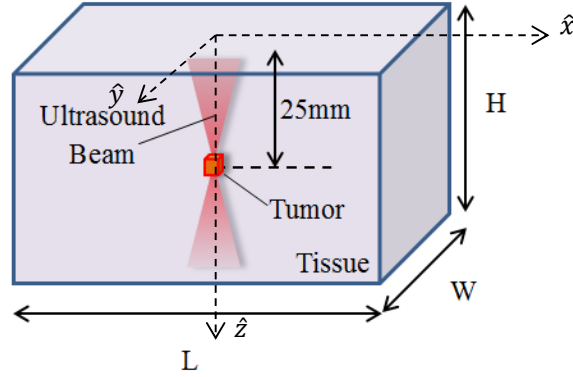


Figure 4-3: Simulation geometry for the mechanical simulations. A focused ultrasound transducer is assumed to be present upon homogenous breast tissue. Transducer is focused at 25 mm depth.

Table 4-2: Acoustic and mechanical parameters for different tissue types used in the mechanical simulations

<i>Tissue Type</i>	<i>Attenuation constant (dB/ cm/ Mhz)</i>	<i>Speed of sound (m/s)</i>	<i>Young's Modulus(kPa)</i>	<i>Poisson's ratio</i>
Fat	0.34[70]	1479 [71]	5	0.495
Skin	1.84 [80]	1479		
Tumor	0.79[70]	1550[71]	20	

In the homogeneous case,  $I'$  is the short-time average intensity distribution including the attenuation of the skin layer.  $I'$  is given by :

$$I'_{i,j,k} = \frac{p_{0,i,j,k}^2}{2\rho c_{s,i,j,k}} \quad (4-3)$$

where  $p_{0,i,j,k}$  is the peak pressure at the  $(i,j,k)^{th}$  voxel, and  $\rho c_{s,i,j,k}$  is the acoustic impedance for the  $(i,j,k)^{th}$  voxel. Using (2-1) and (4-3), the force distribution due to an amplitude modulated intensity can be calculated using:

$$F_{i,j,k} = \frac{\alpha_{i,j,k} I'_{i,j,k}}{c_{s,i,j,k}} (1 + \cos(\Delta\omega t)) \quad (4-4)$$

where  $\Delta\omega$  is the modulation or vibration frequency in *rad/s*.

Simulations are performed for three vibration frequencies: 125 Hz, 250 Hz and 500 Hz. The dimension of the problem is larger in the axial direction as the ultrasound beam width and the displaced region width are larger. Length (L) and width (W) are 80 mm, height (H) is 100 mm, and edge size of a cubic cell is 1 mm for 125 Hz excitation. For 250 Hz, tissue size is 40 mm (L) x 40 mm (W) x 80 mm (H) and cell edge size is 0.8 mm. For 500 Hz, tissue size is 21 mm (L) x 21 mm (W) x 51 mm (H) and cell edge size is 0.3 mm. The time steps used in the simulations are 9.19 $\mu$ s, 7.35  $\mu$ s, and 2.76  $\mu$ s for 125 Hz, 250 Hz, and 500 Hz, respectively. 3500 iterations are used for 125 Hz, and 2500 iterations are used for 250 Hz and 500 Hz simulations.

The simulations are run for two cases: One set with tumor inclusion and one set without tumor inclusion. A cubic tumor inclusion having a 3mm edge length is introduced at 25 mm depth inside the tissue for the simulations with tumor. Lateral and axial linear scan of the probe is simulated. Lateral scan is performed for 0 mm to +8 mm travel distance with 1 mm steps. For simulating the scan of the probe, the tumor is moved rather than the intensity

distribution. Axial scan is performed for -10 mm to +10 mm travel distance with 2 mm steps. Separate acoustic simulations are used for the scan in the axial direction since the material transition distance changes which correspond to the mechanical scan of the probe in the axial direction. Three dimensional displacement maps are formed at the time instants when the first maximum and first minimum displacement occur at the focus. The displacement distributions are stored in a file for each scan step in order to be used as input for the electromagnetic FDTD simulations.

The peak to peak displacement values calculated using the average of the first 3 cycles are given in Table 4-6. The displacement at the focus is plotted as a function of time in Figure 4-5 for 125 Hz, 250 Hz and 500 Hz. In order to visualize the influence of the tumor to the displacement inside the tissue, the displacement distributions are plotted for 500 Hz frequency at the first displacement instant for the cases tumor is present or not.

Table 4-3: The displaced region widths (DRW) and the peak-to-peak displacement values at the focus for the homogenous numerical phantom calculated by averaging the first 3 excitation cycles.

<b>Freq. (Hz)</b>	<b>Lateral DRW (mm)</b>	<b>Axial DRW (mm)</b>	<b>Displacement of tumor (<math>\mu\text{m}</math>)</b>	<b>Displacement of fat tissue (<math>\mu\text{m}</math>)</b>
125	2.1	9.8	16.73	15.03
250	1.9	8.7	5.28	9.61
500	1.7	8.4	1.44	1.94

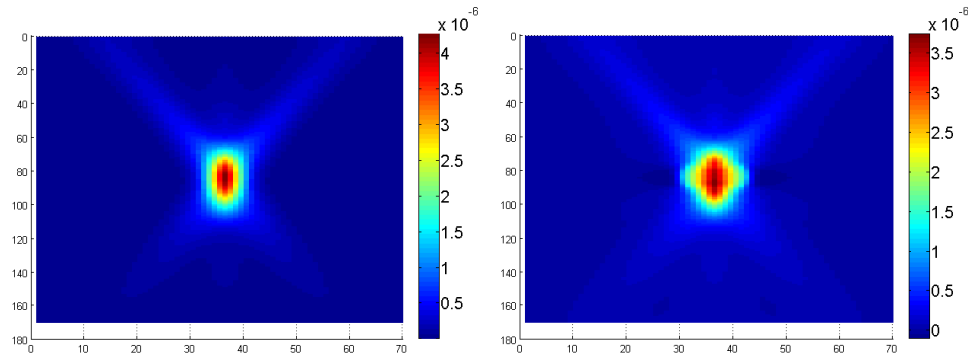


Figure 4-4: Displacement distribution inside the tissue at the first maximum displacement instant for 500 Hz vibration frequency. Left: Normal tissue, right: cubic tumor of 3mm edge length is introduced.

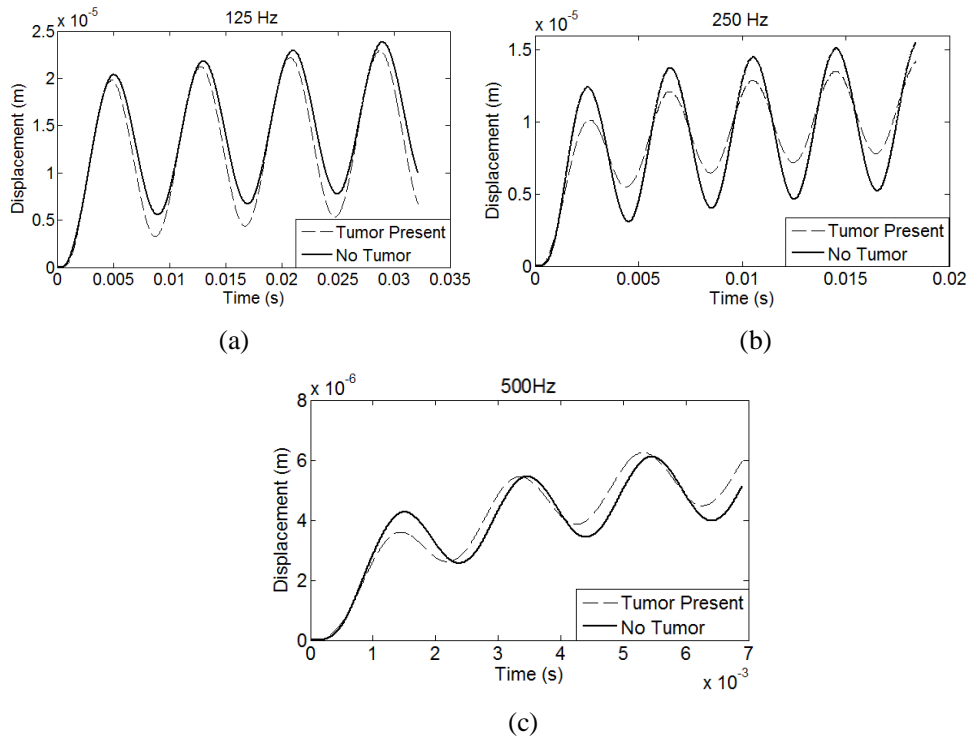


Figure 4-5: The displacement at the focus for homogenous model simulations for (a) 125 Hz, (b) 250 Hz, and (c) 500 Hz vibration frequencies. The tumor is not present in the solid line plots, whereas a cubic tumor with 3mm edge length is introduced in the dashed line plots.

### 4.2.3. Electromagnetic Simulations

In the electromagnetic simulation part, firstly the configuration of the antennas is chosen. Four different configurations are analyzed. In the first one, the antennas are arranged in E-plane configuration (Figure 2-12) with a 20 mm distance between them. In the second one, they are arranged again in E-plane configuration but placed side by side. In the third one, H-plane configuration with 20 mm distance is analyzed. In the last one, side by side H-plane arrangement is analyzed. The media, geometry and inclusion parameters are the same as in Figure 2-9. The normalized Doppler component with respect to the directly coupled signal is plotted as a function of depth in Figure 4-6.

Inspecting Figure 4-6, the following deductions can be made. When the antennas are away from each other, near surface performance is decreased, whereas deeper inclusions are sensed better. H-plane antenna alignment is better than E-plane alignment as the directly coupled signal is low. H-plane 20 mm arrangement gives better results after 12 mm depth. Therefore, H-plane-20mm alignment is selected for the following simulations.



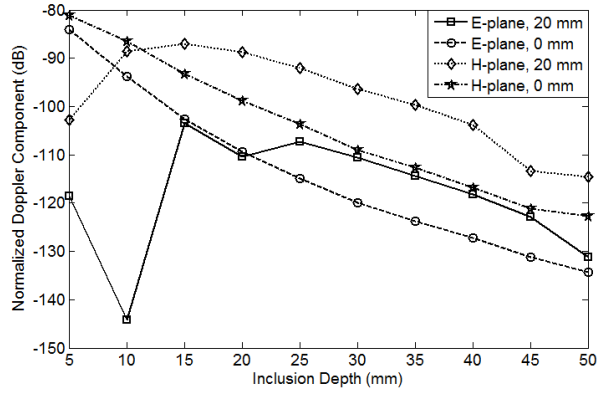


Figure 4-6: Doppler component to directly coupled signal ratio for different probe arrangements as a function of tumor depth.

The geometry of the electromagnetic simulations is shown in Figure 4-1. The dimensions of the tissue are: 60 mm (X) x 60 mm (Y) x 50 mm (Z). Cell size is 1 mm in all directions. The geometry is terminated with 10 cell PML layer in all directions. The microwave frequency is 5 GHz. The simulation time step is 1.11 picoseconds and 3600 simulation steps are performed for each simulation. Transmitting and receiving antennas are water-filled open ended waveguides of size 14 mm x 4 mm. They are aligned in H-plane with a 20 mm distance. For the cases tumor is introduced, it is placed to a 25 mm depth measured from the antenna apertures. The parameters used in the electromagnetic simulations are given in Table 4-4. Simulations are performed for the scan of the focus in the  $\hat{x}$  - direction from 0 mm to 8 mm with 1 mm steps with respect to the center of the tumor. It is assumed that the ultrasound probe and the tumor move together. Rather than moving the antennas and the displacement map, tumor is shifted in the  $\hat{x}$ - direction in the simulations. Simulations for the  $\hat{z}$  - direction scan are also performed from -10 mm to 10 mm distance with respect to the tumor center with 2 mm steps. The main frequency and the Doppler frequency components of the received signal are calculated for each scan point.

Table 4-4: Parameters Used In The Electromagnetic Simulations

<b>Frequency</b>	GHz	5
<b>Waveguide dimensions</b>	a (mm)	14
	b (mm)	4
<b>Thickness of the skin layer</b>	d (mm)	2
<b>Distance between transmitting and receiving waveguides</b>	s (mm)	1
<b>Relative dielectric constants</b>	Skin[22]	39.61-j12.86
	Fat [72]	4.48-j0.75
	water	77.15-j15.86

The amplitude of the main frequency component (directly coupled) of the received signal is calculated using:

$$S_{RX\_main} = \frac{|E_{t2\_nodisp}|}{|E_{t1\_nodisp}|} \quad (4-5)$$

Here,  $E_{t2\_nodisp}$  is the total electric field at the receiver antenna aperture for the undisplaced tissue simulation,  $E_{t1\_nodisp}$  is the total electric field at the transmitter antenna aperture for the undisplaced tissue simulation.  $S_{RX\_main}$  can also be calculated using the electric field values calculated with the displaced tissue simulations. The directly coupled signal level for 1 Watt TX output power is calculated as -35 dBm.

In order to calculate the Doppler component, the phase of the received signal is calculated at two instants: 1<sup>st</sup> maximum displacement at the focus and 1<sup>st</sup> minimum displacement at the focus. It is assumed that the phase oscillation is similar for the following cycles since the displacement oscillation amplitude is similar. The phase is calculated by converting the time domain signal to the frequency domain with Discrete Time Fourier Transform (DTFT). Using (3-24), the magnitude of the Doppler component can be calculated as:

$$S_{RX-Doppler} = A \left( \frac{P_{max} - P_{min}}{2} \right) \quad (4-6)$$

where  $A$  is the normalized amplitude of the scattered field :

$$A = \frac{|E_{s2\_nodisp}|}{|E_{t1\_nodisp}|} \quad (4-7)$$

Here,  $E_{s2\_nodisp}$  is the scattered electric field at the receiver antenna aperture for the undisplaced tumor simulation,  $E_{t1\_nodisp}$  is the electric field at the transmitter antenna aperture for the undisplaced tumor simulation.  $A$  can also be calculated using the electric field values calculated with the displaced tissue simulations. The result is similar since the amplitude change is too small ( $M \ll 1$  in (2-36)) and negligible.  $P_{max}$  is the phase difference of the scattered signal at the 1<sup>st</sup> maximum displacement instant:

$$P_{max} = Arg(E_{s2\_disp}^{max}) - Arg(E_{s2\_nodisp}^{max}) \quad (4-8)$$

$E_{s2\_disp}^{max}$  is the electric field at the receiver antenna aperture scattered from the displaced tissue for the 1<sup>st</sup> maximum displacement instant.  $E_{s2\_nodisp}^{max}$  is the electric field at the receiver antenna aperture scattered from the undisplaced tissue for the 1<sup>st</sup> maximum displacement

instant.  $P_{min}$  is calculated in a similar manner using the electric field values from the simulation results for the 1<sup>st</sup> minimum displacement instant.

For 1 Watt output power, the scattered signal from the stationary tumor is found to be -59.7 dBm in all simulations since the relative positions of antennas and the tumor does not change.

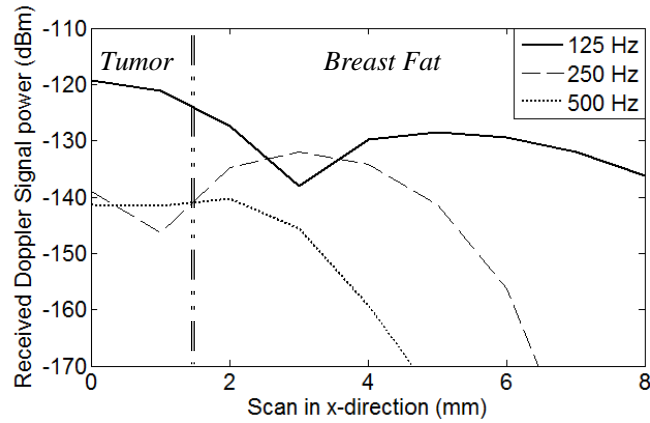


Figure 4-7: Signal level at the Doppler frequency for 1 W microwave output power as a function of scan position in  $\hat{x}$  direction calculated using the 1<sup>st</sup> cycle of the vibration. Tumor with 3 mm edge size is present at 25 mm depth. The boundary of the tumor is shown as dashed-dotted line.

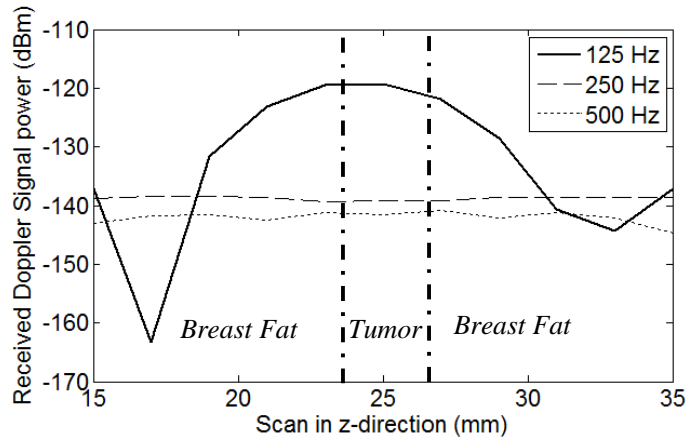


Figure 4-8: Signal level at the Doppler frequency for 1 W microwave output power as a function of scan position in  $\hat{z}$  direction calculated using the 1<sup>st</sup> cycle of the vibration. Tumor with 3 mm edge size is present at 25 mm depth. The boundary of the tumor is shown as dashed line.

For the  $\hat{x}$ -direction scan, the signal component at the Doppler frequency is plotted in Figure 4-7 as a function of scan position. The 3 dB width of the signal is 2.5 mm for 125 Hz and 5.6 mm for 500 Hz vibration frequencies. For 250 Hz vibration, the signal decreases about 7 dB rapidly in the 1<sup>st</sup> millimeter but increases after that point. Taking the peak points at the maximum extents as reference, 3 dB width is calculated as 8 mm. The results show that 125 Hz vibration yields the highest resolution. The displaced region widths become larger when a stiff inclusion (tumor) is introduced (Figure 4-4). This effect is more pronounced for frequencies 250 Hz and 500 Hz than 125 Hz vibration frequency, which is the reason of the low resolution in 250 Hz and 500 Hz frequencies.

For the  $\hat{z}$ -direction scan, the signal component at the Doppler frequency is plotted in Figure 4-8 as a function of focus depth. The 3 dB width of the signal is 6 mm for 125 Hz. Larger displaced region widths for higher frequencies are also observed in this direction.

### 4.3. Simulations with the Realistic Breast Tissue Model

The breast tissue models used in the previous studies are homogenous. However, breast tissue is inhomogeneous containing mammary glands (lobules) and connective tissues. Anatomically realistic numerical models of the tissues can be extracted from MRI images, which provide high contrast tissue differentiation. UWCEM (University of Wisconsin Computational Electromagnetics) group has an online 3-D breast phantom repository [89]. In the repository, there are 9 numerical breast phantom models classified according to ACR (American College of Radiology) that can be used in electromagnetic FDTD simulations. ACR classifies breast into 4 classes [105]:

- Class I** : The breast is almost entirely fat.
- Class II** : There are scattered fibro-glandular densities.
- Class III** : The breast is heterogeneously dense. This may lower the sensitivity of mammography.
- Class IV** : The breast tissue is extremely dense, which could obscure a lesion in mammography.

Slices of the provided models for different classes are given in Figure 4-9.

The numerical phantoms are derived from T1 weighted magnetic resonance images from patients in a prone position. The voxel sizes of the phantoms are: 0.5 mm x 0.5 mm x 0.5 mm. The dielectric properties of each voxel can be calculated with the provided files for each phantom. A Class III numerical phantom is used in this study for mechanical and electromagnetic simulations. In order to decrease computer demands, only the interested region of the phantom is used.

For acoustic simulations, same acoustic intensity distributions as in the homogeneous tissue case (Section 4.2.1) are used since the acoustic simulator tool can only simulate homogeneous tissue.

### 4.3.1. Mechanical Simulations

The intensity distribution is imported in the mechanical simulator for calculating the mechanical force distribution. The 3-D numerical breast phantom model from UWCEM website (ID: 080304) is also imported. The tissue is categorized into 3 groups in the model according to the media type value for the numerical phantom [89]: Fibro-connective/glandular, fatty, and transitional tissues. In the original model data, there are also sub-categories for fatty and glandular tissue types. These sub-categories are not taken into account, and the same attenuation and speed values are assigned to all sub-categories. The attenuation and the speed parameters are assigned to the tissue model according to Table 4-5. Fibro-connective/ glandular and fatty tissue parameters are taken from [70] and [71]. The average value of them is used for the transitional tissue.

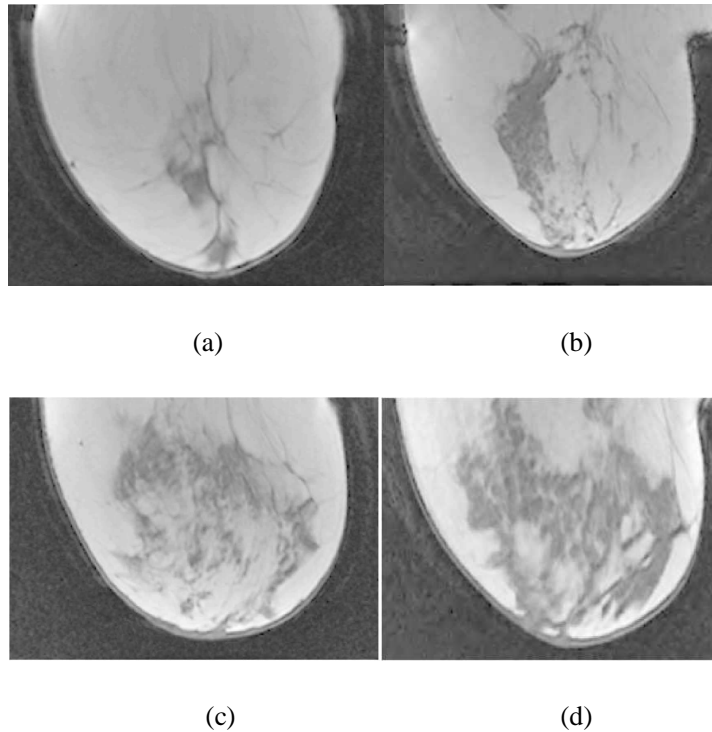


Figure 4-9: Four classes of ACR categorized breast images in UWCEM phantom repository [89]: (a) Class I, (b) Class II, (c) Class III, (d) Class IV.

In the acoustic simulations, tissue is modeled as a homogeneous breast fat. Therefore, the attenuation of the ultrasound due to tissue inhomogeneity is not taken into account. In order to obtain realistic results, the intensity is altered using (4-1) to include this effect.

The computation domain size is same as the homogeneous case. Length (L) and width (W) are 80 mm, height (H) is 100 mm, and edge size of a cubic cell is 1 mm for 125 Hz

excitation. For 250 Hz, tissue size is 40 mm (L) x 40 mm (W) x 80 mm (H) and cell edge size is 0.8 mm. For 500 Hz, tissue size is 21 mm (L) x 21 mm (W) x 51 mm (H) and cell edge size is 0.3 mm. The time steps used in the simulations are 9.19 $\mu$ s, 7.35  $\mu$ s, and 2.76  $\mu$ s for 125 Hz, 250 Hz, and 500 Hz, respectively. 3500 iterations are used for 125 Hz, and 2500 iterations are used for 250 Hz and 500 Hz simulations. Figure 4-10 shows the numerical phantom and the size of the numerical model used in the mechanical simulations.

Table 4-5: Acoustic and mechanical parameters for different tissue types used in the mechanical simulations

<i>Tissue Type</i>	<i>Attenuation constant (dB/ cm/ Mhz)</i>	<i>Speed of sound (m/s)</i>	<i>Young's Modulus(kPa)</i>	<i>Poisson's ratio</i>
Fibroconnective/glandular	1.5	1553	5	0.495
Fatty	0.34	1472		
Transitional	0.9	1513		
Tumor	0.79	1550	20	

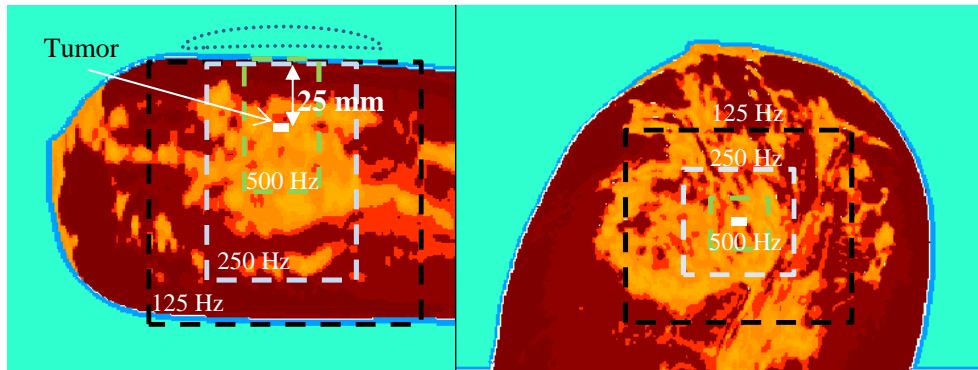


Figure 4-10: The breast phantom used in the simulations (Left: Side view, Right: Top view).The yellow region is fibro-glandular tissue, red region is fat tissue. The extent of the simulation geometry is shown in black dashed line for 125 Hz, light blue dashed line for 250 Hz, and green dashed line for 500 Hz. The place of the virtual ultrasound probe is shown in the left figure. The tumor is depicted in white color.

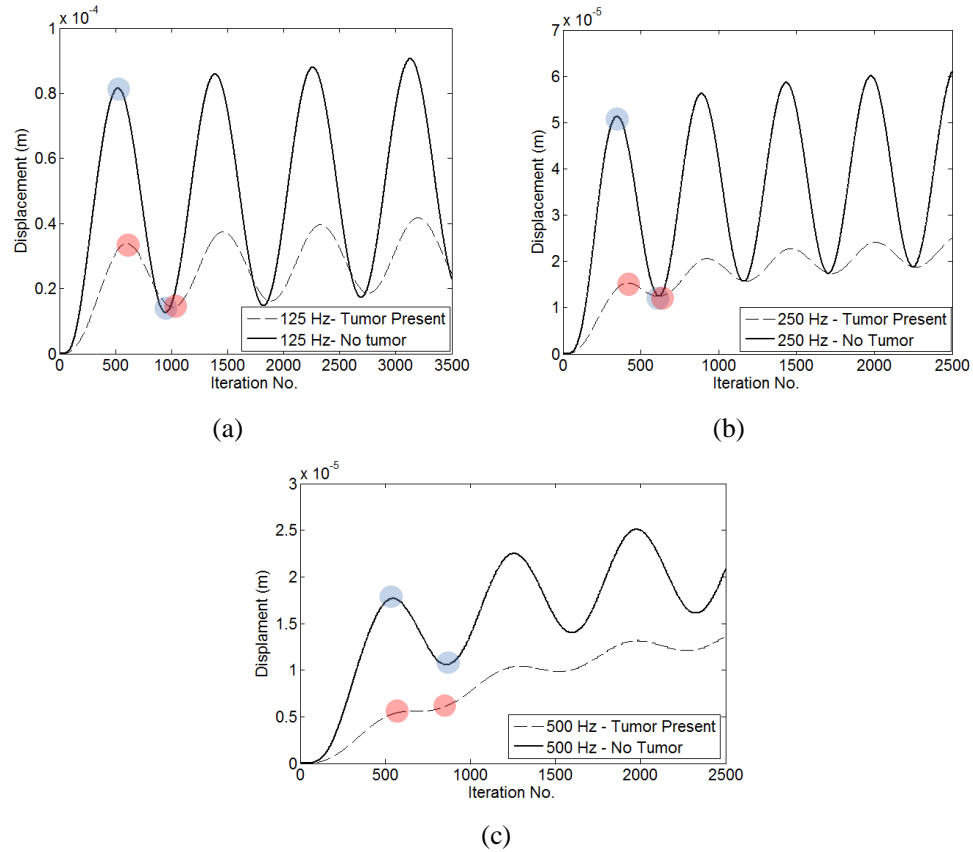


Figure 4-11: The displacement at the focus for realistic model simulations. The tumor is not present in the solid line plots, whereas a cubic tumor with 3mm edge length is introduced in the dashed line plots. (a) 125 Hz vibration frequency, (b) 250 Hz vibration frequency, (c) 500 Hz vibration frequency. The moments when the displacement distribution is exported (1<sup>st</sup> maximum and 1<sup>st</sup> minimum) to a text file are shown with circles.

Table 4-6: The displaced region width (DRW) and the displacement values at the focus mechanical simulations for the realistic phantom.

Freq. (Hz)	Lateral DRW (mm)	Axial DRW (mm)	Displacement of tumor ( $\mu\text{m}$ )	Displacement of realistic tissue ( $\mu\text{m}$ )
125	2.4	10	9.75	34.65
250	1.76	8.5	1.4	19.25
500	1.64	8.4	0.26	3.45

Lateral and axial linear scan of the probe is simulated for two cases: One without any inclusions, and one with an inclusion representing the tumor. A cubic tumor inclusion having a 3mm edge length is introduced at 25 mm depth inside the fibro glandular tissue for the

cases with tumor inclusion. Lateral scan is performed for -10 mm to +10 mm travel distance with 1 mm steps. Axial scan is performed for -8 mm to +8 mm travel distance with 2 mm steps. Separate acoustic simulations are used for the scan in the axial direction since the material transition distance changes as the mechanical position of the probe changes in the axial direction. The displacement at the focus is plotted as a function of time in Figure 4-11 for 125 Hz, 250 Hz and 500 Hz. The displacement values calculated from the average of maximum and minimum displacements are given in Table 4-6.

### 4.3.2. Electromagnetic Simulations

The geometry of the electromagnetic simulations is shown in Figure 4-12. The dimensions of the tissue are: 60 mm (X) x 60 mm (Y) x 50 mm (Z). Cell size is 1 mm in all directions. The geometry is terminated with 10 cell PML layer in all directions. The frequency of operation is 5 GHz. The simulation time step is 1.11 picoseconds and 3600 simulation steps are performed for each simulation. Water-filled open-ended waveguide antennas are placed on the tissue with 20 mm separation. For the cases which tumor is introduced, it is placed to a 25 mm depth from the top of the skin layer. The received signal at the Doppler frequency is calculated for -8 mm to 8mm scan in  $\hat{x}$  - direction with 1 mm steps, and -10 mm to 10 mm scan in  $\hat{z}$ -direction with 2 mm steps, with respect to the center of the tumor. For the  $\hat{x}$  - direction scan simulations, the realistic model is shifted together with the tumor in the  $\hat{x}$  - direction without changing the position of the antennas and the displacement map. For the  $\hat{z}$  - direction scan simulations, displacement map is changed according to the position of the ultrasound transducer. The displacement maps generated by the mechanical simulator are imported for each position of ultrasound focus for the  $\hat{z}$  - direction scan.

Class III type breast phantom (ID: 080304) model from the UWCEM repository is imported to the simulator as in the mechanical simulations. Figure 4-13 shows the dielectric distribution of the model for 3 axes cuts. A reduced portion of the model is used in the simulations (Figure 4-14).

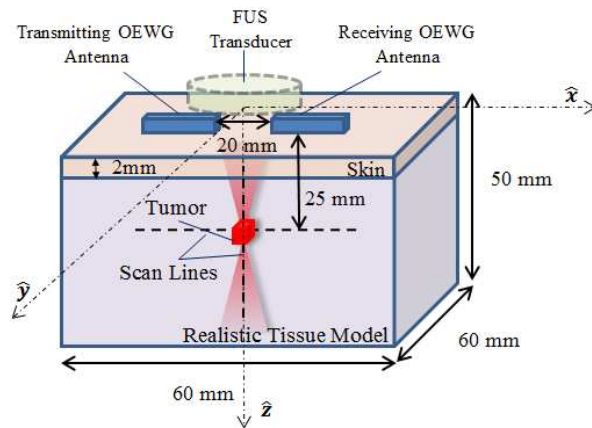
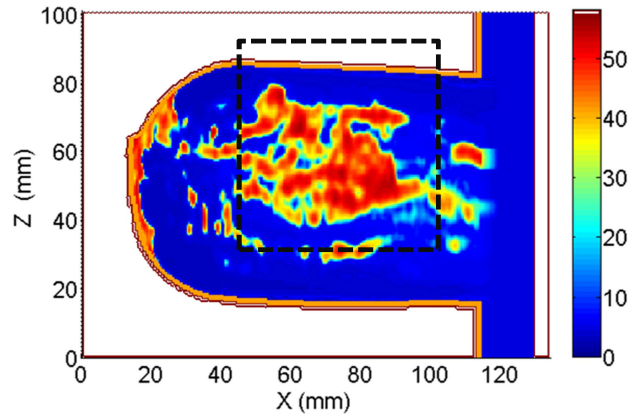
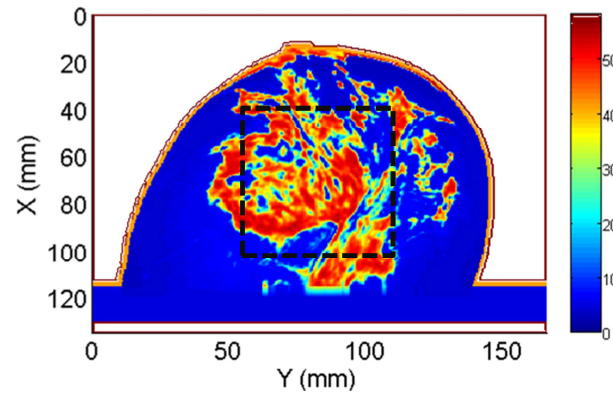


Figure 4-12: Geometry for the electromagnetic simulations for realistic numerical tissue model.

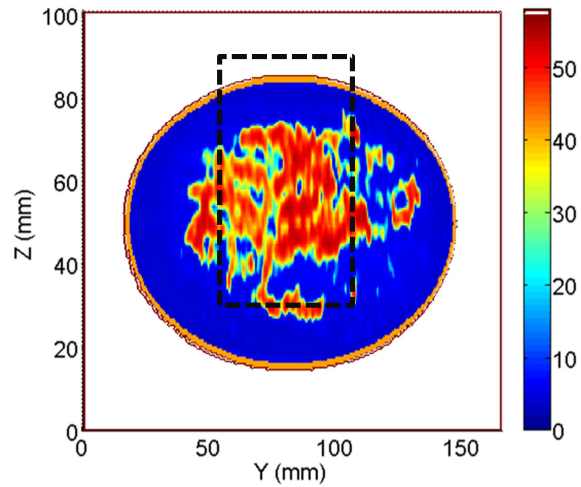




(a)

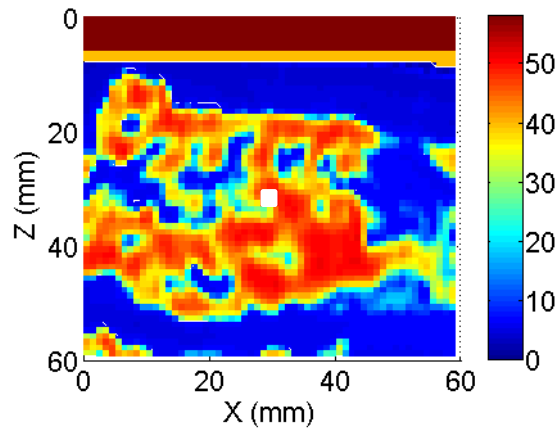


(b)

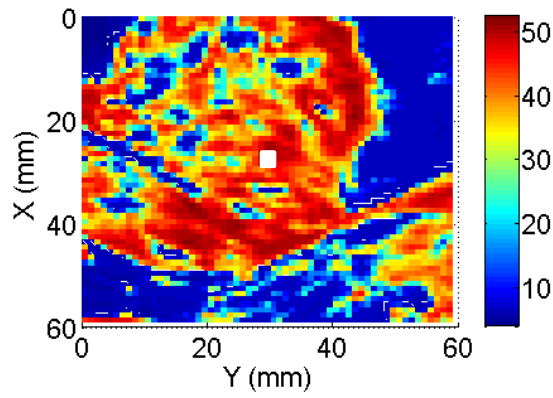


(c)

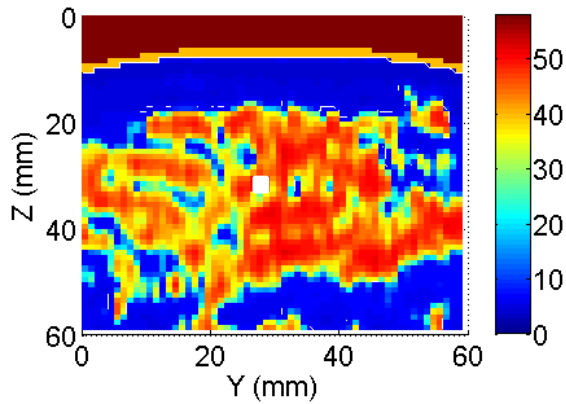
Figure 4-13: The realistic numerical breast model. The dielectric distribution inside the tissue is shown for: (a)  $Y=81.5$  mm cut, (b)  $Z=58$  mm cut, (c)  $X=75$  mm cut. The intersection of the cut planes is the central point of tumor, which is introduced as a cubic inclusion with 3 mm edge length. The boundaries for the reduced model are shown with a dashed rectangle. The rectangle is moved in the  $-$  direction for lateral scan simulations.



(a)



(b)



(c)

Figure 4-14: The reduced numerical model used in the electromagnetic simulations. The dielectric distribution is shown for: (a)  $Y=30$  mm cut, (b)  $Z=30$  mm cut, (c)  $X=30$  mm cut. The intersection of the cut planes is the central point of tumor which is introduced as a cubic inclusion with 3 mm edge length. Tumor is shown as a white box.

The 3-D displacement distribution is imported from the text files generated by the mechanical simulator. The displacement maps ( $Y=30$  mm cut) at the 1<sup>st</sup> maximum displacement instant of the focal point are given in Figure 4-15 in the absence and in the presence of the tumor for 125 Hz, 250 Hz and 500 Hz vibration frequencies.

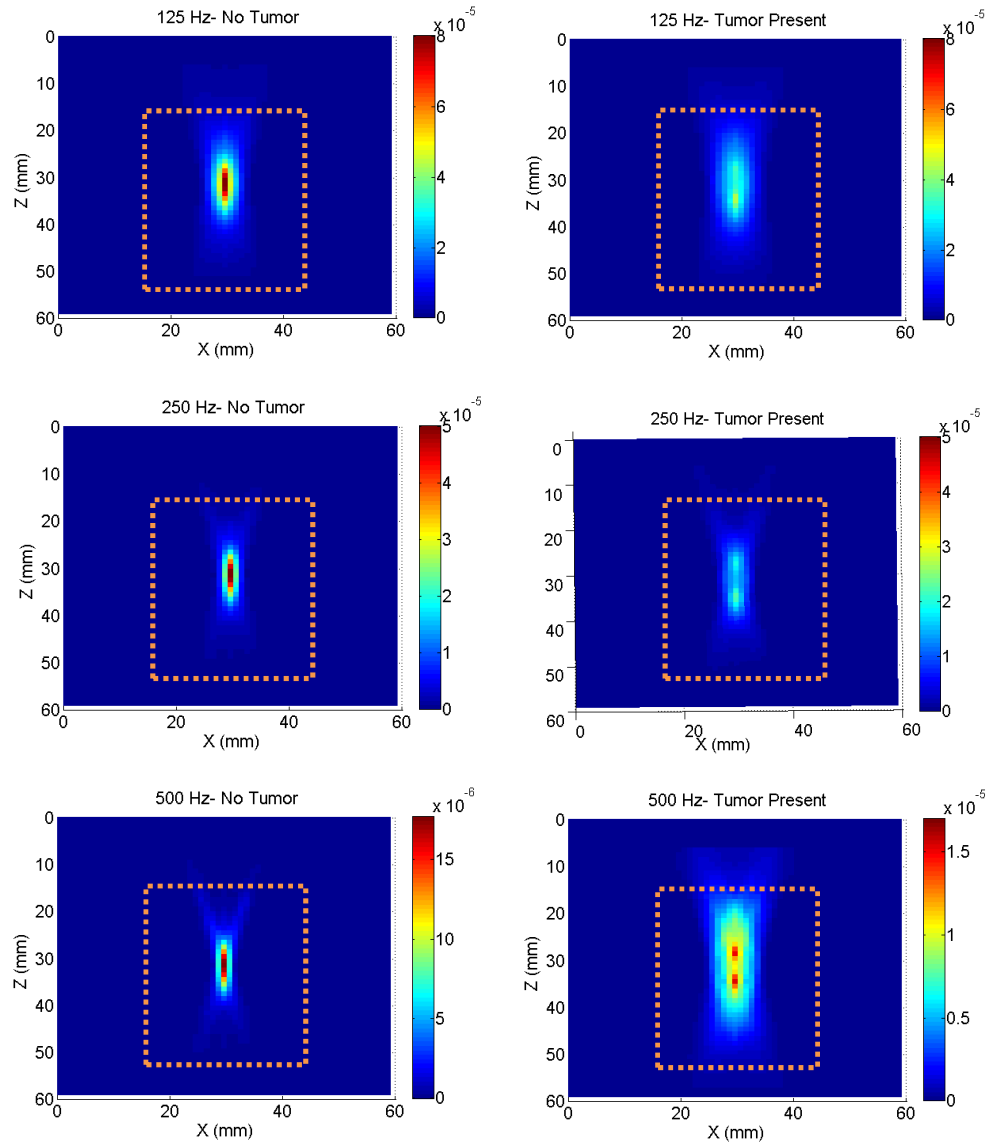


Figure 4-15: Displacement map cuts ( $Y=30$ mm) at the 1<sup>st</sup> maximum peak at the focus imported to the electromagnetic simulations. The displacement maps are shown in the presence and in the absence of the tumor inclusion for 125 Hz, 250 Hz, and 500 Hz vibration frequencies. The vibrating part for the scattering field calculation is depicted by a rectangle.

In order to calculate the Doppler component as given in the method described in Section 3.3.1., firstly the total field is calculated. To calculate the scattered field from the vibrating region using the Volume Equivalence Theorem, the electric field values must be stored for that region. The volume of the vibrating region is selected such that the maximum displacement at the lateral boundary is smaller than %1.5 of the maximum displacement for all the snapshots and vibration frequencies. The region in which the fields are stored is 30 mm (X) x 30 mm (Y) x 40 mm (Z). 4.6 Gigabytes (30 x 30 x 40 x 3600 x 3 x 8) memory is required to store the electric field for the whole simulation time. This region and the Volume Equivalent geometry are shown on the displacement map in Figure 4-16.

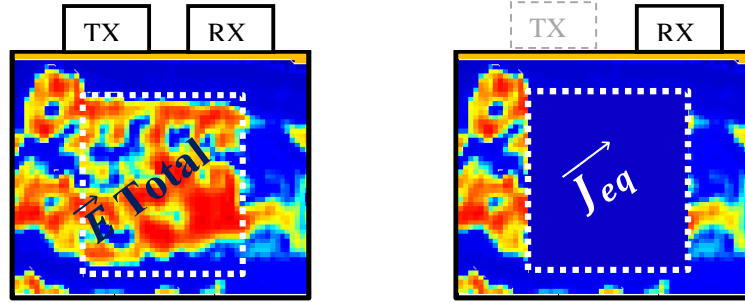


Figure 4-16: Geometries for the original (left) and the volume equivalent (right) problems for the realistic electromagnetic simulations.

The volume equivalent current update equation for the  $i, j, k^{th}$  cell inside the vibrating region is:

$$\vec{J}_{eq,i,j,k}^n = \left( \varepsilon_{obj,i,j,k} - \varepsilon_b \right) \frac{\vec{E}_{obj,i,j,k}^{n+1} - \vec{E}_{obj,i,j,k}^n}{\Delta t} + \left( \sigma_{obj,i,j,k} - \sigma_b \right) \frac{\vec{E}_{obj,i,j,k}^{n+1} + \vec{E}_{obj,i,j,k}^n}{2} \quad (4-9)$$

where  $\varepsilon_{obj}$ ,  $\sigma_{obj}$  and  $\varepsilon_b$ ,  $\sigma_b$  are the permittivity and the conductivity values of the realistic tissue model and the background tissue (which is the breast fat :  $\varepsilon_b = 4.48$ ,  $\sigma_b = 0.11$  S/m [72]), respectively.  $\vec{E}_{obj}$  is the stored total electric field component inside the vibrating region volume in the first simulation. The received signal at the RX antenna is the scattered signal from the vibrating region.

The phase of the scattered signal is calculated at two instants: 1<sup>st</sup> maximum displacement at the focus and 1<sup>st</sup> minimum displacement at the focus (shown in Figure 4-11). It is observed that the displacement oscillation amplitude is similar for the following cycles. Therefore, the phase oscillation amplitude is also assumed to be similar. The phase is calculated by converting the time domain signal to the frequency domain with Discrete Time Fourier

Transform (DTFT). The Doppler component of the received signal is calculated in a similar procedure given in Section 4.2.3.

The main frequency component (i.e. the coupled signal at the transmitted signal frequency) for 1 Watt TX output power is given in Figure 4-17. This component varies as a function of scan position since the tissue is inhomogeneous.

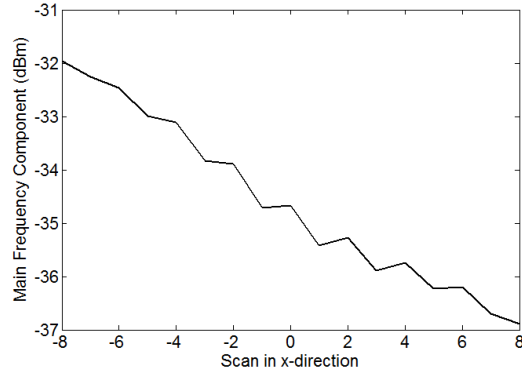
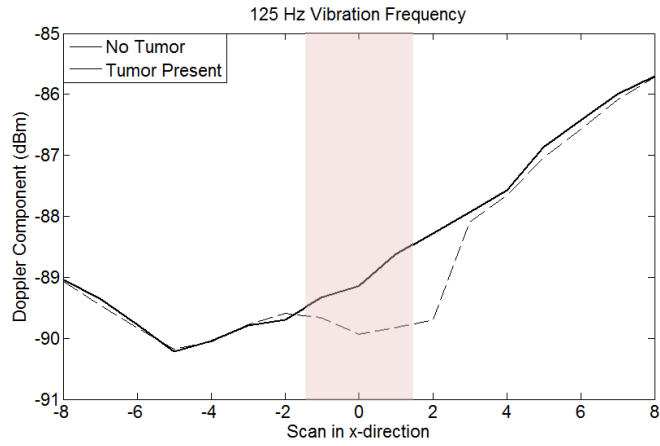


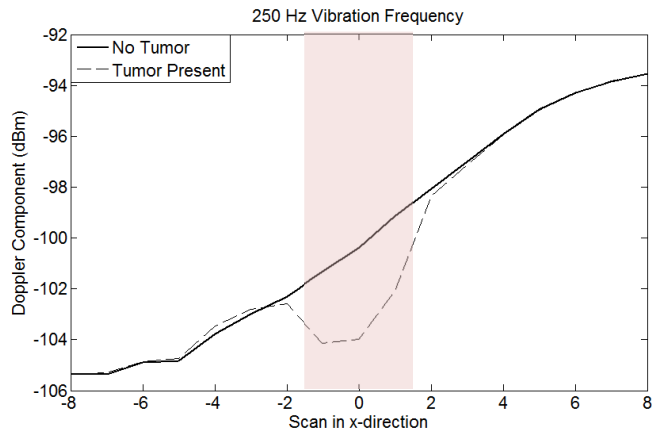
Figure 4-17: Main frequency component of the received signal for the realistic simulation as a function of scan distance.

The Doppler component of the received signal is plotted as a function of  $\hat{x}$ -direction scan in Figure 4-18 for 125 Hz, 250 Hz, and 500 Hz vibration frequencies. The effect of tumor is also given in the plots. The width of the tumor (3 mm) is resolved well for all frequencies as the DRW is small in the lateral direction. It is observed that the signal level decreases about 1 dB, 3 dB and 10 dB when the focus is on the tumor for 125 Hz, 250 Hz and 500 Hz vibration frequencies, respectively. It is also observed for 500 Hz that the signal level increases when the focus is at the tumor center. The reason can be best understood examining the axial displacement plots (Figure 4-21). When the focus is on the tumor, the displacement magnitude and the difference between displacement distributions is larger than the case focus is shifted to 1 mm. This effect is only observed for 500 Hz vibration frequency, which may be caused by the small displacement values and smaller DRW for this frequency.

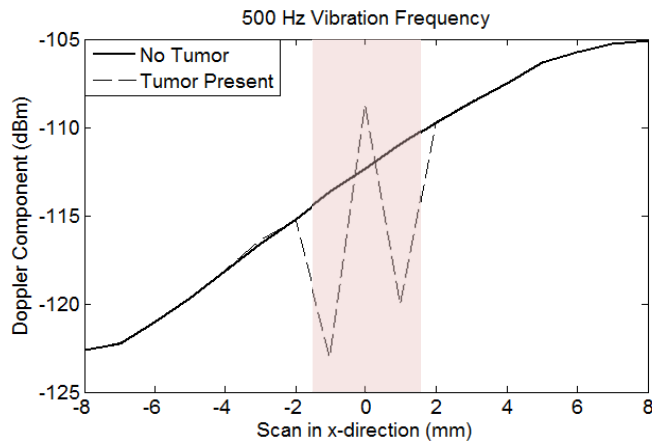
In Figure 4-19, signal level difference for multiple vibration frequencies are given. When the tumor is not present, the behavior of the differential signal level is smooth as a function of scan distance. However, if there is a tumor, there are abrupt changes at the location of tumor, especially if 500 Hz vibration frequency is involved. This information can be used to identify the presence of a tumor. In Figure 4-20, the Doppler component of the received signal is plotted as a function of  $\hat{z}$ -direction scan for 125 Hz, 250 Hz, and 500 Hz vibration frequencies. The effect of tumor is given in the plots. The resolution is lower than the resolution in  $\hat{x}$ -direction in this case as the DRW is high.



(a)

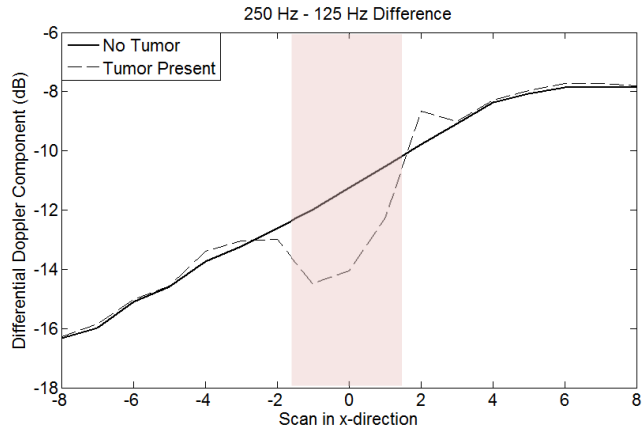


(b)

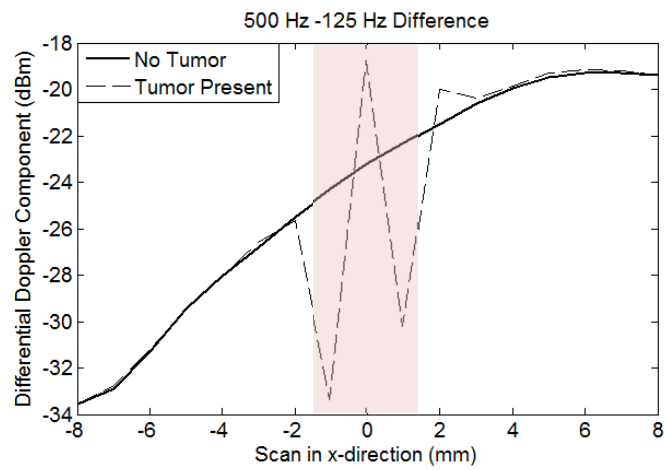


(c)

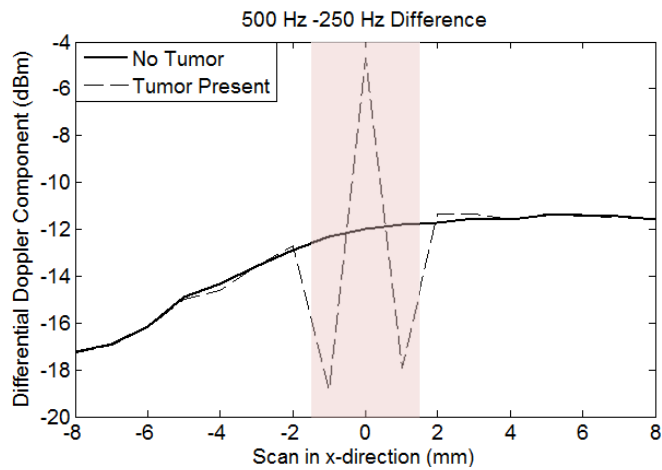
Figure 4-18: Doppler component of the received signal as a function of lateral scan distance in the presence and in the absence of the tumor for (a) 125 Hz, (b) 250 Hz, and (c) 500 Hz vibration frequency. The place of tumor is shown as a pink region.



(a)



(b)



(c)

Figure 4-19: Differential Doppler component of the received signal as a function of scan distance in the presence and in the absence of the tumor for (a) 125 Hz – 250 Hz, (b) 125 Hz – 500 Hz, (c) 250 Hz – 500 Hz frequencies. The place of tumor is shown as a pink region.

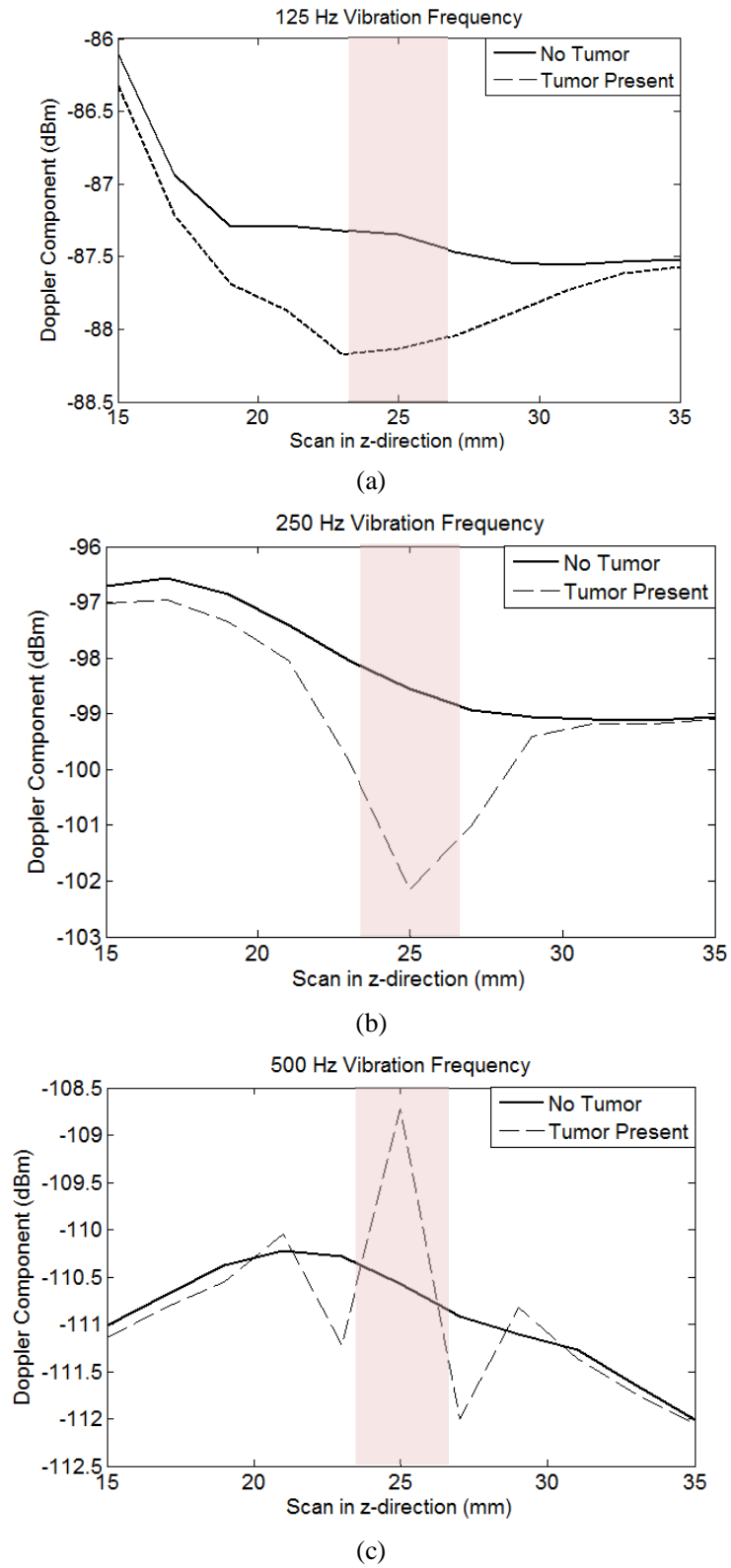


Figure 4-20: Doppler component of the received signal as a function of axial scan distance in the presence and in the absence of the tumor for (a) 125 Hz, (b) 250 Hz, (c) 500 Hz vibration frequency. The place of tumor is shown as a pink region.



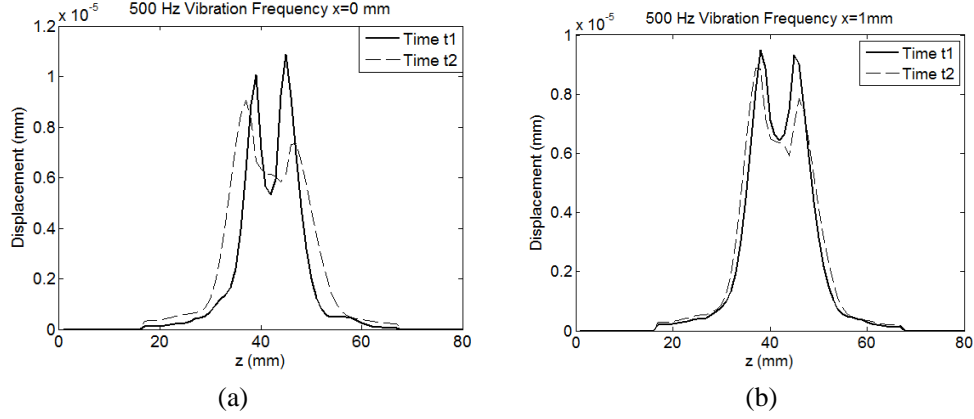


Figure 4-21: Axial displacement plots for 500 Hz frequency at maximum and minimum displacement instants of the first cycle for (a)  $x = 0$  mm, (b)  $x = 1$  mm scan position.

#### 4.4. Late Time Response

In the previous section, the results are presented for a single excitation cycle. As the sinusoidal mechanical excitation continues, the shear waves propagate transversally inside the tissue. Therefore, the phase of the received microwave signal also depends on the transversal displacement and the dielectric distribution outside the focal region. The effect of longer excitation time is studied in this section. The acoustic, mechanical and electromagnetic simulation models are similar to the ones used in Section 4.3. For 4 cycles of excitation, the displacement distribution inside the tissue is sampled at the maximum and minimum displacement instants of the focal point. Using the FDTD electromagnetic simulator, the phase of the received signal is calculated to obtain the signal component at the Doppler frequency. The focal scan is performed in the  $\hat{x}$  -direction from 0 mm to 5 mm in 1 mm steps. Simulations are conducted for 125 Hz, 250 Hz, and 500 Hz vibration frequencies. For 0 mm scan point, the displacement of the focal point is presented and the sampling instants are shown in Figure 4-22 (a). In Figure 4-22 (b), the phase of the received signal at these sampling instants is plotted. It is observed that the insertion phase decreases incrementally. The sinusoidal variation in phase due to vibration is added on the slow variation. The variation of the phase in the received signal can be denoted by a time varying signal  $k(t)$ . The received signal can be expressed by:

$$\begin{aligned}
 S_{RX}(t) = & B \cos\left(\omega_m t + \frac{4\pi R}{\lambda} + k(t) + \phi\right) = B \cos\left(\omega_m t + \phi + \frac{4\pi R}{\lambda}\right) \cdot \cos(k(t)) \\
 & - B \sin\left(\omega_m t + \phi + \frac{4\pi R}{\lambda}\right) \cdot \sin(k(t))
 \end{aligned} \tag{4-10}$$

Since  $k(t)$  is much smaller than unity,  $S_{RX}(t)$  can be written as:

$$S_{RX}(t) = B \cos\left(\omega_m t + \phi + \frac{4\pi R}{\lambda}\right) - Bk(t) \sin\left(\omega_m t + \phi + \frac{4\pi R}{\lambda}\right) \quad (4-11)$$

Therefore, the spectrum of  $k(t)$  is shifted to the microwave carrier frequency  $\omega_m$ . Since the vibration frequency is known, a matched filter can be used to extract the vibration (Doppler) frequency component of the received signal.

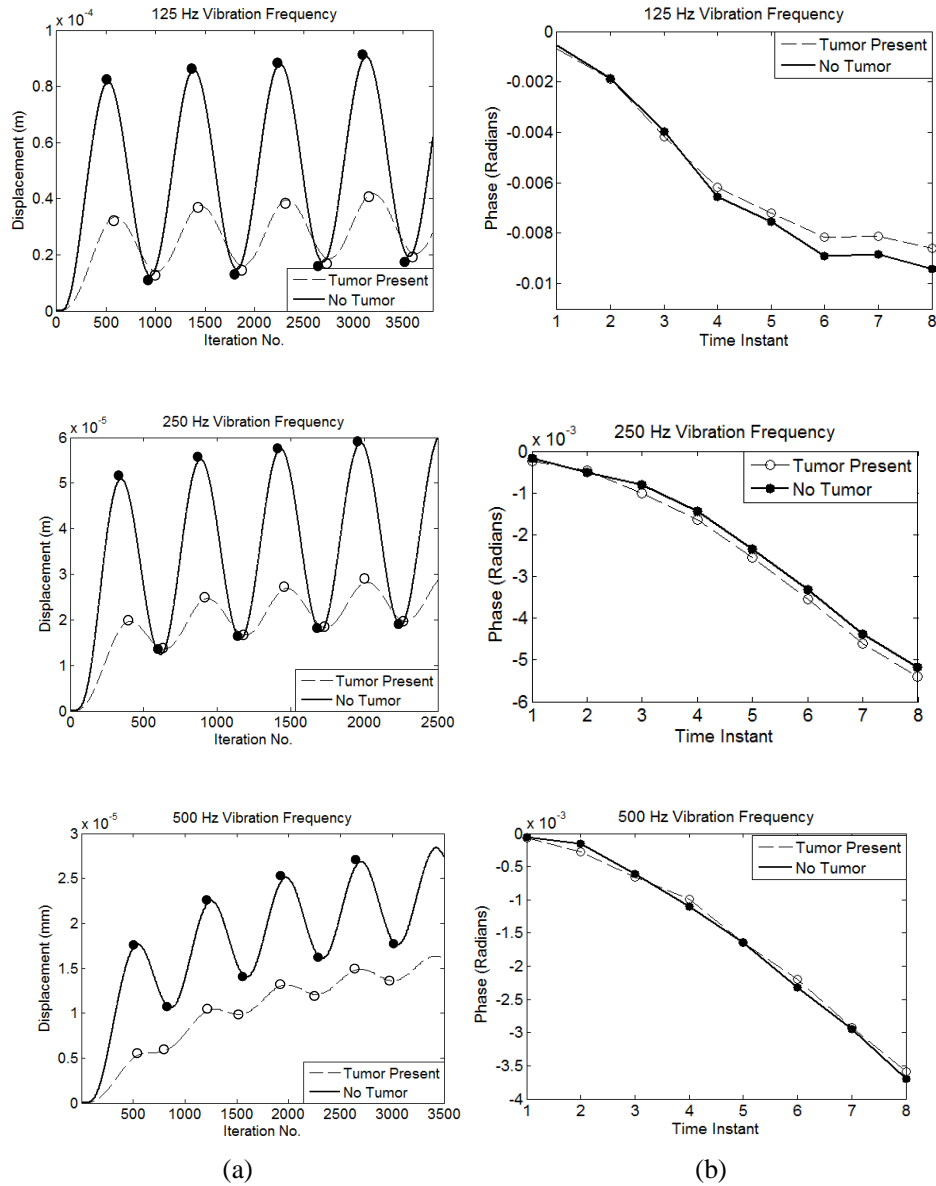
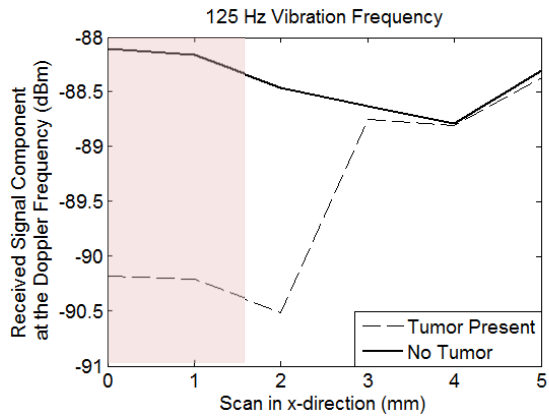
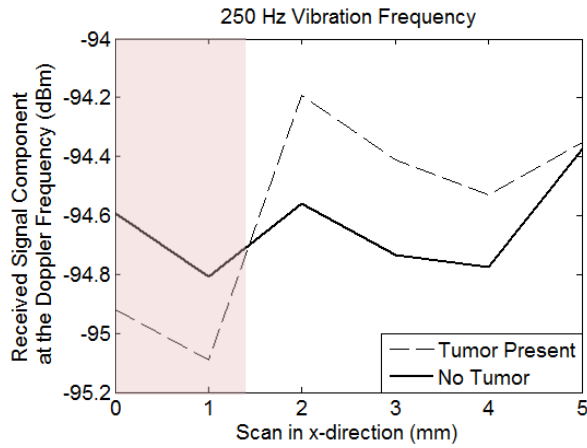


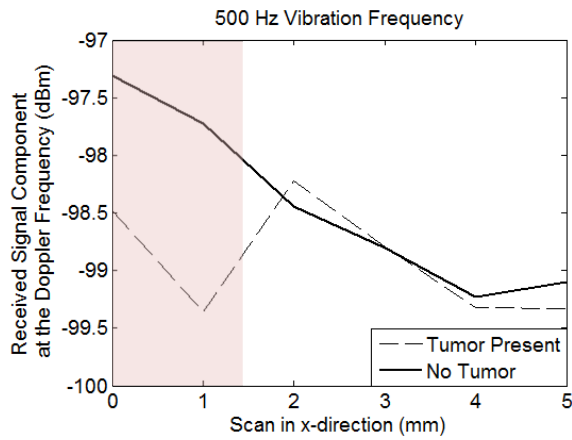
Figure 4-22: (a) Displacement of the focal point and the sampling instants in the presence and in the absence of the tumor at the focal point for 125 Hz, 250 Hz and 500 Hz vibration frequencies at 0 mm scan point. (b) Phase of the received signal at the sampled time instants in the presence and in the absence of the tumor at the focal point for 125 Hz, 250 Hz and 500 Hz vibration frequencies at 0 mm scan point.



(a)



(b)



(c)

Figure 4-23: Simulation results for the received signal component (4 cycles of excitation) at the Doppler Frequency. Vibration is applied at 125 Hz, 250 Hz, and 500 Hz. The place of tumor is shown as a pink region.

If the signal is down converted to the baseband, the matched filter is an impulse at the vibration frequency. The signal component at the vibration frequency for 125 Hz, 250 Hz, and 500 Hz vibration frequencies is calculated using DTFT of the phase response  $k(t)$ . The resultant signal levels at the vibration frequency for 1 W output power are plotted in Figure 4-23.

Looking at Figure 4-23 it is observed that the tumor is best resolved for 125 Hz vibration frequency for which the signal decreases about 2 dB. For 250 Hz and 500 Hz vibration frequencies, it is difficult to make a decision about malignancy as the signal level change is also significant for the case tumor is not present, which is due to inhomogeneity of the tissue and the shear wave effect. For 125 Hz, as the shear wavelength is larger, rather smooth behavior is observed in the absence of the tumor. The decrease in the signal level in the presence of tumor is more significant since the displaced region is larger compared to higher excitation frequencies.

#### 4.5. Conclusions and Discussion

In this chapter, the HMMDI method is analyzed with numerical simulations. An axisymmetrical acoustic solver based on KZK equations is used for finding the acoustic intensity distribution inside the tissue. FDTD method is used for mechanical simulations in order to generate displacement maps inside the tissue due to the acoustic radiation force of the focused ultrasound probe. In mechanical simulations, the tissue is modeled as a linear elastic medium, and it is assumed that the Young's constant and Poisson's ratio are not functions of frequency and the applied force [83]. Also, the thermal effects on the peak value of the displacement are ignored. The intensity distribution obtained in the acoustic simulations is altered to include the attenuation due to tissue inhomogeneity. The displacement results are used as input for the electromagnetic FDTD simulations. The dielectric variation of the tissue due to motion is not taken into account.

The performance of the method is investigated for 125 Hz, 250 Hz, and 500 Hz vibration frequencies. A cubic tumor with 3 mm edge length is introduced in the simulation cases with tumor.

In the homogenous tissue case, the Doppler signal level increases when the focal region moves towards the tumor. The simulations for the homogenous tissue show that the best 3 dB width resolution value is achieved for 125 Hz vibration frequency, which is 2.5 mm laterally and 6 mm axially. The resolution is lower for higher frequencies. This is a result of enlargement in the displaced region volume for the higher frequencies in the presence of tumor. For 125 Hz frequency, the difference in displacement values between the maximum and minimum focal displacement instants are larger in value compared to the higher frequencies.

In simulations for a Class III realistic tissue, it is observed that the Doppler signal level decreases when the focal region is around the tumor. This is caused by the high reflectivity and softness properties of the surrounding fibro-glandular region. It is also observed that the received Doppler signal level varies with the scan position in healthy tissue because of tissue inhomogeneity.

The simulation results are presented for two cases: First one for the Doppler signal level calculated using the first cycle of the vibration; second one for the Doppler signal calculated using the first 4 cycles of the excitation. For the former case if the focus is on the tumor, there is a decrease in signal level and the amount of decrease is affected by the vibration frequency. It is observed that the higher frequencies lead to a higher amount of decrease in the signal level. Therefore, it is better to increase the frequency of vibration for higher resolution. In this case, however, the level of the signal obtained from the normal tissue also decreases as the vibration amplitude decreases. In the latter case, the effect of shear waves leads to abrupt changes in signal level for 250 Hz and 500 Hz frequencies. The position of tumor is recognizable for 125 Hz frequency with a 2 dB decrease in the signal level. The signal level varies rather smoothly for 125 Hz vibration frequency. Since the shear wavelength is larger for the lower vibration frequencies, a low pass filtering effect is observed and the signal level does not change much during a scan. If the focus is on a tumor, due to the small displacement value, the signal level decreases.

For detection of a tumor inside dense inhomogeneous tissue, low vibration frequency provides advantages over high vibration frequencies such as: higher signal level and less influence by the shear waves that lead to higher SNR. High vibration frequencies lead to better discrimination if the system has sufficient SNR for handling single cycle excitation.

Although only 3 vibration frequencies are analyzed for linear scanning in this chapter, the performance of the HMMDI method can be analyzed for other frequencies, and more scan positions to generate images of the realistic tissue models using the developed methods.

## CHAPTER 5

### DEVELOPMENT OF BREAST PHANTOM MATERIALS

#### 5.1. Introduction

Development of phantom materials is essential for experimental investigation of any imaging modality. Phantom materials that mimic the electrical properties of breast tissue are present in the literature [106]-[118]. A review of literature for these types of phantoms can be found in [119]. Similarly, there are a number of publications about breast phantoms for elastography [120]-[124].

The phantom material to be developed for HMMDI method should possess the following characteristics:

- a. It should be stable for a long time.
- b. It must not contain toxic materials.
- c. It should be easy to produce.
- d. It should be able to mimic both dielectric and elastic properties at the same time.

The phantom materials based on oil in gelatin emulsion are found to be the best candidate that can satisfy the criteria above. Oil-in-gelatin emulsion phantoms were firstly used for imitating the ultrasonic properties of the tissue [127]. In 1997, Hall *et. al.* developed phantoms for elastography based on similar materials [120]. These types of phantoms are further investigated in terms of stability for elastography by Madsen *et. al.*[121]. Lazebnik *et.al* proposed using oil in gelatin phantoms for microwave imaging for narrow-band and ultra wideband systems [115]. These types of phantoms are developed successfully for microwave imaging purposes also by other research groups [128] - [131]. The main ingredients for oil in gelatin type elastography and microwave phantoms are gelatin, safflower oil, deionized water, p-toluic acid, n-propanol, formaldehyde, surfactant and kerosene.

As the proportion of the oil is increased in the phantom, the dielectric constant and Young's Modulus decreases. Electrical and mechanical properties are controlled by varying the gelatin/oil ratio. P-toluic acid and n-propanol are used as preservatives. Formaldehyde is used for cross-linking of the gelatin, which facilitates the stability of the phantom. The homogeneity of the emulsion is maintained by the surfactant. Graphites and glass-beads can be added for increasing ultrasound attenuation and scattering.

Electrical and elastic properties of high-adipose content tissues can be emulated using high rates of oil. The tumor can be emulated using a low oil rate since the dielectric and elastic constants of the tumor are high. However, fibro-glandular tissue has high dielectric constant

but low elastic constant. Another control parameter is needed other than oil to gelatin ratio for this type of tissue phantom. It is reported that the elastic constant of the phantom material can be decreased by baking it at 50 °C. The baking period can be several days to several weeks.

Three different types of phantoms (normal breast fat, normal fibro-glandular, tumor) are developed in this study. The amounts of materials for preparing about 1 liter phantom volume (based on [115]) are given in Table 5-1. The surfactant percentage for breast fat is increased for better homogeneity of the phantom material. The fibro-glandular tissue phantom is obtained by baking tumor phantom at 50 °C for 4 days. The dielectric, elastic and ultrasonic properties of the developed phantoms are presented.

Table 5-1: Amounts of materials for preparing 1 liter phantom ( p-tol: p-toluic acid, n-prop: n-propanol, formald.: formaldehyde, surf.: surfactant, gel: gelatine).

<b>Tissue Type</b>	<b>kerosene (ml)</b>	<b>oil (ml)</b>	<b>P- tol. (mg)</b>	<b>n- prop. (ml)</b>	<b>water (ml)</b>	<b>gel. (gr)</b>	<b>formal. (ml)</b>	<b>surf. (ml)</b>
Breast Fat	333	333	167	8.3	158	28.6	1.67	140
Tumor /Fibro- glandular	49.5	49.5	800	39.6	753.5	135	7.9	10.1

## 5.2. Phantom Preparation Procedure

The procedure for phantom preparation is given in [115]:

- (i) P-toluic acid and n-propanol are heated in a small pyrex beaker until p-toluic acid is dissolved.
- (ii) The mixture is poured into a larger beaker that contains de-ionized water.
- (iii) Gelatin is added with stirring to the mixture at room temperature.
- (iv) The top of the beaker is closed by thin plastic film using rubber band, and it is placed in a double boiler.
- (v) The solution is heated until it is nearly transparent (about 90°C).
- (vi) The molten gelatin solution is taken out and stirred. The bubbles on the top are removed.

- (vii) The solution is put inside a water bath and stirred until its temperature is 50°C. Meanwhile, safflower oil and kerosene mixture is heated until 50°C.
- (viii) The oil mixture is added to molten gelatin at 50°C. If the desired oil percentage is higher than 50 %, firstly, required amount for 50 % oil is added and the mixture is stirred until the oil drops are very small. After that the oil mixture is added in small amounts. Every time, the size of the oil drops should be minimized before adding more oil mixture.
- (ix) Using a syringe, surfactant is added to the mixture.
- (x) The mixture is cooled until 40 °C while stirring.
- (xi) Using a syringe and a needle, formaldehyde (37%) added.
- (xii) The mixture is cooled until 34 °C while stirring. It can be poured into the mold at this temperature.
- (xiii) A few days are required for gelatin cross-linking.

### 5.3. Dielectric Properties of the Developed Phantoms

The dielectric properties of the phantoms are measured using the virtual line method [126]. The coaxial probe is placed on the material, and the coaxial line is assumed to be extended inside the material virtually in this method. The dielectric constant of the virtual coaxial line is assumed to be the dielectric constant of the material. Since the radiation loss of the probe can be neglected, the virtual line is terminated with open circuit. The probe model for this method is given in Figure 5-1.

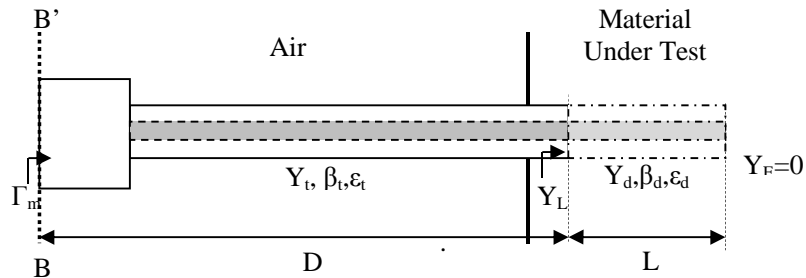


Figure 5-1: Probe model for virtual line method

The variables in the model are given below:



- $Y_d$ : Characteristic admittance of the virtual line.  
 $\epsilon_d$ : Complex dielectric constant of the material under test.  
 $\beta_d$ : Propagation constant of the virtual line.  
 $Y_t$ : Characteristic admittance of the coaxial probe.  
 $\epsilon_t$ : Complex dielectric constant of the dielectric material used in the probe.  
 $\beta_t$ : Propagation constant of the probe  
 $Y_L$ : The admittance at the probe's open end  
 $\Gamma_m$ : The reflection coefficient at B-B' section  
 $D$ : Physical length of the probe  
 $L$ : Length of the virtual line

The admittance at the probe's open end can be written as:

$$Y_L = jY_d \tan(\beta_d L) \quad (5-1)$$

The characteristic admittance of the virtual line is:

$$Y_d = \frac{\sqrt{\epsilon_d}}{60 \ln\left(\frac{b}{a}\right)} \quad (5-2)$$

Relationship between  $\Gamma_m$ ,  $Y_t$  and  $Y_L$  is given as:

$$Y_L = Y_t \frac{1 - \Gamma_m e^{2j\beta_t D}}{1 + \Gamma_m e^{2j\beta_t D}} \quad (5-3)$$

where

$$Y_t = \frac{\sqrt{\epsilon_t}}{60 \ln\left(\frac{b}{a}\right)} \quad (5-4)$$

Inserting (5-3) and (5-1) into (5-2), the complex dielectric constant of the material is given by:

$$\epsilon_d = \frac{-jc\sqrt{\epsilon_t} (1 - \Gamma_m e^{2j\beta_t D})}{2\pi f L (1 + \Gamma_m e^{2j\beta_t D})} \coth\left(\frac{2\pi f L \sqrt{\epsilon_d}}{c}\right) \quad (5-5)$$

where  $c$  is the speed of light,  $f$  is the frequency.

There are two unknowns (D and L) at the right hand side of (5-5). These unknowns can be found by calibration with materials for which the dielectric constant is known (i.e., air, de-ionized water, etc.)

A MATLAB tool is developed for calculating the dielectric constant of the materials measured with the virtual line method. PNA 8364B Network Analyzer is used for the measurements (Figure 5-2). The network analyzer is calibrated using an 85052B calibration kit. An L-shaped semi-rigid cable having 130 mm length is used as the probe. Air and de-ionized water are used for calibration references. Measurements are done in 0.5 GHz- 6GHz frequency band. Time domain gating is applied in order to remove the reflection at the connector.  $S_{11}$  parameter is given in time-domain with and without “gating” in Figure 5-3.



Figure 5-2: Dielectric measurement of the breast fat phantom using network analyzer.

The materials are cut into 3 separate pieces. Measurements are taken from top and bottom of each piece making a total of 6 measurements for each phantom. The mean values for the real and imaginary parts of the relative permittivity are plotted in Figure 5-4. Reference values are also shown for comparison. The dielectric properties of tumor phantoms are very similar to the reference values, whereas the dielectric constant of breast fat phantom is higher than the reference values. The cause of this increase is the addition of extra amount of surfactant for phantom homogenization. The dielectric constant of the fibro-glandular phantoms is similar to the dielectric constant of the tumor phantoms since same amount of materials is used.

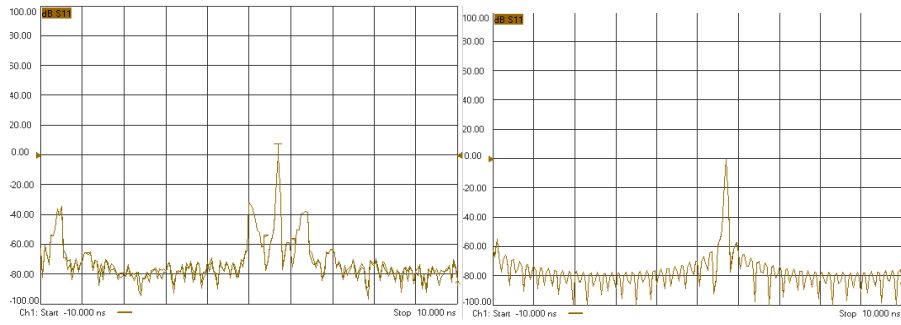


Figure 5-3: Time-domain S11 parameter. Left: without “Gating”, Right: with “Gating”.

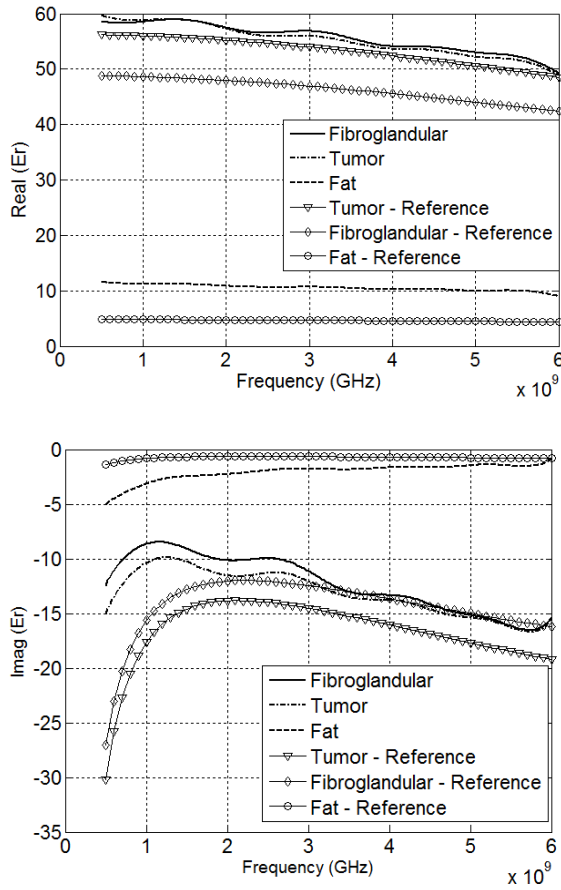


Figure 5-4: Measured relative permittivity of the developed phantoms. Top: Real part ( $\epsilon'$ ), Bottom: Imaginary part ( $\epsilon''$ ).

#### 5.4. Elastic Properties of the Developed Phantoms

The elastic properties of developed phantoms are tested with both dynamic and static measurements. Dynamic measurements are performed using Perkin Elmer Pyris Diamond Dynamic Measurement Analyzer (DMA) in the METU Central Laboratory (Figure 5-5). Cylindrically shaped fat and tumor phantom samples are cut from larger phantoms using a cylindrical hollow tube for the measurements. The diameter and the height of the samples were about 5 mm. Two samples (each from the same batch) were prepared for each type. 15 measurements are taken at 0.1 Hz, 1 Hz, and 10 Hz frequencies. The measurement temperature was 25 °C. The mean values for the storage and loss moduli of the samples are presented in Table 5-2.

The measurement values for the two fat phantoms are different from each other. Therefore, the accuracy of the measurements for the fat phantoms is questionable. The fat phantoms are so soft that measurements may not be performed well using such small samples. However, the measurements for the two tumor phantom samples are similar. In addition, they show good agreement to the values presented in [125]. The results also show that the elastic modulus increases as the frequency increases.

Table 5-2: Measured Storage ( $E'$ ) and loss ( $E''$ ) modulus of the phantom samples (DMA)

Measurement Frequency	Fat - 1		Fat - 2		Tumor - 1		Tumor - 2	
	$E'$ (kPa)	$E''$ (kPa)	$E'$ (kPa)	$E''$ (kPa)	$E'$ (kPa)	$E''$ (kPa)	$E'$ (kPa)	$E''$ (kPa)
<b>0.1 Hz</b>	6.28	4.03	17.71	7.59	77.32	10.82	76.63	12.15
<b>1 Hz</b>	7.62	3.88	25.51	5.59	87.51	14.71	90.86	18.50
<b>10 Hz</b>	12.34	3.51	38.07	11.77	110.52	18.18	118.42	19.53



Figure 5-5: Perkin Elmer Pyris Diamond Dynamic Measurement Analyzer (DMA) in METU Central Laboratory.

Static compression measurements are also performed for the fat, tumor and fibro-glandular phantoms. Lloyd LRX 5K materials testing machine in METU BIOMATEN laboratory (Figure 5-6) is used for obtaining the stress-strain relationship of the phantom material samples with compression test. 100 N load cell is used in the measurements. Samples are prepared in 15 mm diameter falcon tubes. For the measurements, the samples are taken out from the mold and cut in 10 mm height.

The diameter of the compression plate was 60 mm. The measurements are done at room temperature. The initial linear region of the stress-strain curve is used to calculate the Young's moduli of the samples, with the following relation:

$$E = \kappa S \quad (5-6)$$

where  $E$  is the Young's (elastic) modulus,  $S$  is the slope of the stress-strain relation, and  $\kappa$  is a constant. The measured Young's modulus of the tumor phantom at 0.1 Hz frequency is taken as a reference to calculate the constant  $\kappa$ . The results for the two fat phantoms are consistent in this case with a 4.32 kPa average. The measured elasticity values for the developed phantoms and the reference measurement values of the real tissues are presented in Table 5-3.

Elastic moduli of the fat phantoms are similar to the reference value, whereas elastic moduli of the tumor and the fibro-glandular phantoms are higher than the reference values. Fibro-glandular phantom is produced by baking the tumor phantom for 4 days in 50°C oven. For longer baking periods, it was observed that the phantom melts, and its shape is not preserved. In addition, it becomes viscous rather than elastic. Therefore, the produced phantoms are used for experimental studies even though they exhibit higher stiffness than the real tissues. As a result, the phantoms show smaller displacement values for the same amount of mechanical force than the real tissues, which has to be taken into account in assessing the performance of the experimental system.

## 5.5. Ultrasonic Properties of the Phantoms

The ultrasound attenuation and speed of the phantoms are tested in METU Non-Destructive Testing laboratory at 1 MHz and 2 MHz frequencies. Fat and tumor phantom samples with 10 cm. height and 8 cm diameter are used for the tests. The attenuation and speed of the phantoms are measured with tone burst reflection tests. Measured values are presented in Table 5-4.



Figure 5-6: Lloyd LRX 5K materials testing machine in METU BIOMATEN laboratory testing fat phantom sample. The stress-strain relationships of the different phantom types are measured using a 100 N load cell. The samples were 15 mm in diameter and 10 mm in height.

Table 5-3: Measured Young's modulus of the phantom samples (Static compression measurements)

	<b>Fat - 1</b>	<b>Fat - 2</b>	<b>Tumor</b>	<b>Fibro-glandular</b>
Measurements	3.34 kPa	6.07 kPa	76.96 kPa	16.72kPa
Reference	3.25 kPa	3.25 kPa	10.40-42.52 kPa	3.24 kPa

Table 5-4: Measured ultrasonic properties of the phantoms

	<b>Speed of Sound</b>	<b>Attenuation at 1 MHz</b>	<b>Attenuation at 2 MHz</b>
Fat Phantom	1625 m/s	0.36 dB/cm	0.46 dB/cm
Tumor Phantom	1655 m/s	0.49 dB/cm.	0.88 dB/cm

### 5.6. Breast Phantoms for Imaging Setup

Two breast phantoms are prepared to be used in the experimental setup. The first one is a homogeneous fat phantom which includes three different tumor phantoms with different

sizes (Figure 5-7). Diameter x Height values for the tumor phantoms are 3mm x 2.5 mm, 10 mm x 5 mm, and 25 mm x 4.5 mm. The tumors are placed at 30 mm depth from the top surface. The phantom is prepared inside a glass bowl with 11 cm diameter and 5 cm height. It is produced in two stages. At the first stage, the fat phantom is prepared, and poured into the container up to 2.5 cm from the bottom of the mold. The phantom is leaved to solidify for one day. At the second stage, tumor phantoms are placed at the surface of the fat phantom with their centers aligned on a straight line. The places of the tumor phantoms are marked on the cover of the container. In addition, two points are marked on the opposite sides of the container mold, through which the center line of the tumor phantoms passes. After that, fat phantom is prepared and poured on top of the tumor phantoms until the surface level reached 3 cm in height. The phantom is leaved for 7 days at room temperature to solidify.



Figure 5-7: Homogeneous breast phantom including 3 different size tumor phantoms at 30 mm depth. Left: Tumor phantoms used in the breast phantom, Middle: Tumor phantoms placed on the fat phantom at the first stage. Right: Final condition of the breast phantom after the second stage.

The second breast phantom includes a fibro-glandular tissue phantom inside homogeneous fat phantom. A tumor phantom is put inside the fibro-glandular phantom. It is also produced in two stages as in the case for the homogeneous phantom. At the first stage, the fat phantom is prepared, and poured into the container up to 2.5 cm from the bottom of the mold. The phantom is leaved to solidify for one day. The fibro-glandular tissue phantom is prepared inside a falcon tube of 25 mm diameter. After the baking period, 12 mm height portion of it is cut to be used in the breast phantom. A hole is cut, and a tumor phantom of 5 mm diameter and 7 mm height is placed in the bottom of the fibro-glandular phantom (Figure 5-8). The fibro-glandular phantom including the tumor is placed on the center of the fat phantom. Another fat phantom is prepared and poured in the same mold until the surface level reached 3 cm in height. The phantom is leaved for 7 days at room temperature to solidify.

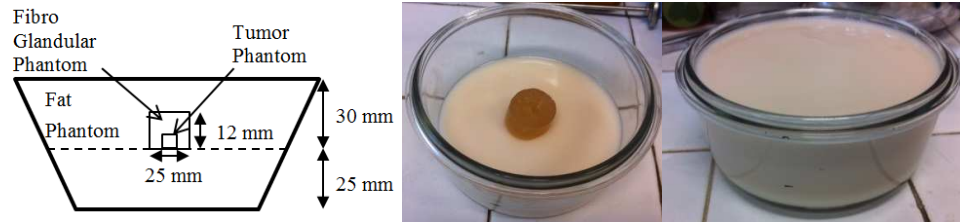


Figure 5-8: Homogeneous breast phantom including tumor phantom inside a fibro-glandular phantom. Left: Phantom geometry, Middle: Fibro-glandular phantom including tumor phantom placed on the fat phantom at the first stage. Right: Final condition of the breast phantom after the second stage.

### 5.7. Conclusion and Discussion

In this chapter, phantom materials that mimic breast tissue properties are developed. The material type is chosen as oil-in-gelatin dispersion as they exhibit excellent properties such as stability, ease of production and mimicking of different tissue types. The dielectric properties are adjusted by varying the oil to gelatin ratio. Elastic properties are adjusted by not only adjusting the oil to gelatin ratio but baking the phantom in 50°C oven, as well. Dielectric, elastic and ultrasonic properties of the phantoms are measured.

The dielectric properties of the phantoms are measured with a virtual line technique using reflection measurements with an open-ended coaxial line. The dielectric properties of the tumor and the fibro-glandular phantoms are consistent with the reference values measured for the real tissues. The permittivity values of the fat phantoms are about 2.5 times larger than the reference values. This is due to the addition of the extra surfactant for making them homogeneous. Otherwise, as the oil percentage is 80 % in the fat phantom, oil is separated from the mixture.

The elastic properties of the phantoms are measured using both dynamic and static compression tests. The reference values present in the literature are measured with 0.1 Hz dynamic tests. The results obtained with the dynamic measurement tests for the tumor phantom were in good agreement with the reference values. Therefore, dynamic measurement results of the tumor phantom are taken as a reference for obtaining the elastic constants of the phantoms. The elastic properties of the fat phantom are consistent with the reference values. However, tumor and fibro-glandular phantoms are stiffer than the reported values. Although baking the phantoms decrease their elastic constant, a long baking period result in a viscous material rather than an elastic one. Therefore, the elastic constant of the fibro-glandular tissue phantom could not be decreased to the elastic constant of the fat phantom.



Ultrasonic properties of the phantoms are also tested using reflection technique. The speed of sound in the phantoms was found to be about 7% higher than the speed of sound in real tissues.

Even though there are some discrepancies between some of the measured properties of the phantoms and the reference values (real tissue measurements), they are not severe. Since they are known, they can be used for predicting the experimental system performance. Two breast phantoms are prepared for the experimental setup: One includes three tumor phantoms with different sizes in homogeneous fat phantom; other includes a fibro-glandular phantom in the homogeneous fat phantom. A small tumor is placed inside the fibro-glandular tissue phantom for the latter case. This case has a special importance since the conventional electromagnetic imaging methods are incapable of detecting the tumor inside the fibro-glandular tissue. It is also problematic to detect the tumor inside dense glandular tissue using mammography. The performance of the HMMDI method is investigated experimentally with the developed phantoms in the next chapter.

## CHAPTER 6

### EXPERIMENTAL STUDY

#### 6.1. Experimental Setup

The performance of the HMMDI method for tumor detection is investigated experimentally using the developed phantom materials. A block diagram of the experimental setup is given in Figure 6.1.

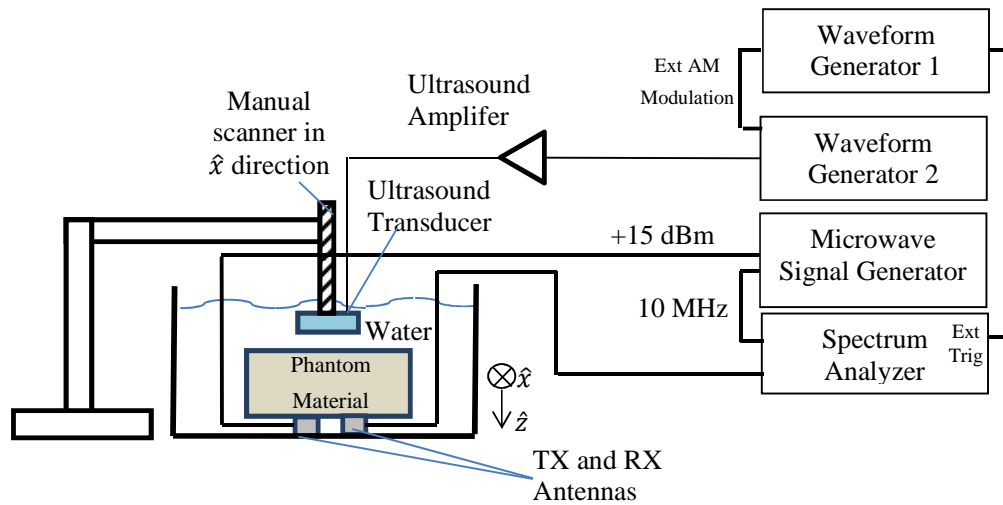


Figure 6-1: Simplified schematic for experimental setup

An amplitude modulated RF signal is generated using two waveform generators. Waveform Generator 1 is used as the modulating signal. A burst signal waveform is used in order not to harm the transducer and the phantom. The generated AM signal is amplified with a high power RF amplifier (Amplifier Research 150A100B) with 52 dB gain. It is fed into a single element focused ultrasound transducer (Sonic Concepts H-102). By this way, vibration is induced inside the phantom material.

A microwave signal generator is used (Agilent E8257C) to feed the transmitting antenna. Spectrum Analyzer (Agilent E4446a) is used for observing the received signal frequency spectrum. It is triggered by Waveform Generator 1 in order to start sweep at the beginning of the burst signal. The properties of the sensors used in the system are given in the next two subsections.

### 6.1.1. Focused Ultrasound Transducer

A single element focused ultrasound (FUS) transducer (Sonic Concepts H-102) is used for generating vibrations inside the tissue. Its properties are given in Table 6-1.

Table 6-1: Properties of the FUS transducer Sonic Concepts H-102

<b>Frequency</b>	1.1 MHz (Fundamental), 3.3 MHz (3 <sup>rd</sup> Harmonic)
<b>Active Diameter</b>	64 mm (Outer) x 22.6 mm (Inner)
<b>Thru Opening</b>	20 mm diameter central opening
<b>Geometric Focus</b>	63.2 mm
<b>Focal Depth</b>	53.5 mm (measured from transducer housing rim to geometric focus)
<b>Power Handling</b>	150 Watts (CW), 400 Watts (Pulsed)
<b>Axial Half Intensity Beamwidth</b>	15 mm (1.1 MHz), 5 mm (3.3 MHz)
<b>Lateral Half Intensity Beamwidth</b>	1.8 mm (1.1 MHz), 0.6 mm (3.3 MHz)

The pressure pattern of the FUS transducer is measured using a needle hydrophone (Onda Corporation, CA, USA) in order to obtain the pressure value for the applied voltage. This is necessary for calculating the applied force in the experiments, and also for using the intensity distribution in the simulations. The measurement is done in the METU ULTRAMEMS laboratory in Electrical and Electronics Engineering Department. The measured axial and lateral pressure beams are plotted in Figure 6-2 for 1 Volt peak to peak excitation of the transducer. The frequency for maximum pressure was measured to be 3.320 MHz.

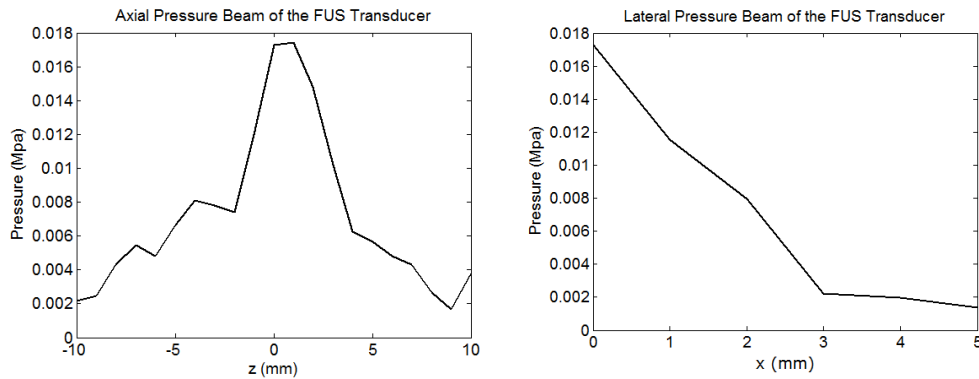


Figure 6-2: The measured beam patterns of the FUS transducer for 1V peak to peak excitation.

### 6.1.2. Antenna Design

Open-ended waveguide antennas are used for transmitting and receiving microwave signals. These types of antennas have advantages such as wide bandwidth, low-loss, and design simplicity. Antennas are placed at the bottom of the phantoms in order not to block the ultrasound transducer that is at the top side. Glass is used as a mold for the breast phantoms. Therefore, there is a 3 mm glass layer between the phantom and the antennas. The antennas are designed in order to work in a wide frequency band from 5 GHz to 8 GHz. The dielectric material used in the antenna is vegetable oil ( $\epsilon_r \approx 2.5$ ,  $\sigma=0.05$  [132]). Broad-wall and narrow-wall dimensions of the waveguide are chosen to be 22.86 mm and 10.16 mm. The cut-off frequency for  $TE_{10}$  mode is 4.07 GHz for this choice of dimensions. The next propagating mode is  $TE_{20}$  which has the cut-off frequency of 8.1 GHz. The antenna is fed using a coaxial probe having the dimensions of a standard SMA adapter (inner conductor radius: 0.69 mm, outer conductor radius: 2.3 mm). The dielectric material in the coaxial adapter is Teflon™ with relative permittivity 2.1, and dielectric loss tangent 0.001. Antenna is modeled in Ansys HFSS (Ansys, Inc., PA, USA). It is placed at the bottom of the glass bowl for matching using the parameters  $p$ ,  $d$ , and  $h$  (Figure 6-3).  $p$  is the length of the inner conductor inside the waveguide.  $d$  is the distance between the center point of coaxial probe to the short circuit.  $h$  is the total length of the antenna. The convergence parameter (maximum magnitude of delta S) is chosen to be 0.005 in the simulations. The optimized values for a -10dB bandwidth of 50 % are  $d=8\text{mm}$ ,  $p=5.6\text{ mm}$ , and  $h=15\text{mm}$ .

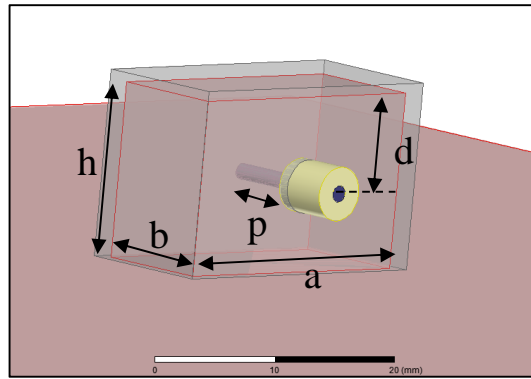


Figure 6-3: Antenna HFSS model. The design parameters are shown on the figure.

The housing of the antenna is produced using aluminum material in the ASELSAN REWIS Machine Shop. Oil is prepared and poured into the antenna and the opening is closed using a plastic material. The plastic is fixed to the aluminum using a waterproof adhesive. The antennas are placed on the bottom of the phantoms and the S-parameters are measured using Agilent 8722 D network Analyzer. The measured and the simulated S11 parameter are shown in Figure 6-4. There is a shift in the measured frequency band of the antenna to the lower frequency. The reason of this shift is the difference between the real dielectric

parameter of the safflower oil and the simulated value. Nevertheless, the antenna exhibits a return loss better than 10 dB in the desired frequency range.

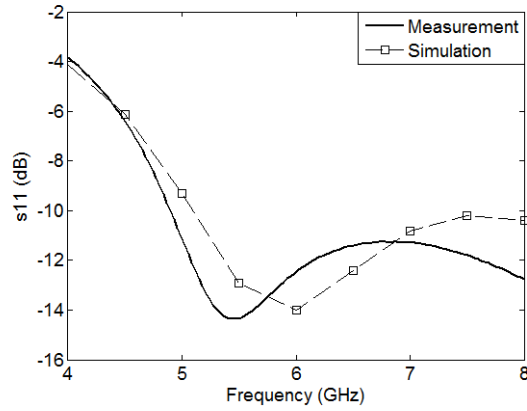


Figure 6-4: Measured and simulated  $S_{11}$  parameter of the antenna.

### 6.1.3. Phase Noise of the Transmitter

The phase noise of the transmitter is an important parameter since the Doppler frequency is very close to the carrier frequency. The phase noise of the signal generator is measured by directly connecting the Signal Generator output to the Spectrum Analyzer for 0 dBm output power (Figure 6-5). 10 MHz reference signal of the Spectrum Analyzer is used as 10 MHz reference for the Signal Generator. The spectrum analyzer parameters for the phase noise measurement are: Resolution bandwidth = 6.8Hz, Span =500Hz, Averaging = 20.

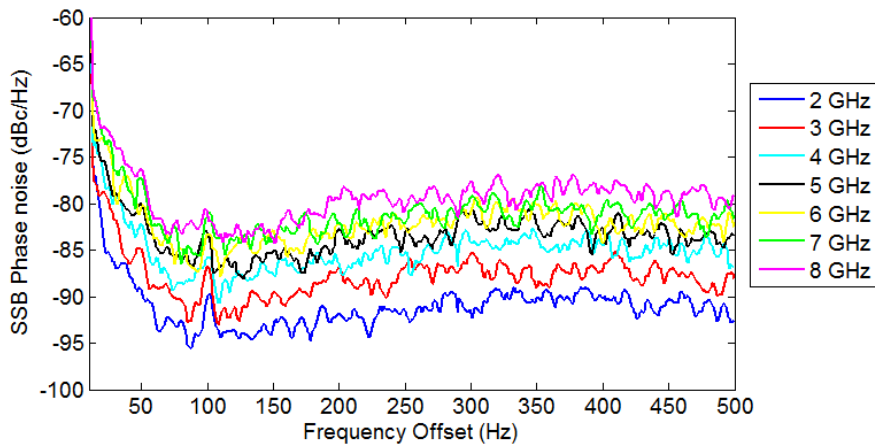


Figure 6-5: Directly measured phase noise characteristic of the Signal Generator for 500 Hz frequency span.

## 6.2. Measurements for the Phantom-1

Phantom-1 contains a fibro-glandular phantom with 25 mm diameter and 12 mm height inside the fat phantom (Figure 6-6). A tumor phantom with 5 mm diameter and 7 mm height is present in the middle of the fibro-glandular phantom.



Figure 6-6: Phantom-1 before the second fat layer is poured.

The configuration for the measurements is given in Figure 6-7. The height of the FUS transducer is adjusted so that its focus is at 30 mm depth. The antennas are placed in H-plane configuration with 15 mm distance between their edges. The antennas are placed on the bottom side in order not to obstruct the FUS transducer that is scanned on the top side. Since the bottom of the glass container is not planar, a piece of rubber is placed between the antennas and the glass. The antennas are placed 15 mm away from each other. The transmitting antenna is fed by the Signal Generator. The output power of the Signal Generator is 15 dBm. The receiving antenna output is connected to the Spectrum Analyzer.

### 6.2.1. Microwave Frequency Analysis

Prior to the mechanical scan, the microwave operating frequency is chosen first. The FUS transducer is fed with  $367 V_{pp}$  voltage, which corresponds to 6.4 MPa peak pressure at the focus (Figure 6-8). Vibration frequency is selected to be 15 Hz, which showed a good SNR value. The Doppler response for higher frequencies than 30 Hz was masked by the coupled phase noise of the oscillator. For vibration frequencies lower than 10 Hz, the Doppler response was not resolvable from the main frequency component. An AM burst with 3 cycles is sent with 1 second repetition intervals. The focus of the FUS probe is positioned at the fibro-glandular phantom. Averaging the short-time intensity (2-3), spatial peak pulse average intensity  $I_{sppa}$  of the ultrasound beam is  $630.2 \text{ W/cm}^2$  in this case. For 3 cycles of excitation, duration is 200 ms.

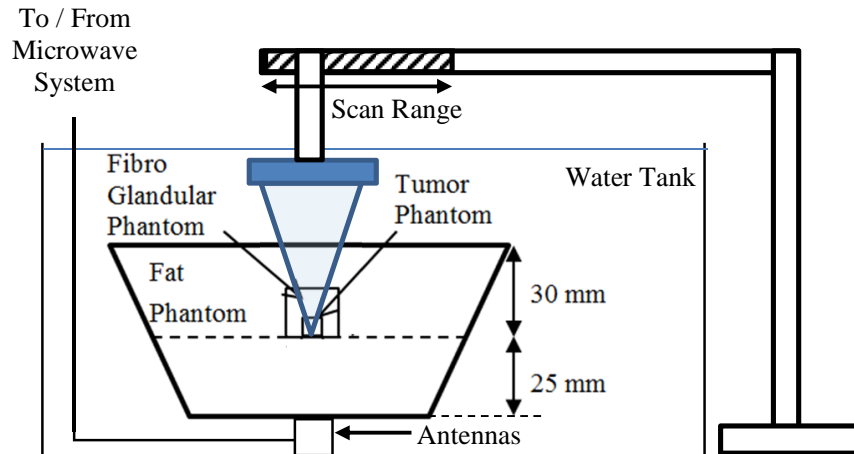


Figure 6-7: Setup configuration for the Phantom-1 measurements

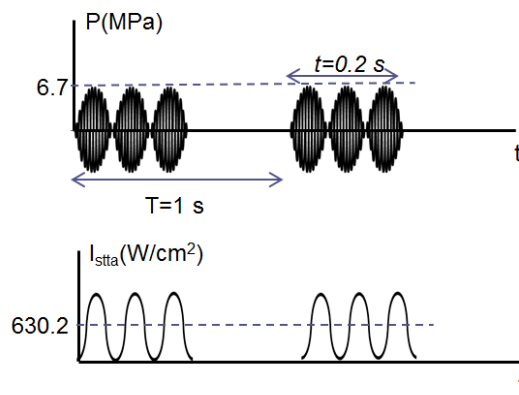


Figure 6-8: Pressure and intensity at the focus of the ultrasound probe for microwave frequency analysis. Amplitude modulated pressure is applied as a burst of 3 cycles.

The following parameters are used in the microwave measurements: Resolution bandwidth = 6.8Hz, Span =200Hz, Sweep Time =280 ms, Averaging = 20. The main frequency and the Doppler frequency components of the received microwave signal are measured along with the noise value at the Doppler frequency component (Figure 6-9).

Figure 6-10 (a) shows that the SNR is above 20 dB from 2 to 6 GHz. The Doppler component to main frequency component is highest for 6 GHz frequency (Figure 6-10 (b)). This is a result of cancellation of the coupled signal components from water/glass interface and glass/phantom interface at this frequency.

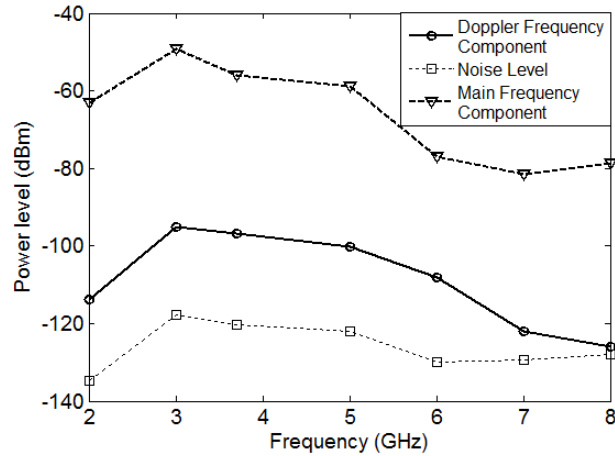


Figure 6-9: Received signal and noise levels as a function of frequency when the focus is on the fibro-glandular phantom. 15 Hz vibration with 3 cycles is applied with 1 second PRI. Peak pressure is 6.7 MPa.

This effect is investigated with HFSS simulations. The simulation geometry is shown in Figure 6-11. S21 parameter is calculated for no spacer, 1 mm rubber layer spacer, and 1 mm water layer spacer cases. Similar to the experimental setup, the antennas are 15 mm away from each other in the simulation geometry. Background is water. The dielectric properties used in the simulation are: Glass (Ansys HFSS):  $\epsilon_r=5.5$ ,  $\sigma=0$  S/m, rubber (Ansys HFSS):  $\epsilon_r=3$ ,  $\sigma=10^{-15}$  S/m, water:  $\epsilon_r=77$ ,  $\sigma=4.406$  S/m, Fat phantom:  $\epsilon_r=10$ ,  $\sigma=0.41$  S/m, oil [132]:  $\epsilon_r=2.5$ ,  $\sigma=0.05$  S/m.

The simulation and the measurement values for S21 parameter are plotted as a function of frequency in Figure 6-12. The coupled power decreases when the rubber layer is present. It is further decreased if water is present between the antennas and the glass due to the attenuation of the waves in water and reflection at the antenna aperture. The simulated values for the S11 parameter are shown in Figure 6-13 for different configurations. It is observed that when there is a rubber spacer between the antennas and the glass, the decrease in coupling is due to the attenuation of the waves inside the water between the antennas. If water is present between the antennas and the glass, the reflection at the antenna aperture is high because of the high dielectric contrast between water and oil. Therefore, coupling is decreased further. In order to observe the relative power transmitted to the phantom for both cases, a test antenna is placed on the phantom. The coupled signal from the transmitting antenna to the test antenna is plotted in Figure 6-14.



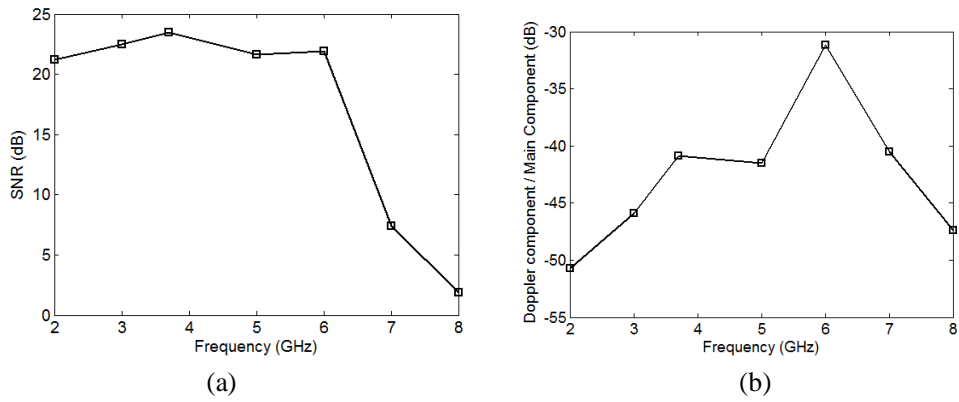


Figure 6-10: (a) SNR, and (b) Doppler component to main frequency component. 15 Hz vibration with 3 cycles is applied with 1 second PRI. Peak pressure is 6.7 MPa.

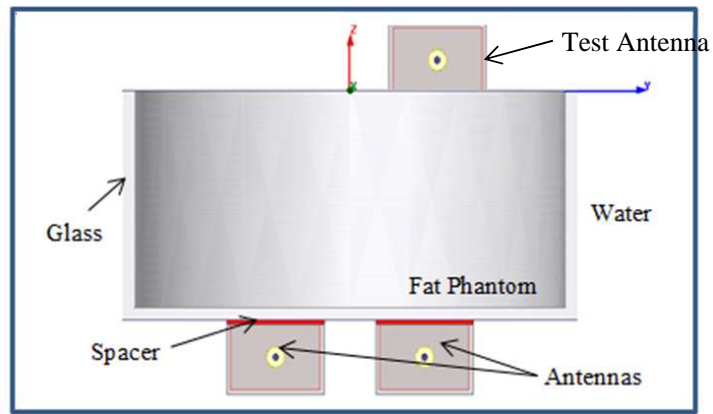


Figure 6-11: Ansys HFSS simulation geometry for coupling analyses. The antennas are placed at the bottom of the phantom. There is a 1 mm space between the aperture of the antennas and the glass. A third test antenna is placed on top of the phantom in order to observe the change in power transmitted to the phantom.

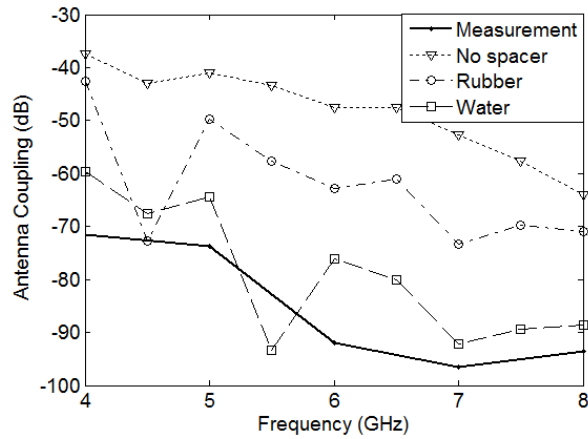


Figure 6-12: Simulated and measured antenna coupling values.

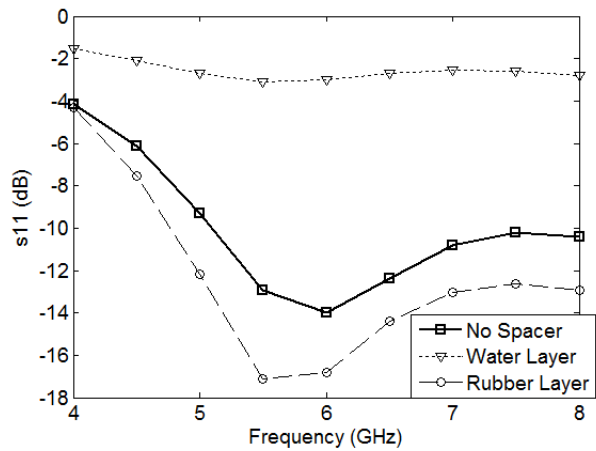


Figure 6-13: Simulated S11 parameter of the antennas

When rubber layer is present between the antennas and the glass, the coupled signal to the test antenna does not decrease more than 2 dB. However, if water leaks between the antennas and the glass, the transmitted power to the phantom can decrease more than 12 dB. The presence of water between the transmitting and the receiving antennas is desirable in the sense that the direct coupled signal decreases. However, the antenna/glass interface must be free of water in order to match the antennas to the phantom. The coupled signal level in the measurements is lower than the simulated value for 1 mm water layer between the antennas and the glass. This shows that water is leaked into the rubber layer. In addition, the water layer thickness between the antenna aperture and the glass is thicker than 1 mm.

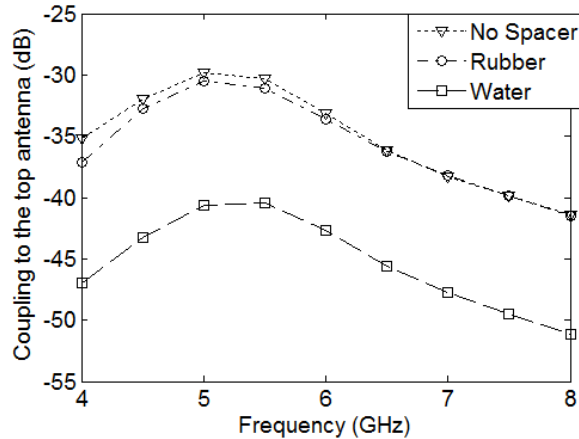


Figure 6-14: Coupled signal from the transmitting antenna to the test antenna.

It is observed that the coupled signal level is very low at some frequency point (Figure 6-12). For rubber layer this frequency point is 4.5 GHz, whereas for water layer it is 5.5 GHz. The transmitted power to the phantom is not decreased for these frequencies (Figure 6-14). Therefore, it can be concluded that there is a cancellation mechanism for the directly coupled signal, which results in a low coupling at a certain frequency. This effect also leads to an increase in the scattered signal to direct coupled signal ratio at 6 GHz in the measurements (Figure 6-10 (b)).

### 6.2.2. Linear Scan Results

Since the Doppler component to the main frequency component is highest at 6 GHz frequency, the operation frequency for the linear scan is chosen as 6 GHz. The manual scanner has a 31 mm scan range. The scan is performed for 54 mm range in 1 mm steps with two positions of the holder. 9 mm of the scan range for two scans are coincident. The FUS probe and the phantom during the scan are shown in Figure 6-15. The scan lines, boundaries of the fibro-glandular and tumor phantoms, and the antenna positions are shown in Figure 6-16.

The same waveform used in the microwave frequency analysis section is used for scanning along the phantom. However, in this case the measurements are performed with 4.2 MPa peak pressure at the focus in order to work closer to the safety limits.  $I_{sppa}$  of the ultrasound beam is 271.4 W/cm<sup>2</sup>. The SNR was not sufficient for lower ultrasound intensity values in the presented setup. If this amount of energy were applied to the real fibro-glandular tissue, the temperature rise would be 4.23 °C, neglecting convection and conduction of heat. Also, the mechanical index is calculated to be 2.3. Although these values are above safety limits, there are a number of differences in the phantom experiment than real tissue case that leads to higher intensity requirement for phantom experiments. Firstly, the elastic constants of the fibro-glandular tissue and tumor phantoms are higher than the real tissues. Secondly, the dielectric contrast between the fat phantom and the fibro-glandular or tumor phantom is lower than the real scenario. Thirdly, a better transmitter and with lower phase noise can be

used together with a sensitive receiver that would require lower ultrasound power. In addition, the antenna apertures were not sealed, and there was an uncontrolled water leakage between the antennas and glass.

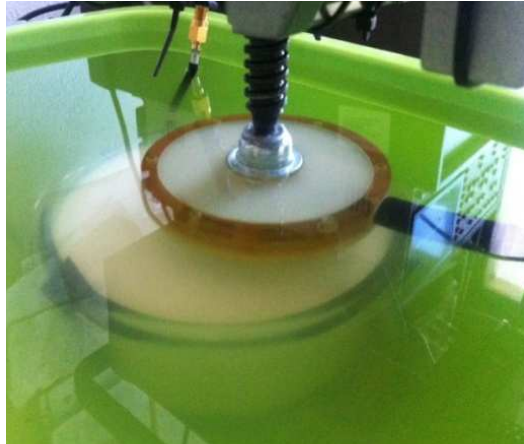


Figure 6-15: FUS probe scanning on the breast phantom

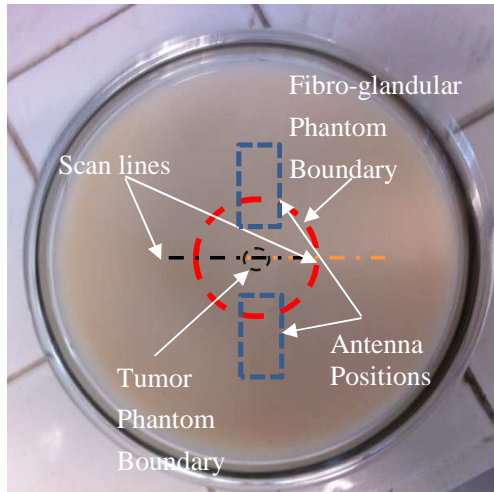


Figure 6-16: Scan line 1 (black) and 2 (orange) for the heterogeneous tissue phantom.

Microwave exposure is not an issue for safety since the applied microwave power is 15 dB, which is lower than the sample case given in Section 2.8.7. The measurements are affected by thermal noise rather than phase noise since the direct coupling is low. The microwave power could be even higher using an amplifier, which would decrease the requirement for ultrasound power and duration.

Simulations are also performed for the same configuration using the measured values of the ultrasound probe intensity, and the measured ultrasonic, elastic and electrical parameters of the phantom materials. The method given in Chapter 3 is used for the simulations. The geometry for the electromagnetic simulation is given in Figure 6-15. The tumor phantom is modeled as a rectangular prism with 5mm x 5mm x 7mm dimensions. The fibro-glandular phantom is also modeled as a rectangular prism with 28 mm x 28 mm x 12 mm dimensions. Antennas are put inside the water as in the case in the measurement setup. A water layer of 1 mm thickness was assumed to be present between the antenna apertures and the glass mold. 1mm<sup>3</sup> mesh size is used. The problem geometry is terminated with Perfectly Matched Layers in all dimensions.

The measurement results are presented in Figure 6-18 along with the simulation results. The positions of the tumor and the fibro-glandular tissue phantom are represented with red and yellow colors in the figure, respectively. The signal level is low when the focus is on fat phantom. It increases as the focus gets closer to the fibro-glandular phantom and decreases about 3 to 6 dB when the focus is on the tumor. The signal plot is not symmetrical since the fibro-glandular phantom is not symmetric (Figure 6-6). The simulated values were found 8 dB higher than the measurement values, and normalized in the plot for comparison. This results show that the water layer is thicker than the simulated case in the measurement setup. Nevertheless, there is a good agreement between the signal characteristics of the simulated and the measured values. The discrepancy in the outer region is due the assumptions made in the simulations. The fibro-glandular phantom is not standing straight; it is rather inclined (Figure 6-6). In addition, the effect of dielectric perturbation in fat phantom due to vibration is not taken into account in the simulations.

The results show that a small tumor inside the fibro-glandular tissue is detectable with the presented HMMDI method. When the focus is on the fat phantom, the Doppler signal is higher than the noise level due to the density variation caused by the motion. It may be discriminated using a different vibration frequency and comparing the changes in signal level for tumor and fat phantoms.

The scan range of the manual scanner is increased to 40 mm and another linear scan is performed for the same phantom with a single scan (Figure 6-19). The measured results are plotted in Figure 6-20 together with the simulated values. This time the simulation results are decreased 6 dB for normalization, which shows that a better coupling to the phantom is achieved in the measurements. The results are in good agreement with the simulations.

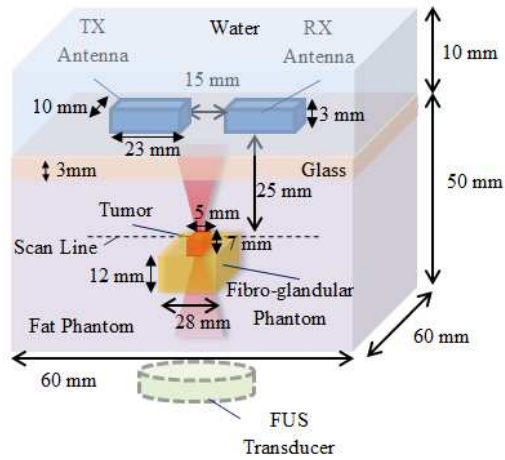


Figure 6-17: Simulation geometry for the linear scan measurements of Phantom-1.

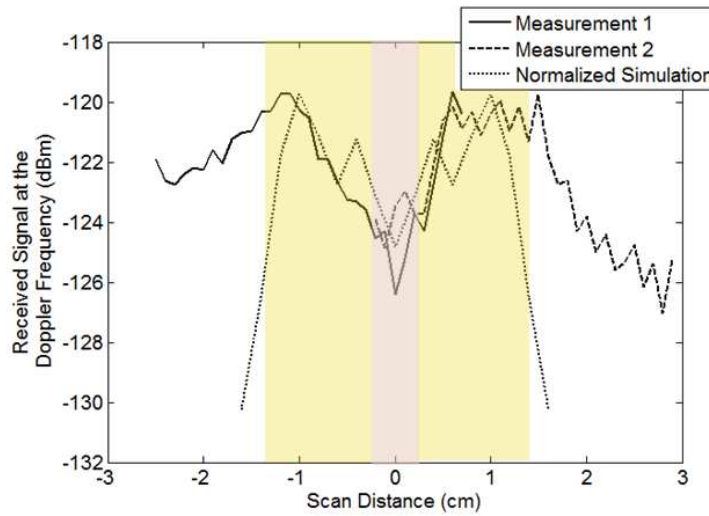


Figure 6-18: Measured and simulated signal level at the Doppler frequency for the linear scan across the fibro-glandular phantom, which contains tumor in the middle. The places of the tumor (red) and the fibro-glandular (yellow) phantoms are depicted in the figure.

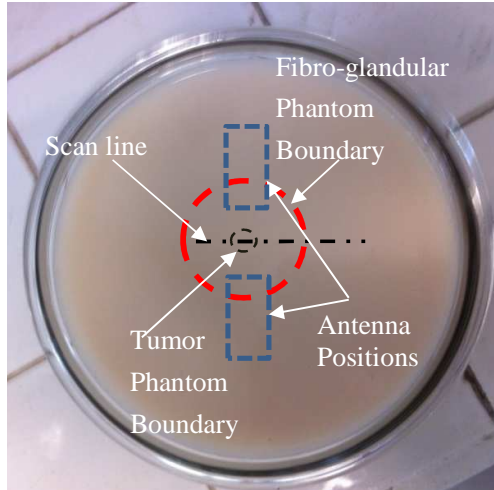


Figure 6-19: Scan line for the single 40 mm linear scan case for Phantom 1.

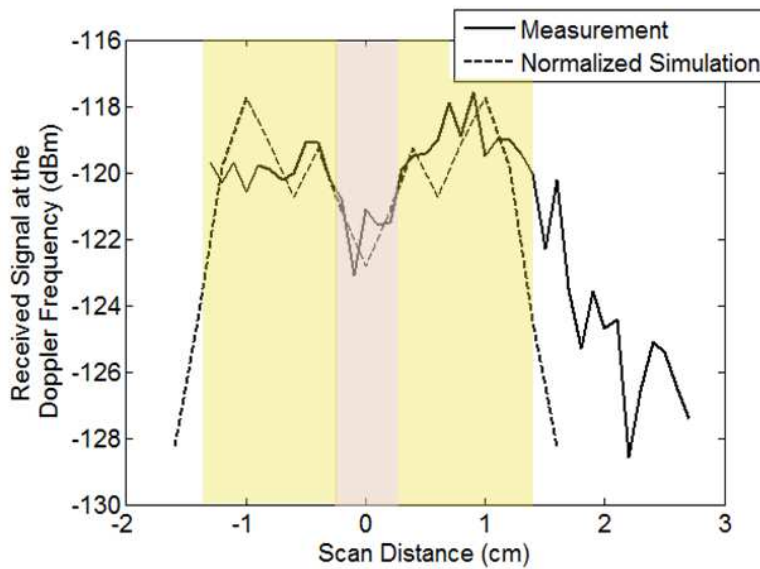


Figure 6-20: Measured signal level at the Doppler frequency for the 40 mm linear scan across the fibro-glandular phantom, which contains tumor in the middle. The places of the tumor (red) and the fibro-glandular (yellow) phantoms are depicted in the figure.

### 6.3. Measurements with Phantom-2

In Phantom-2, there are three different tumor phantoms inside the fat phantom (Figure 6-21). The biggest is 25 mm in diameter and 4.5 mm in height. The middle sized is 10mm in diameter and 5 mm in height. The smallest one is 3 mm in diameter and 2.5 mm in height.

The value of peak pressure was increased to 7.5 MPa in order to discriminate highly hard tumor phantom inside the fat phantom.  $I_{SPPA}$  of the ultrasound beam is  $865.4 \text{ W/cm}^2$ .



Figure 6-21: Phantom-2 before the second fat layer is poured.

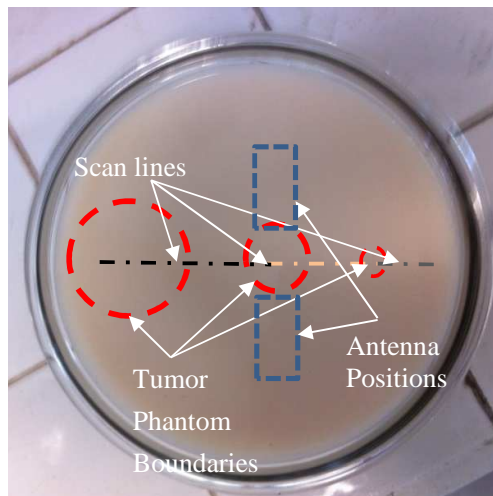


Figure 6-22: Scan line 1 (black), 2 (orange), and 3 (gray) for Phantom-2.

Three scans are performed to cover 78 mm linear scan range with 1 mm steps. Measurement is done in 3.7 GHz microwave frequency with +16 dBm output power from the signal generator. 30 Hz vibration frequency is applied. In this case, only the response from different sizes of tumor phantoms inside the fat phantom is considered. The frequency values are not optimized for the best SNR.



The measurement results show that the small and middle sized tumor phantoms can be identified. However, the amplitude of the displacement for the big sized tumor is not sufficient to increase the Doppler component.

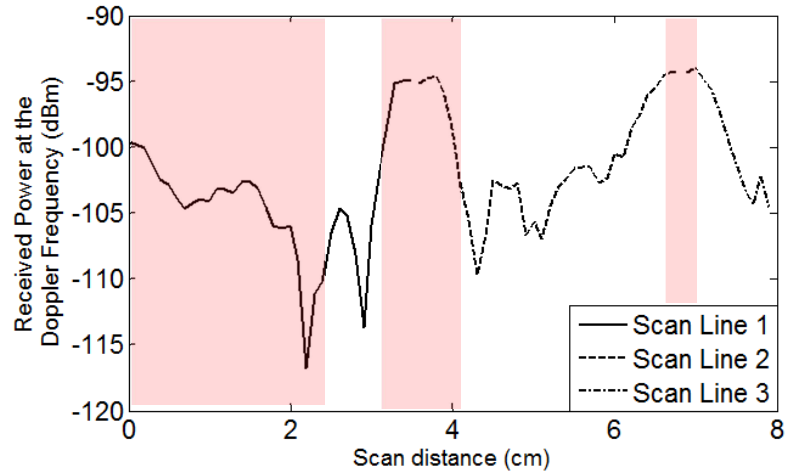


Figure 6-23: Measured signal level at the Doppler frequency for the linear scan across the heterogeneous breast phantom, which contains 3 different tumors. The places of tumors are depicted in red color.

#### 6.4. Conclusions and Discussions

In this chapter, the proof of concept for the HMMDI method is demonstrated on the phantom materials. The phantom materials are vibrated locally using a FUS probe. Microwave signals are transmitted to the phantom during ultrasound excitation. The amplitude of the received signal at the Doppler (vibration) frequency signal is sensed using a Spectrum Analyzer. Using a linear manual scanner, the focus of the FUS probe is scanned on a line at 30 mm depth inside the phantom. From the bottom (antenna) side, the depth of the scan line is 25 mm.

For the breast phantom including tumor inside fibro-glandular phantom, the results show that the received signal level increases when the focus is on fibro-glandular phantom and decreases when it is on tumor phantom. This result is important in the sense that it shows it is possible to distinguish tumor inside fibro-glandular tissue using HMMDI method. A 5 mm diameter tumor at 25 mm depth was resolved in the experiments. Because of the fluctuation of dielectric constant due to vibration, a significant response from the fat phantom is also received. Therefore, during a scan, a means for distinguishing the fat response from the tumor response is necessary. Measurements with multiple vibration frequencies may be a solution for this problem. 15 Hz vibration frequency is used in this study. For higher vibration frequencies, the amplitude of the vibration for the same amount of ultrasound

pressure is low. Therefore, the Doppler frequency component was not resolved in noise. The applied ultrasound intensity was  $I_{sppa} = 271.4 \text{ W/cm}^2$ , which is slightly above the safety limits. The ultrasound power is not increased in order not to harm the phantom. Some aspects of the experimental system, which required high amount of ultrasound intensity level, should be noted. The transmitter and receiver used in this study are general measurement devices. Using a transmitter with lower phase noise, a receiver with a processor that measures the Doppler component with a matched filter, better results for higher vibration frequencies can be obtained. In addition, the elastic constants of fibro-glandular and tumor phantoms are higher than the real tissue reference values. The dielectric contrast between the fat and tumor/fibro-glandular phantoms is also lower than the reference values. Therefore, a better performance is expected for experiments with breast tissue rather than phantoms. Also, the antenna coupling to the phantom can be improved by using a coupling liquid that enables better coupling to the tissue and at the same time provides high isolation between the transmitting and the receiving antennas. The isolation between the antennas should be made as high as possible in order to avoid leakage phase noise of the transmitter. It was observed that when there are two layers between the antennas and the phantom, the directly coupled signal decreases drastically for some frequency point. This property can be used in the system design, which will increase the performance of the system.

Although normalization was necessary due to the differences between the experimental setup and the simulation geometry, the simulation results were quite similar to the measurements. The main difference that led to lower received power level in the measurements is the thickness of the water layer between the antenna aperture and the phantom.

For the homogenous breast phantom with tumor inclusions, a higher ultrasound power level ( $I_{sppa} = 865.4 \text{ W/cm}^2$ ) was required since the elastic constant of the tumor phantom is high. For a 3 mm diameter tumor, the width that the signal decreased 3 dB from the peak was 8 mm. A sharper decrease was observed for 10 mm diameter tumor for which the 3dB width was 5 mm. The smaller tumor has a lower inertial mass. Therefore, the signal level is high for a larger lateral separation between the tumor and the focal point. On the other hand, the larger tumor vibrates when the focus is just on it, yielding a better resolution. Although there is an increase in the signal level, the vibration response of the biggest tumor could not be resolved well since the vibration amplitude is small.

To conclude, it is shown with phantom experiments that the proposed method can be used for detecting small tumors in highly dense breast tissues. In fact, it is better to image a dense tissue rather than a fatty tissue with HMMDI method as the Doppler component will be higher.

## CHAPTER 7

### CONCLUSIONS AND FUTURE WORK

In this thesis, the potential of a novel method, namely Harmonic Motion Microwave Doppler Imaging (HMMDI), for detection of breast tumors in the early stage was presented. The method makes use of the contrast in electrical and elastic properties of the malignant and healthy tissues for tumor detection. It can also be used for detecting tumors in the other tissues that are penetrable by ultrasound and microwaves.

The method involves generation of local harmonic motion inside the tissue. This motion can be generated using radiation force of ultrasound. Microwave signals are transmitted and received using antennas that are matched to the tissue. Phase modulation is introduced on the received signal due to vibration. The first spectral frequency component, namely the Doppler component, of the received signal is sensed, which depends on the elastic and electrical characteristics of the tissue.

The advantages of this method can be listed as follows:

- 1) Potential of detecting tumors inside fibro-glandular tissue:  
Since the tumors are stiffer than the healthy tissues, they can be detectable inside the fibro-glandular tissue with a reduction in the signal level.
- 2) Utilization of microwaves rather than ultrasound:  
In remote palpation methods such as Harmonic Motion Imaging (HMI) or Acoustic Radiation Force Imaging (ARFI), the elasticity of the tissue is reconstructed using a diagnostic ultrasound transducer. The attenuation of ultrasound waves in fibro-glandular tissue is about 11 dB/cm at 7.5 MHz, which is a typical frequency. On the other hand, attenuation of microwaves at 3 GHz is about 5 dB/cm. Therefore, better penetration depth is achievable using microwaves. In addition, the method can be combined with microwave imaging and dielectric and elastic properties can be reconstructed at the same time yielding better sensitivity and specificity.
- 3) Millimetric resolution:  
The resolution is on the order of millimeters due to the usage localized vibration, without the need for ultrawideband microwave components.

4) Simpler reconstruction due to focused US:

Since the vibration is localized due to the usage of focused ultrasound, complex reconstruction algorithms are not needed.

5) Non-invasive, patient friendly method suitable for mass screening :

Since ionizing radiation is not used, the proposed method is harmless and can be used without any limitations. The compression of the breast is not necessary. Therefore, it is a patient friendly method and has a potential for mass screening usage.

A semi-analytical solution procedure is given for analyzing the feasibility of the method for simple two layered breast model. Numerical FDTD simulators for both mechanical and electromagnetic problems are developed. For calculating the scattered field from a vibrating region inside the tissue, a new accurate 3-D FDTD approach is introduced. A solution procedure for numerical simulations of the forward problem is proposed. The procedure involves the simulations of the acoustic, mechanical and electromagnetic problems sequentially.

The simulation results show that as the frequency increases, the region of vibration gets smaller. Therefore, higher resolution can be achieved. It was also shown that if there is a tumor inside the tissue, the signal level drops down when the focus of the ultrasound probe passes through the tumor. The decrease in the signal level is greater for higher frequency of vibration, if only the first cycle of excitation is considered. Consequently, the discrimination performance is better. However, SNR decreases as the vibration frequency increases since the vibration amplitude decreases. If the excitation is longer than one cycle, the shear waves are propagated into the tissue, and the received signal is affected from the regions outside the focus. The response from a 3 mm edge cubic tumor was still distinguishable with a 2 dB signal decrease for 125 Hz vibration frequency with 4 cycles of vibration.

Breast phantom materials that mimic the electrical, elastic and ultrasonic properties of the breast tissue are developed to be used in experimental studies on the method. The dielectric properties of the tumor and fibro-glandular phantoms were similar to the reference values whereas the dielectric constant of fat phantom was about 2.5 times higher than the reference. On the contrary, for elasticity, the fat phantom properties were similar to the reference values where tumor and fibro-glandular phantoms yield higher elasticity values.

The experiments with general purpose instruments showed that a small tumor phantom at 25 mm depth with 5 mm diameter and 7 mm height is detectable inside fibro-glandular tissue for 15 Hz vibration frequency. A 3 to 6 dB decrease in signal level was observed on the tumor region compared to the signal level gained on the fibro-glandular phantom. Better performance is expected if specialized microwave architectures are used together with signal processing techniques.

This thesis is an initial work on the HMMDI method for which the feasibility is investigated for early stage breast cancer detection. As a consequence, there are numerous points that should be investigated further in the future. Some of them are listed below:

- 1) Development of fast and efficient numerical tools for the forward problem solution,
- 2) Adding the effect of dielectric perturbation due to motion in the electromagnetic simulator,
- 3) Conducting simulations on various realistic tissue geometries for different tumor sizes and depths,
- 4) Analyzing the performance and usability of the method for detection of tumors in other organs such as prostate, kidney, and liver,
- 5) Improving phantom materials to construct more realistic phantoms,
- 6) 3-D scanning on phantom materials,
- 7) Designing and implementing a specialized microwave transceiver system to be used in the experiments,
- 8) Improving the antenna and coupling medium design for high isolation and better coupling to the tissue,
- 9) Multi-vibration frequency data acquisition to improve fat/tumor discrimination,
- 10) Building a clinical prototype system for imaging,
- 11) Acquiring and processing 3D image data from phantom materials/ animals /patients,
- 12) Data fusion with microwave imaging,
- 13) Developing reconstruction algorithms for elasticity and dielectric variation inside the tissue,

## REFERENCES

- [1] Worldwide Breast Cancer, "Breast cancer statistics worldwide," <http://www.worldwidebreastcancer.com/learn/breast-cancer-statistics-worldwide/>, Date of last access: 03 Sep. 2013.
- [2] P. T. Huynh, A. M. Jarolimek, and S. Daye, "The false-negative mammogram," *Radiograph*, vol. 18, no. 5, pp. 1137–1154, 1998.
- [3] J. G. Elmore, M. B. Barton, V. M. Moceris, S. Polk, P. J. Arena, and S. W. Fletcher, "Ten-year risk of false positive screening mammograms and clinical breast examinations," *New Eng. J. Med.*, vol. 338, no. 16, pp. 1089–1096, 1998.
- [4] R. P. Burns, "Image guided breast biopsy," *Am. J. Surg.*, vol. 73, pp. 9–11, 1997.
- [5] Y. Zou and Z. Guo, "A review of electrical impedance techniques for breast cancer detection," *Medical Engineering & Physics*, vol. 25, pp. 79–90, 2003.
- [6] P. P. Tarjan and R. McFee, "Electrodeless Measurements of the Effective Resistivity of the Human Torso and Head by Magnetic Induction," *IEEE Tran. Biomed. Eng.*, vol. 15, no. 4, Oct. 1968.
- [7] N. G. Gencer and M. N. Tek, "Electrical conductivity imaging via contactless measurements," *IEEE Transactions on Medical Imaging*, vol. 18, pp. 617-627, July 1999.
- [8] A. Korjenevsky, V. Cherepenin, and S. Sapetsky, "Magnetic induction tomography: Experimental realization," *Physiol. Meas.*, vol. 21, pp. 89-94, 2000.
- [9] H. Scharfetter, H. Lackner, and J. Rosell, "Magnetic induction tomography: Hardware for multi-frequency measurements in biological tissues," *Physiol. Meas.*, vol. 22, pp. 131-146, 2001.
- [10] B. U. Karbeyaz, N. Gencer, "Electrical Conductivity Imaging via Contactless Measurements: An Experimental Study," *IEEE Tran. Bmed. Eng.*, vol. 22, no 5, May 2003.
- [11] H. Wen, J. Shah, and S. Balaban, "Hall effect imaging," *IEEE Trans. Biomed.Eng.*, vol. 45, no. 1, pp.119-124, 1998.
- [12] H. Wen, "Feasibility of biomedical applications of hall effect imaging," *Ultrason. Imag.*, vol. 22, pp.123-136, 2000.
- [13] H. Wen, "Volumetric hall effect tomography – a feasibility study," *Ultrason. Imag.*, vol. 21, pp.186-200, 1999.

- [14] A. Montalibet, J. Jossinet, A. Matias, "Scanning electric conductivity gradients with ultrasonically-induced Lorentz force". *Ultrason. Imag.* vol. 2., no.1, pp.32,2001.
- [15] H. Zhang and L. V. Wang, "Acousto-electric tomography", *Proc. SPIE* 5320, 145, 2004.
- [16] Y. Xu and B. He, "Magnetoacoustic tomography with magnetic induction," *Phys. Med. Biol.*, vol. 50, pp. 5175-5187, 2005.
- [17] X. Li, Y. Xu, and B. He, "Imaging electrical impedance from acoustic measurements by means of magnetoacoustic tomography with magnetic induction (MAT-MI)," *IEEE Trans. Biomed. Eng.*, vol. 54, pp. 323-330, Feb. 2007.
- [18] R. Xia, X. Li, and B. He, "Magnetoacoustic tomographic imaging of electrical impedance with magnetic induction," *Appl. Phys. Lett.*, vol. 91, 083903, 2007.
- [19] Y. Xu, S. Haider, and A. Hrbek, "Magnetoacousto Electrical Tomography: A new Imaging Modality for Electrical Impedance," *2007 IFMBE Proceeding 17*, pp. 292- 295, 2007.
- [20] S Haider, A Hrbek, and Y Xu, "Magneto-acousto-electrical tomography: a potential method for imaging current density and electrical impedance," *Physiol.Meas*, vol.S29, pp.41-50, 2008.
- [21] Chaudhary, S.S., Mishra, R. K., Swarup, A., Thomas, J. M., "Dielectric Properties Of Normal And Malignant Human-Breast Tissues At Radiowave And Microwave-Frequencies," *Indian Journal of Biochemistry & Biophysics*, vol. 21, pp. 76-79, 1984.
- [22] S. Gabriel, R. W. Lau, and C. Gabriel, "The dielectric properties of biological tissues: III. Parametric models for the dielectric spectrum of tissues," *Phys. Med., Biol.*, vol. 41, no. 11, pp. 2271-2293, Nov. 1996.
- [23] A. E. Bulyshev, S. Y. Semenov, A. E. Souvorov, R. H. Svenson, A. G. Nazarov, Y. E. Sizov, and G. P. Tatsis, "Computational modeling of three-dimensional microwave tomography of breast cancer," *IEEE Trans. Biomed. Eng.*, vol. 48, no. 9, pp. 1053-1056, Sep. 2001.
- [24] P. M. Meaney, M. W. Fanning, D. Li, S. P. Poplack, and K. D. Paulsen, "A clinical prototype for active microwave imaging of the breast," *IEEE Trans. Microw. Theory Tech.*, vol. 48, no. 11, pp. 1841-1853, Nov. 2000.
- [25] P. M. Meaney, K. D. Paulsen, B. W. Pogue, and M. I. Miga, "Microwave image reconstruction utilizing log-magnitude and unwrapped phase to improve high-contrast object recovery," *IEEE Trans. Med. Imag.*, vol. 20, no. 2, pp. 104-116, Feb. 2001.

- [26] S. C. Hagness, A. Taflove, and J. E. Bridges, "Two-dimensional FDTD analysis of a pulsed microwave confocal system for breast cancer detection: fixed-focus and antenna-array sensors," *IEEE Trans. Biomed. Eng.*, vol. 45, pp. 1470–1479, Dec. 1998.
- [27] E. J. Bond, X. Li, S. C. Hagness, and B. D. Van Veen, "Microwave imaging via space-time beamforming for early detection of breast cancer," *IEEE Trans. Antennas Propag.*, vol. 51, no. 8, pp. 1690–1705, Aug. 2003.
- [28] E. C. Fear and M. A. Stuchly, "Microwave system for breast tumor detection," *IEEE Microwave Guided Wave Lett.*, vol. 9, pp. 470–472, Nov. 1999.
- [29] W. T. Joines, Y. Zhang, C. X. Li, R. L. Jirtle, "The measured electrical properties of normal and malignant human tissues from 50 to 900 Mhz," *Med. Phys.*, vol. 21, pp. 547-550, 1994.
- [30] A. J. Surowiec, S. S. Stuchly, J. R. Barr, A. Swarup, "Dielectric properties of breast-carcinoma and the surrounding tissue," *IEEE Trans. on Biomed. Eng.*, vol. 35, pp. 257-263, 1988.
- [31] Meaney, P. M., Fanning, M. W., Reynolds, T., Fox, C. J., Fang, Q. Q., Kogel, C. A., Poplack, S. P., Paulsen, K. D., "Initial Clinical Experience With Microwave Breast Imaging In Women With Normal Mammography," *Academic Radiology*, 2007. 14(2): p. 207-218.
- [32] Souvorov, A. E., Bulyshev, A. E., Semenov, S. Y., Svenson, R. H., Tatsis, G. P., "Two-Dimensional Computer Analysis Of A Microwave Flat Antenna Array For Breast Cancer Tomography," *IEEE Transactions on Microwave Theory and Techniques*, 2000. 48(8): p. 1413-1415.
- [33] Hagness, S., "Space-Time Microwave Imaging For Breast Cancer Detection: Theoretical Principles And Experimental Techniques," *Medical Physics*, 2003. 30(6): p. 1541-1541.
- [34] Lazebnik, M., McCartney, L., Popovic, D., Watkins, C. B., Lindstrom, M. J., Harter, J., Sewall, S., Magliocco, A., Booske, J. H., Okoniewski, M., Hagness, S. C., "A Large-Scale Study Of The Ultrawideband Microwave Dielectric Properties Of Normal Breast Tissue Obtained From Reduction Surgeries", *Physics in Medicine and Biology*, 2007. 52(10): p. 2637-2656.
- [35] Lazebnik, M., Popovic, D., McCartney, L., Watkins, C. B., Lindstrom, M. J., Harter, J., Sewall, S., Ogilvie, T., Magliocco, A., Breslin, T. M., Temple, W., Mew, D., Booske, J. H., Okoniewski, M., Hagness, S. C. "A Large-Scale Study Of The Ultrawideband Microwave Dielectric Properties Of Normal, Benign And Malignant Breast Tissues Obtained From Cancer Surgeries". *Physics in Medicine and Biology*, 2007. 52(20): p. 6093-6115.
- [36] Kruger, R. A., Miller, K. D., Reynolds, H. E., Kiser, W. L., Reinecke, D. R., Kruger, G. A., "Breast Cancer -In Vivo: Contrast Enhancement With Thermoacoustic CT At 434 Mhz Feasibility Study.", *Radiology*, 2000. 216(1): p. 279-283.



- [37] Shea, J. D., Kosmas, P., Van Veen, B. D., Hagness, S. C., "Contrast-Enhanced Microwave Imaging Of Breast Tumors: A Computational Study Using 3D Realistic Numerical Phantoms." *Inverse Problems*, 2010. 26(7).
- [38] Chen, Y.F., I.J. Craddock, and P. Kosmas, "Feasibility Study of Lesion Classification via Contrast-Agent-Aided UWB Breast Imaging". *IEEE Transactions on Biomedical Engineering*, 2010. 57(5): p. 1003-1007.
- [39] Mashal, A., J.H. Booske, and S.C. Hagness, "Toward Contrast-Enhanced Microwave-Induced Thermoacoustic Imaging Of Breast Cancer: An Experimental Study Of The Effects Of Microbubbles On Simple Thermoacoustic Targets". *Physics in Medicine and Biology*, 2009. 54(3): p. 641-650.
- [40] Ku, G. and L.H.V. Wang, "Combining Microwave And Ultrasound: Scanning Thermoacoustic Tomography," in *Proceedings of the 22nd Annual International Conference of the IEE Engineering in Medicine and Biology Society*, Vols 1-4, J.D. Enderle, Editor 2000. p. 2321-2323.
- [41] Wang, L.H.V., and G. Ku, " Hybrid Medical Imaging: Scanning Thermoacoustic Tomography." *13th IEEE Symposium on Computer-Based Medical Systems*, 2000. 129-134.
- [42] Yao, L., G.F. Guo, and H.B. Jiang, "Quantitative Microwave-Induced Thermoacoustic Tomography". *Medical Physics*, 2010. 37(7): p. 3752-3759.
- [43] Wikimedia Foundation Inc, "Breast," <http://en.wikipedia.org/wiki/Breast>, 24 Aug. 2013. Date of last access: 03 Sep. 2013.
- [44] Samani, A., J. Zubovits, and D. Plewes, "Elastic Moduli Of Normal And Pathological Human Breast Tissues: An Inversion-Technique-Based Investigation Of 169 Samples," *Physics in Medicine and Biology*, 2007. 52(6):p. 1565-1576.
- [45] Fatemi, M., A. Manduca, and J.F. Greenleaf, "Imaging Elastic Properties Of Biological Tissues By Low-Frequency Harmonic Vibration." *Proceedings of the IEEE*, 2003. 91(10): p. 1503-1519.
- [46] Maleke, C. and E.E. Konofagou, "Harmonic Motion Imaging For Focused Ultrasound (HMIFU): A Fully Integrated Technique For Sonication And Monitoring Of Thermal Ablation In Tissues." *Physics in Medicine and Biology*, 2008. 53(6): p. 1773-1793.
- [47] Abbosh, A., "Early Breast Cancer Detection Using Hybrid Imaging Modality." 2009 *IEEE Antennas and Propagation Society International Symposium and Usnc/Ursi National Radio Science Meeting*, Vols 1-62009. 1456-1459.
- [48] Zhao, M., Shea, J. D., Hagness, S. C., Van der Weide, D. W., Van Veen, B. D., Varghese, T., "Numerical Study of Microwave Scattering in Breast Tissue via Coupled

Dielectric and Elastic Contrasts". *IEEE Antennas and Wireless Propagation Letters*, 2008. 7: p. 247-250.

[49] M. Zhao, "Contributions to Cost Reduction and Sensitivity Improvement of Microwave Breast Cancer Detection," Ph.D Dissertation, Dept. Elect.Comp. Eng., The University Of Wisconsin-Madison, Madison, WI, 2009.

[50] Maleke, C., Luo, J., Gamarnik, V., Lu, X. L., Konofagou, E. E., "Simulation Study of Amplitude-Modulated (AM) Harmonic Motion Imaging (HMI) for Stiffness Contrast Quantification with Experimental Validation," *Ultrasonic Imaging*, 2010. 32(3): p. 154-176.

[51] Maleke, C., Pernot, M. and Konofagou E.E, "A Single-Element Focused Transducer Method for Harmonic Motion Imaging", in *2005 IEEE Ultrasonics Symposium*, Vols 1-42005. p. 17-20.

[52] Alizad, A., Whaley, D. H., Greenleaf, J. F., Fatemi, M., "Critical Issues In Breast Imaging By Vibro-Acoustography". *Ultrasonics*, 2006. 44: p. E217-E220.

[53] Greenleaf, J.F. and M. Fatemi, "Ultrasound Stimulated Vibro-Acoustography", in 2001 *IEEE Ultrasonics Symposium Proceedings*, Vols 1 and 2, D.E. Yuhus and S.C. Schneider, Editors. 2001. p. 1613-1618.

[54] Konofagou, E. E., Ottensmeyer, M., Agabian, S., Dawson, S. L., Hynynen, K., "Estimating Localized Oscillatory Tissue Motion For Assessment Of The Underlying Mechanical Modulus". *Ultrasonics*, 2004. 42(1-9): p. 951-956.

[55] Fatemi, M. and J.F. Greenleaf, "Vibro-Acoustography: An Imaging Modality Based On Ultrasound-Stimulated Acoustic Emission". *Proceedings of the National Academy of Sciences of the United States of America*, 1999.96(12): p. 6603-6608.

[56] Lawrence, D.E. and K. Sarabandi, "Acoustic And Electromagnetic Wave Interaction: Analytical Formulation For Acousto-Electromagnetic Scattering Behavior Of A Dielectric Cylinder," *IEEE Transactions on Antennas and Propagation*, 2001. 49(10): p. 1382-1392.

[57] Nightingale, K. R., Palmeri, M. L., Nightingale, R. W., Trahey, G. E., "On The Feasibility Of Remote Palpation Using Acoustic Radiation Force." *Journal of the Acoustical Society of America*, 2001. 110(1): p. 625-634.

[58] Al-Jumaily, A. and Fatemi, M., *Biomedical Applications of Vibration and Acoustics in Imaging and Characterizations*, ASME Press, 2008.

[59] Guy, A.W., "Electromagnetic Fields And Relative Heating Patterns Due To A Rectangular Aperture Source In Direct Contact With Bilayered Biological Tissue". *IEEE Transactions on Microwave Theory and Techniques*, 1971. MT19(2): p. 214.

- [60] Gupta, R.C. and S.P. Singh, "Analysis Of The SAR Distributions in Three Layered Bio-Media ·In Direct Contact With A Water-Loaded Modified Box-Horn Applicator". *IEEE Transactions on Microwave Theory and Techniques*, 2005. 53(9): p. 2665-2671.
- [61] Gupta, R.C. and S.P. Singh, "Mutual Coupling Between Box-Horn Elements Of A Phased Array Terminated In Three-Layered Bio-Media". *IEEE Transactions on Antennas and Propagation*, 2007. 55(8): p. 2219-2227.
- [62] Nikita, K.S. and N.K. Uzunoglu, "Analysis Of The Power Coupling From A Wave-Guide Hyperthermia Applicator Into A 3-Layered Tissue Model". *IEEE Transactions on Microwave Theory and Techniques*, 1989. 37(11): p.1794-1801.
- [63] Compton Jr., R.T., "The Admittance of Aperture Antenna Radiating Into Lossy Media," 1964, Ohio State Univ., Antenna Lab.: Columbus, OH.
- [64] R. F.Harrington, *Time-Harmonic Electromagnetic Fields*, Wiley-IEEE Press, 2001.
- [65] R.E.Collin, *Foundations For Microwave Engineering*, Wiley-IEEE Press, 2000.
- [66] Tsang, L., J.A. Kong, and K.-H. Ding, *Scattering Of Electromagnetic Waves:Theories and Applications*, John Wiley & Sons, Inc., 2000.
- [67] Food and Drug Administration, "HIFU Simulator," <http://www.fda.gov/aboutfda/centersoffices/officeofmedicalproductsandtobacco/cdrh/cdrhoffices/ucm301529.htm>, 24 Apr. 2012. Date of last access: 03 Sep. 2013.
- [68] N.S. Bakhvalov, Ya. M. Zhileikin and E.A. Zabolotskaya, *Nonlinear Theory of Sound Beams*, American Institute of Physics, New York, 1987 (Nelineinaya teoriya zvukovih puchkov, Moscow "Nauka", 1982).
- [69] Peter R. Hoskins, Kevin Martin, and Abigail Thrush, *Diagnostic ultrasound: Physics and equipment*, Cambridge University Press, 2010.
- [70] F. T. D'Astous, F. S. Foster, "Frequency dependence of ultrasound attenuation and backscatter in breast tissue," *Ultrasound Med. Biol.* 1986;12:795-808.
- [71] A. L. Scherzinger, R. A. Belgam, P. L. Carson, C. R. Meyer, J. V. Sutherland, F. L. Bookstein, T. M. Silver, "Assessment of ultrasonic computed tomography in symptomatic breast patients by discriminant analysis," *Ultrasound Med. Biol.*, 1989;15:21-28.
- [72] Lazebnik, M., Okoniewski, M., Booske, J. H., Hagness, S. C., "Highly Accurate Debye Models For Normal And Malignant Breast Tissue Dielectric Properties At Microwave Frequencies". *IEEE Microwave and Wireless Components Letters*, 2007. 17(12): p. 822-824.
- [73] J. A. Scheer, J.L. Kurtz, *Coherent Radar Performance Estimation*, Artech House Inc., 1993.

- [74] J. Smith, *Modern communication Circuits (2nd edition)*, McGraw Hill, 1998, p. 82.
- [75] "Guidelines For Limiting Exposure To Time-Varying Electric, Magnetic, and Electromagnetic Fields (Up To 300 Ghz)", ICNIRP, Editor 1997: Oberschleissheim, Germany.
- [76] P. Bernardi, M. Cavagnaro, S. Pisa, E. Piuzzi, "Specific absorption rate and temperature elevation in a subject exposed in the far-field of radio-frequency sources operating in the 10-900-MHz range". *IEEE Trans. Biomed. Eng.* 2003;50:295--304.
- [77] "Revised 510(k) Diagnostic Ultrasound Guidance for 1993", C.f.D.a.R.H. Food and Drug Administration, Editor 1993: Rockville, MD.
- [78] McDicken, W.N., "Diagnostic Ultrasonics: Principles and Use of Instruments", 1993, New York: John Wiley and Sons, Inc.
- [79] NCRP. Report No. 113: Exposure Criteria for Medical Diagnostic Ultrasound: I. Criteria Based on Thermal Mechanisms. NCRP Publications, Bethesda, MD 20814: National Council on Radiation Protection and Measurements, 1992.
- [80] F. A. Duck, *Physical Properties of Tissue: a Comprehensive Reference Book*, Academic Press, 1990.
- [81] Abbott JG. "Rationale and derivation of  $M_i$  and  $T_i$  - A review". *Ultrasound Med. Biol.* 1999;25(3):431-441.
- [82] Use of Mechanical Index in Place of Spatial Peak, Pulse Average Intensity in Determining Substantial Equivalence, Center for Devices and Radiological Health, US Food and Drug Administration, Rockville, MD, April 14, 1994.
- [83] M. L. Palmeri, K. R. Nightingale, "Acoustic radiation force-based elasticity imaging methods," *Interface Focus*, vol.1, pp. 553--564, 2011.
- [84] R.F. Harrington, *Field Computation by Moment Methods*. Oxford University Press, 1993.
- [85] C.S. Desai and J.F. Abel, *Introduction to the Finite Element Method: A Numerical Approach for Engineering Analysis*. New York: Van Nostrand Reinhold, 1972.
- [86] K.S. Yee, "Numerical solution of initial boundary-value problems involving Maxwell's Equations in isotropic media," *IEEE Trans. Ant. Prop.*, vol. AP-14, May 1966, pp. 302-307.
- [87] J. G. Maloney and G. S. Smith, "The efficient modeling of thin material sheets in the finite-difference time-domain (FDTD) method," *IEEE Transactions on Antennas and Propagation*, AP- 40, 3, pp, 323-330, 1990.

- [88] Wu, J.R. and G.H. Du, "Temperature Elevation Generated By A Focused Gaussian-Beam Of Ultrasound". *Ultrasound in Medicine and Biology*, 1990.16(5): p. 489-498.
- [89] University of Wisconsin Computational Electromagnetics Group,  
<http://uwcem.ece.wisc.edu/home.htm>, Jul. 2013, Date of last access: 03 Sep. 2013.
- [90] Virieux, J. (1984). SH wave propagation in heterogeneous media: velocity-stress finite-difference method, *Geophysics* 49, 1933-1957.
- [91] Virieux, J. (1986). P-SV wave propagation in heterogeneous media: velocity-stress finite-difference method, *Geophysics* 51, 889-901.
- [92] Levander, A. R. (1988). Fourth-order finite-difference P-SV seismograms, *Geophysics* 53, 1425-1436.
- [93] Randall, C. J. (1989). Absorbing boundary condition for the elastic wave Equation: velocity-stress formulation, *Geophysics* 54, 1141-1152.
- [94] Yomogida, K. and J. T. Etgen (1993). 3-D wave propagation in the Los Angeles Basin for the Whittier-Narrows earthquake, *Bull Seism. Soc. Am.* 83, 1325-1344.
- [95] Robert W. Graves, Simulating Seismic Wave Propagation in 3D Elastic Media Using Staggered-Grid Finite Differences, *Bulletin of the Seismological Society of America*, Vol. 86, No. 4, pp. 1091-1106, August 1996.
- [96] J. A. Roden and S. D. Gedney, "A convolutional PML for the effective absorption of evanescent waves in arbitrary media," *IEEE Transactions on Antennas and Propagation*, submitted for review, June 2000.
- [97] A. Taflov, S.C. Hagness, *Computational Electrodynamics: The Finite-Difference Time-Domain Method*. 2nd Edition, Boston, MA: Artech House, 2000.
- [98] A. P. Zhao and A. V. Raisanen, "Application of a simple and efficient source excitation technique to the FDTD analysis of waveguide and microstrip circuits," *IEEE trans. Microwave Theory Tech.*, vol. 44, no. 9, pp. 1535-1539, 1996.
- [99] Shibata, T. and T. Itoh, "Generalized-scattering-matrix modeling of waveguide circuits using FDTD field simulations," *IEEE Trans.on Microwave Theory and Techniques*, Vol. 46, 1742-1751, 1998.
- [100] D. E. Lawrence and K. Sarabandi, "Electromagnetic scattering from vibrating metallic objects using time-varying impedance boundary conditions," *IEEE Trans. Antennas Propag.*, vol. 2, pp. 782-785, Jan. 2002.

- [101] D. E. Lawrence and K. Sarabandi, "Electromagnetic scattering from vibrating penetrable objects using a general class of time-varying sheet boundary conditions," *IEEE Trans. Antennas Propag.*, vol. 54, no. 7, pp. 2054–2061, Jul. 2006.
- [102] A. M. Buerkle and K. Sarabandi, "Analysis of acousto-electromagnetic wave interaction using sheet boundary conditions and the finite-difference time-domain method," *IEEE Trans. Antennas Propag.*, vol. 55, no. 7, pp. 1991–1998, Jul. 2007.
- [103] T. B. A. Senior and J. L. Volakis, *Approximate Boundary Conditions in Electromagnetics*, 1995 :IEE Press.
- [104] Wein, W.,Khamene, A., Clevert, D., Kutter, O., Navab, N.,2007a, "Simulation and fully automatic multimodal registration of medical ultrasound," In: MICCAI 2007 Proceedings, vol. 4791 of Lecture Notes in Computer Science, Springer, pp. 136–143.
- [105] American College of Radiology, "Illustrated Breast Imaging Reporting and Data System (BI-RADS)". American College of Radiology, third edition, 1998.
- [106] Nikawa Y, Chino M and Kikuchi K "Soft and dry phantom modeling material using silicone rubber with carbon fibre," *IEEE Trans. Microw. Theory Tech.* vol. 44, pp.1949–53, 1996.
- [107] Lagendijk J J W and Nilsson P Hyperthermia dough: a fat and bone equivalent phantom to test microwave/radiofrequency hyperthermia heating systems *Phys. Med. Biol.* vol. 30, pp. 709–12, 1985.
- [108] Ito K, Furuya K, Okano Y and Hamada L " Development and characteristics of a biological tissue-equivalent phantom for microwaves Electron," *Commun. Japan* vol.1, no. 84, pp.1126–35, 2001.
- [109] D. Li, P. M. Meaney, and K. D. Paulsen. "Conformal Microwave Imaging for Breast Cancer Detection," *IEEE Trans. Microw. Theory Tech.* vol.51, pp.1179-1186, 2003.
- [110] H. Tamura, Y. Ishikawa, T. Kobayashi, and T. Nojima, "A dry phantom material composed of ceramic and graphite powder," *IEEE Trans. Electromagn. Compat.*, vol. 39, pp. 132–137, May 1997.
- [111] Bini M G, Ignesti A, Millanta L, Olmi R, Rubino N and Vanni R " The polyacrylamide as a phantom material for electromagnetic hyperthermia studies," *IEEE Trans. Biomed. Eng.* vol. 31 pp.317–22, 1984.
- [112] Robinson M J, Richardson M J, Green J L and Preece A W " New materials for dielectric simulation of tissues," *Phys. Med. Biol.* vol. 36 , pp.1565–71, 1991.

- [113] P. Meaney, K. Paulsen, A. Hartov, and R. Crane, "Microwave imaging for tissue assessment: Initial evaluation in multitarget tissueequivalent phantoms," *IEEE Trans. Biomed. Eng.*, vol. 43, pp. 878– 890, Sept. 1996.
- [114] A.W. Preece, J.L. Green, N. Potheary and R.H. Johnson "Microwave Imaging For Tumour Detection,". The Institution of Electrical Engineers, IEE, Savoy Place, London WC2R OBL, UK, 1994.
- [115] Lazebnik M, Madsen E L, Frank G R and Hagness S C "Tissue-mimicking phantom materials for narrowband and ultrawideband microwave applications," *Phys. Med. Biol.* vol.50, pp.4245–58, 2005.
- [116] Andreuccetti, D.; Bini, M.; Ignesti, A. "Use of polyacrylamide as a tissue-equivalent material in the microwave range," *IEEE Trans. Biomed. Eng.* vol.35, pp.275–277; 1988.
- [117] Surowiec A, Shrivastava P N, Astrahan M and Petrovich Z "Utilization of a multilayer polyacrylamide phantom for evaluation of hyperthermia applicators ,"*Int. J. Hyperthermia* vol.8, pp.795–807, 1992.
- [118] P. M. Meaney, K. D. Paulsen, and J. T. Chang, "Near-field microwave imaging of biologically-based materials using a monopole transceiver system," *IEEE Trans. Microwave Theory Tech.*, vol. 46,pp. 31–45, 1998.
- [119] W.M.A Wan Ibrahim, H.M Algabroun and M.T. Almaqtari. 2008. "Short Review on the used Recipes to Simulate the Bio-tissue at Microwave Frequencies". *4th Kuala Lumpur International Conference on Biomedical Engineering*. Kuala Lumpur. 25 28
- [120] Hall,T. J., Bilgen,M., Insana,M. F.&Krouskop,T.A."Phantommaterials for elastography." *IEEETrans. Ultrason. Ferroelect. Freq. Contr.* 44, 1355–1365, 1997.
- [121] Madsen, E. L., Hobson, M. A., Shi, H., Varghese, T. &Frank, G. R. "Stability of heterogeneous elastographyphantoms made from oil dispersions in aqueous gels", *Ultrasound Med. Biol.* 32, 261–270 2006.
- [122] Negron, L. A., Viola, F., Toth, C. A. & Walker, W. F. "Development and characterisation of a vitreous mimicking material for radiation force imaging." *IEEE Trans. Ultrason. Ferroelect. Freq. Contr.* 49, 1543–1551,2002.
- [123] Oudry, J., Bastard, C., Miette, V., Willinger, R. & Sandrin, L. "Copolymer-in-oil phantom materials for elastography." *Ultrasound Med. Biol.* 35, 1185–1197, 2009.
- [124] Madsen, E. L., Hobson, M. A., Frank, G. R., Shi, H., Jiang, J., Hall, T. J., Varghese, T., Doyley, M. M. &Weaver, J. B. "Anthropomorphic breast phantoms for testing elastography systems". *Ultrasound Med. Biol.*32, 857–874,2006.

- [125] Madsen, E. L. , Frank, G.R, Krouskop, T.A, Varghese, T., Kallel, F., Ophir, J. “Tissue mimicking oil-in-gelatin dispersions for use in heterogeneous elastography phantoms”, *Ultrasonic Imaging* 25, 17-38 (2003).
- [126] F. M. Ghannouchi and R. G. Bosisio, “Measurement of microwave permittivity using a six-port reflectometer with an open-ended coaxial line,” *IEEE Trans. Instrument. Meas.*, vol. 38, no. 2, pp. 505-508, Apr.1989.
- [127] E. L. Madsen, J. A. Zagzebski, R. A. Banjavic, and R. Jutila, "Tissue mimicking materials for ultrasound phantoms," *Med. Phys.*, vol. 5, pp. 391-394, 1978.
- [128] M. Ostadrahimi, R. Reopelle, S. Noghalian, S. Pistorius, A. Vahedi, F. Safari, “A Heterogeneous Breast Phantom for Microwave Breast Imaging”, *Annual International Conference of the IEEE Engineering in Medicine and Biology Society*. IEEE Engineering in Medicine and Biology Society. Conference, 2009:2727-2730, 2009.
- [129] J. Croteau, J. Sill, T. Williams and E. Fear, “Phantoms for testing radar-based microwave breast Imaging”, *Antenna Technology and Applied Electromagnetics and the Canadian Radio Science Meeting, 2009*. ANTEM/URSI 2009. 13th International Symposium on, on page(s): 1 – 4.
- [130] E. Porter, J. Fakhoury, R. Oprisor, M. Coates and M. Popović, “Improved Tissue Phantoms for Experimental Validation of Microwave Breast Cancer Detection”, *Proc. 4th European Conference on Antennas and Propagation (EUCAP 2010)*, 1-5, Apr. 12-16, 2010.
- [131] J. C. Y. Lai, C. B. Soh, E. Gunawan, and K. S. Low, “Homogeneous and Heterogeneous Breast Phantoms for Ultra-WideBand and Microwave Imaging Applications”, *Progress In Electromagnetics Research*, Vol. 100, 397-415, 2010.
- [132] Pace, W. E., Westphal, W. B. And Goldblith, S. A., “Dielectric Properties of Commercial Cooking Oils,” *Journal of Food Science*, 33: 30–36, 1968.



## CURRICULUM VITAE

### PERSONAL INFORMATION

Surname, Name: Top, Can Barış

Nationality: Turkish (TC)

Date and Place of Birth: 2 November 1981 , Ankara

Marital Status: Married

Phone: +90 505 4006724

Fax: +90 312 592 1043

email: [cbsen@aselsan.com.tr](mailto:cbsen@aselsan.com.tr)

### EDUCATION

Degree	Institution	Year of Graduation
MS	METU Electrical and Electronics Eng.	2006
BS	METU Electrical and Electronics Eng.	2003
High School	İzzet Baysal Anatolian High School, Bolu	1999

### WORK EXPERIENCE

Year	Place	Enrollment
2004-present	ASELSAN Inc. /TURKEY	RF, Microwave and Antenna Design Engineer

### FOREIGN LANGUAGES

Advanced English, Basic Spanish

### PUBLICATIONS

#### Journal Articles

1. Top, C.B.; Gencer, N.G., "Harmonic Motion Microwave Doppler Imaging : A Simulation Study Using a Simple Breast Model," Submitted to *Transactions on Medical Imaging, IEEE* , accepted on July 22, 2013.
2. Top, C.B.; Gencer, N.G., "Simulation of the Scattered Field From a Vibrating Tumor Inside the Tissue Using 3D-FDTD Method," *Microwave and Wireless Components Letters, IEEE* , vol.23, no.6, pp.273,275, June 2013.

3. (In progress) Top, C.B., Gençer, N.G., "Numerical Analysis on Harmonic Motion Microwave Doppler Imaging for Breast Cancer Detection," will be submitted to *Transactions on Antennas and Propagation, IEEE* .

### Conference Papers

1. Top, C.B., Dogan, D., "A circularly polarized omni-directional low loss Ka-band slot antenna," *Antennas and Propagation Society International Symposium (APSURSI), 2012 IEEE* , vol., no., pp.1,2, 8-14 July 2012
2. Dogan, D., Top, C.B., "Circularly polarized Ka-band waveguide slot array with low sidelobes," *Antennas and Propagation (EUCAP), 2012 6th European Conference on*, vol., no., pp.1105-1109, 26-30 March 2012.
3. Top, C.B., Dogan, D., Dalkılıç, A., "Ka Bant yönsüz dairesel polarize yarıklı dalga kılavuzu anten," *URSI TÜRKİYE Ulusal Kongresi 2012*, 02-05 Eyl.2012, 2012.
4. Top, C.B., Saralp, C., "Ku Bant dalga kılavuzu döner eklem tasarımı," *URSI TÜRKİYE Ulusal Kongresi 2012*, 02-05 Eyl.2012, 2012.
5. Dogan, D., Top, C. B., "Ka Bant dairesel polarize yarıklı dalga kılavuzu anten," *URSI TÜRKİYE Ulusal Kongresi 2012*, 02-05 Eyl.2012, 2012.
6. Top, C.B., Gençer, N.G., " Dokunmasız yolla elektriksel iletkenlik ölçümleri için analitik formülasyon," 15. Biyomedikal Mühendisliği Ulusal Toplantısı, BIYOMUT 2010, 2010, vol., no., pp.1-4, 21-24 April 2010.
7. Top, C. B., Gençer, N.G., "DFD yöntemi ile dokunmasız elektriksel iletkenlik görüntüleme benzetim çalışmaları," 14. Biyomedikal Mühendisliği Ulusal Toplantısı, BIYOMUT 2009., vol., no., pp.1-4, 20-22 May 2009.
8. Top, C. B., Gençer, N. G., "Dokunmasız Elektriksel İletkenlik Görüntüleme Yöntemi ile Meme Kanseri Tanısı Üzerine Simülasyon Çalışmaları,"13. Biyomedikal Mühendisliği Ulusal Konferansı, BİYOMUT 2008, 433-436, 2008.
9. Top, C. B., İnal, M.E., Hızal, A., "Yarıklı Dalga Kılavuzu Dizi Antenlerde Yarıklı Elemanı Modellemesi " ,*URSI TÜRKİYE Ulusal Kongresi 2006*, 06-08 Eyl.2006, s.100-103, 2006.

## **GRANTS/AWARDS**

**2012-2013**     **Research Grant and Scholarship:** "Harmonic Motion Microwave Doppler Imaging Method", 112E031, The Scientific and Technological Research Council of Turkey (TUBITAK).

**2012**            **Finalist** in Patents in Application Phase Category  
For the patent application: "Hybrid Mechanical-Electromagnetic Imaging Method and the system Thereof," 2. Ar-Ge ve Teknoloji Günleri, ArEge2, Turkey

**2007-2011**     **Scholarship:** "Electrical Impedance Imaging with Current Induction and Magnetic Field Measurements,"106E170, The Scientific and Technological Research Council of Turkey (TUBITAK).

## **PATENTS PENDING**

Top, C.B., Gençer, N.G, Hybrid Mechanical-Electromagnetic Imaging Method and the system Thereof, 2012.

Top, C.B., Dogan, D., Omni-directional Circularly Polarized Waveguide Slot Antenna, PCT Patent Application, 2012.

Dogan, D., Top, C.B., Circularly Polarized Slotted Waveguide Antenna, PCT Patent Application, 2012